UNIVERSITY OF CALIFORNIA
RIVERSIDE

Refinement of Nanocomposite Coating and Magnesium Substrate Surface Properties for Improved Degradation Resistance and Bone Cell Adhesion

A Dissertation submitted in partial satisfaction
of the requirements for the degree of

Doctor of Philosophy

in

Bioengineering

by

Ian James Johnson

June 2016

Dissertation Committee:

Dr. Huinan Liu, Chairperson
Dr. Valentine Vullev
Dr. Prudence Talbot

The Dissertation of Ian James Johnson is approved:

Committee Chairperson

University of California, Riverside

Acknowledgements

Many people have contributed their support to this dissertation, and to my growth as a scientist. First and foremost, I would like to thank my advisor, Dr. Huinan Liu, for her tireless guidance and constant support. She has taught me not just about science, but how to perceive the world and how to better communicate with others. These lessons will be invaluable to me throughout my life. I truly appreciate the time and effort that she has invested in me as a graduate student and as a person. I would also like to thank Dr. Valentine Vullev and Dr. Prudence Talbot for their service on my graduate committee and the invaluable advice that they have provide me.

I thank the members of my lab for their camaraderie and support, especially those who helped me carry out the work described herein; Michelle Sebo, Christine Silken, Khalid Akari, and Anisha Butala. I was blessed to have such wonderful colleagues in my lab, all of whom supported me through my challenges and made the lab such an enjoyable place. I would also like to thank the journals PLOS One and Nanotechnology for publishing my work, some of which appears herein.

Finally, I would like to thank my family for their unwavering support, without which this task would have been impossible. My parents instilled in me the values needed to accomplish my goals and provided me with opportunities for success. I will never be able to pay back my debt for their unconditional love, and this work is dedicated to them.

ABSTRACT OF THE DISSERTATION

Refinement of Nanocomposite Coating and Magnesium Substrate Surface Properties for Improved Degradation Resistance and Bone Cell Adhesion

by

Ian James Johnson

Doctor of Philosophy, Graduate Program in Bioengineering
University of California, Riverside, June 2016
Dr. Huinan Liu, Chairperson

The mechanical and biological properties of magnesium (Mg) alloys are well-suited for biodegradable bone implants, but rapid degradation limits their use for implant applications. Modern advancements in material science offer solutions to this challenge.

Addressing the rapid degradation of Mg alloys requires a deeper understanding of their degradation processes. Mg degradation is the result of multiple interacting factors including: alloy composition, alloy surface type, and immersion media. It was demonstrated that an alloy composition/surface type pair that reduced degradation in one immersion media could increase degradation in a different immersion media. This demonstrates that a Mg alloy designed for slower degradation in general may actually increase degradation in certain environments. Mg alloys should be designed for the specific application and environment for which they are intended.

Nanophase hydroxyapatite (nHA)/polymer nanocomposite coatings were developed as an additional means of controlling Mg alloy degradation. Delamination can limit the functionality of the coatings, but can be prevented through engineering controls. Three different polymers were investigated as components for the nanocomposite coatings; all of them significantly reduced Mg degradation. Post-deposition processing of

the coatings and surface treatments of the Mg substrates may also improve the barrier qualities of the coatings. Furthermore, the nanocomposite coatings improved bone cell adhesion to the Mg substrates. Poly(caprolactone) (PCL) was the most effective polymer coating component for reducing Mg degradation because it has low water permeability and mechanical properties that minimize internal stress. Guidelines for the rational design of nanocomposite coatings were elucidated over the course of this investigation, which will aid in the clinical translation of Mg alloys as biomaterials for bone implants.

Table of Contents

Acknowledgements iiiii

ABSTRACT OF THE DISSERTATION iiv

Table of Contents vii

List of Tables xiiiii

List of Figures xiv

Chapter 1- Introduction 1

1.1- The Advantages of Biodegradable Implants 1

1.2- Mg Alloys Have Many Desirable Properties for Biodegradable Implants 3

1.3- Rapid Degradation Limits the Clinical Translation of Mg Alloys for Biodegradable Implants 3

1.4- Alloy Composition and Processing can Reduce Mg Degradation 5

1.5- Mg Substrate Surfaces Affect Degradation and Coating Adhesion 6

1.6- Coatings can Control Mg Degradation and Surface Properties 7

1.6.1- Hydroxyapatite Coatings 7

1.6.2- Polymer Coatings 9

1.6.3- Nanocomposite Coatings 10

1.6.4- The Spin Coating Process 12

1.7- Objective 13

Chapter 2- Mg Degradation is Influenced by Interactions between Multiple Factors 14

2.1- Specific Challenges and Aims 14

2.2- Materials and Methods 16

2.2.1- Preparation of Pure Mg and Mg-Y Alloy Samples 16

2.2.2- Degradation of cpMg* and MgY* in Immersion Solution 17

2.2.3- Statistical Analysis of Degradation Data 18

2.2.4- Surface Characterization of cpMg* and MgY* 19

2.3- Results 19

2.3.1- Degradation of the cpMg* and MgY* Samples in DI Water 19

2.3.2- Degradation of the cpMg* and MgY* Samples in PBS 24

2.3.3- Statistical Analysis of Mass Loss during Degradation 27

2.3.4- Surface Microstructure and Composition of cpMg* and MgY* Before and After Degradation 31

2.4- Discussion 33

2.4.1- Surface Type and Alloy Composition Influenced Degradation in DI Water 33

2.4.2- Surface Type and Alloy Composition Influenced Degradation in PBS 33

2.4.3- Interactions Between Surface Type, Alloy Composition, and Immersion Media Influenced Degradation 36

2.4.4- Surface Microstructure and Elemental Composition Influenced Degradation 37

2.5- Conclusions of Chapter 2 40

Chapter 3- Nanocomposite Coatings Reduce Mg Degradation 41

3.1- Specific Challenges and Aims 41

3.2- Materials and Methods 42

3.2.1- Preparation and Characterization of Mg Substrates and the Controls 42

3.2.2- Preparation and Characterization of nHA 42

3.2.3- Spin Coating the nHA/PLGA Nanocomposites onto the Mg Substrates and the Controls 43

3.2.4- Spin Coating Pure PLGA onto the Mg Substrates and the Controls 45

3.2.5- Depositing CaP Control Coating onto the Mg Substrates and the Controls 45

3.2.6- Characterization of the Coatings and Controls 45

3.2.7- Degradation Studies by Potentiodynamic Polarization Test 46

3.2.8- Degradation Studies by Immersion Method 48

3.3- Results 49

3.3.1- Characterization of the nHA Particles 49

3.3.2- Characterization of the Coated and Non-coated Mg Substrates 51

3.3.3- Degradation Rate Determined by PDP Test 54

3.3.4- Degradation Determined by Immersion Method 56

3.4- Discussion 66

3.4.1- Composite Coatings had Nanoscale Features 66

3.4.2- The nHA was Well Dispersed in the nHA/PLGA Films and Coatings 66

3.4.3- Delamination Limited the Duration of the Coatings Effectiveness 68

3.4.4- Dispersed nHA Improved CaP Deposition onto Coating Surfaces during Immersion 69

3.4.5- Gas Evolution Promoted Delamination of Coatings 70

3.5- Conclusions of Chapter 3 73

Chapter 4- Optimization of Nanocomposite Coatings for Improved Interfacial Properties of Mg Substrates 74

4.1- Specific Challenges and Aims 74

4.2- Materials and Methods 75

4.2.1- Preparation of Magnesium Substrates 75

4.2.2- Preparation of Nanocomposite Coatings on the Mg Substrates 76

4.2.3- Measurement of Surface Hydrophobicity 79

4.2.4- Potentiodynamic Polarization Measurements for Corrosion Rates 81

4.2.5- Degradation Measurements via Immersion in rSBF 82

4.2.6- Measurements of Coating Adhesion Strength 83

4.2.7- BMSC Study *In Vitro* 84

4.2.8- Statistical Analyses 86

4.3- Results 87

4.3.1- Thickness of the Nanocomposite Coatings on Mg Substrates 87

4.3.2- The Effects of the Coating Parameters on Surface Hydrophobicity 88

4.3.3- The Effects of the Coating Parameters on Corrosion Rates Calculated from PDP Testing 91

4.3.4- Degradation Results from the Immersion Study 97

4.3.5- Coating Adhesion Strength 107

4.3.6- BMSC Adhesion and Morphology 108

4.4- Discussion 112

4.4.1- A Defined Model System for Studying the Key Parameters Affecting Nanocomposite Coatings on Magnesium 112

4.4.2- The Polymer Component in the Nanocomposite Coatings Influenced the Coating Permeability and Interface with the Mg Substrate 113

4.4.3- The Post-Deposition Processing and Substrate Surface Conditions Influenced the Coating Permeability 115

4.4.4- Interactions among the Key Parameters and their Effects on Internal Stress and Corrosion 117

4.4.5- The Key Parameters Affecting the Coating Integrity and Adhesion Strength before and after Immersion Degradation 122

4.4.6- The Most Effective Nanocomposite Coatings in Reducing Degradation and Improving BMSC Adhesion 124

4.4.5- Conclusions of Chapter 4 127

Chapter 5- Major Conclusions and Proposals for Future Research 128

5.1- The Promise of Mg Alloys for Bone Implant Applications 128

5.2- Design Criteria for Nanocomposite Coatings on Mg Alloys 129

5.3- Summary of Major Conclusions 129

5.4- Future Research 130

References 131

List of Tables

Table 2.1: Statistical analysis of Mg* and MgY* degradation……28

Table 2.2: Effects of degradation upon Mg* and MgY* surface composition……..32

Table 4.1: Spin coating speed and coating thicknesses……77

Table 4.2: List of nHA/polymer nanocomposite coated Mg samples with all the processing parameters that were investigated, screened, and compared for optimal outcome……80

Table 4.3: Statistical analysis of the parameters that affected Mg degradation in the immersion study using the Wild Bootstrap……103

Table 4.4: Properties of each polymer type used in nanocomposite coatings on Mg substrates……..114

List of Figures

Figure 1.1: Frequency of complications occurring after surgical removal of implants……2

Figure 1.2: Illustration of the synergy between the nHA, polymer, and Mg substrates due to their complementary properties……12

Figure 2.1: Mg degradation rate and mode are influenced by multiple interacting factors that include: alloy composition, surface type, and physiological ions……..15

Figure 2.2: Photographs of the cpMg* and MgY* samples after degradation in DI water……....21

Figure 2.3: Sample mass change during degradation in DI water…….22

Figure 2.4: Sample pH change during degradation in DI water……23

Figure 2.5: Photographs of the cpMg* and MgY* samples after degradation in PBS……...25

Figure 2.6: Sample mass change during degradation in PBS…….26

Figure 2.7: Sample pH change during degradation in PBS……27

Figure 2.8: Interactions between three key factors that influence Mg* and MgY* lifetime……...30

Figure 2.9: Mg* and MgY* surface microstructure before and after degradation……31

Figure 2.10: Mg* and MgY* degradation rates in DI water and PBS…….35

Figure 3.1: Characterization of nHA……..50

Figure 3.2: Coating cross-section images……..51

Figure 3.3: SEM images of the surfaces of the materials of interest before degradation studies……..53

Figure 3.4: PDP analysis of coated and non-coated Mg……55

Figure 3.5: Photographs of the samples after immersion in rSBF……..57

Figure 3.6: Sample mass and pH change in rSBF……...59

Figure 3.7: Ion concentration change in rSBF after sample immersion……62

Figure 3.8: SEM images and respective EDX analyses of the coatings delaminated from Mg substrates after 24-hour degradation in rSBF……64

Figure 3.9: Hydrogen gas evolution after 2 hours of the sample degradation in rSBF……65

Figure 3.10: Illustration of the speculated mechanism for coating delamination from Mg-based substrates……72

Figure 4.1: Experimental setup for coating adhesion strength measurements……84

Figure 4.2: Cross-sections of nHA/polymer coatings on Mg substrates. ……88

Figure 4.3: Contact angles of DI water on coated and non-coated Mg substrates. ……..90

Figure 4.4: Representative potentiodynamic polarization curves of the nHA/polymer coated and non-coated Mg substrates with different post-deposition processing for the coatings on M_Mg and A_Mg……..92

Figure 4.5: Corrosion rates of the nHA/polymer coated and non-coated Mg substrates that were calculated based on corrosion current density extrapolated from PDP curves……94

Figure 4.6: Interaction plots of polymer component, substrate surface type, and post-deposition processing upon corrosion rate during PDP testing……97

Figure 4.7: Photographs of sample surface morphology after immersion in rSBF for the prescribed period……99

Figure 4.8: Characterization of rSBF immersion media……102

Figure 4.9: SEM images of the samples before and after immersion in rSBF for 7 days……104

Figure 4.10: SEM images of craters in nHA/PLGA coating on A_Mg after 7 days immersion in rSBF……105

Figure 4.11: Surface elemental composition of optimized samples before and after immersion in rSBF for 7 days; as measured using EDX……...106

Figure 4.12: Coating adhesion strength of the coated samples before and after they were immersed in rSBF for 7 days……...108

Figure 4.13: Fluorescence images of BMSCs after direct culture on the samples and controls for 24 hours……109

Figure 4.14: Quantitative Analysis of BMSC adhesion and morphology using ImageJ……111

Figure 4.15: Interactions between the coating parameters (polymer component, substrate surface, post-deposition processing) and the coating properties derived from those parameters……..118

Figure 4.16: Effect of Mg substrate surface type upon polymer crystals in the coating……122

Figure 4.17: Comparison of the mechanical, thermal, and transport properties of the polymer components used in the nanocomposite coatings……..125

Chapter 1- Introduction

1.1- The Advantages of Biodegradable Implants

Implants made from non-degradable materials like titanium (Ti) have improved the quality of life for numerous patients, especially when it is desirable that the implants remain functional for long periods of time (*e.g.* joint replacements). However, certain implants (*e.g.* internal fixation devices) only serve a necessary purpose for a set period of time. The use of biodegradable materials will avoid the need for surgical removal when those implants have fulfilled their purpose for that set period of time. Magnesium (Mg) alloys are biodegradable alternatives to non-degradable materials like Ti, and possess many desirable mechanical and biological properties [1, 2]. However, Mg alloys degrade too rapidly *in vivo*. The clinical translation of Mg alloys as biodegradable materials requires that their degradation be controlled through methods such as alloying, processing, coating, or a combination thereof.

Biodegradable implants are desirable for some applications because the long-term residence of exogenous materials in the human body can cause complications. A longer residence time for implants presents more time for those complications to occur; such as chronic pain [3], immune response [4], and osteolysis [5]. The human body may also lack pathways to clear wear particles or debris that are released from non-degradable materials, which can stimulate immune responses and is another major cause for implant revision [6]. In addition, exogenous materials are generally encapsulated within fibrous tissue [7], which can limit osteointegration and implant stability [8]. Furthermore,

infection is a commonly occurring complication in implants [9, 10] and occurs in around 5% of internal fixation devices [11].

Many of these complications may be addressed by surgically removing implants after they have fulfilled their function for the set period of time and are no longer needed [12]; but that additional surgery also has risks that include infection, re-fracture of bone, nerve damage, and limited mobility [13]. The frequency and severity of these complications vary greatly depending upon the hospital were the surgery was performed and the skill of the surgeon (Figure 1.1) [13]. For these reasons, there is considerable debate among clinicians about when or if implants should be surgically removed. The use of biodegradable materials could avoid the need for this contentious debate.

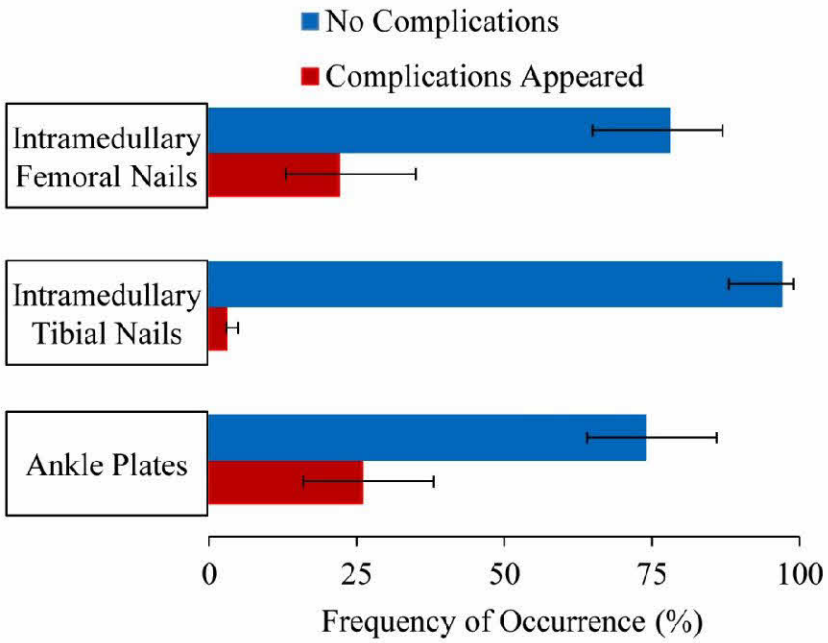

Figure 1.1: Frequency of complications occurring after surgical removal of implants. Common complications included infection, re-fracture of bone, and nerve damage. (Data obtained from [13]).

1.2- Mg Alloys Have Many Desirable Properties for Biodegradable Implants

Mg alloys have many properties that are well suited for biodegradable implant biomaterials. Their mechanical properties mimic cortical bone [14], which enables them to be used as load bearing materials while minimizing stress shielding [2, 15]. Furthermore, the degradation products of Mg are non-toxic and rapidly excreted from the body [16]. Mg-based materials also have many desirable interactions with cells and tissues such as: Mg can inhibit osteolysis induced by wear particles [17], Mg implants may have thinner fibrous capsules than similar Ti implants [18], Mg incorporation on Ti surfaces can increase the adhesion and differentiation of osteoblasts *in vitro* [19], Mg implants can have more bone growth on them than similar Ti implants *in vivo* [20], and Mg implants can adhere more strongly to bone than similar Ti implants *in vivo* [1]. For these reasons, Mg alloys have great potential as biodegradable bone implant biomaterials.

1.3- Rapid Degradation Limits the Clinical Translation of Mg Alloys for Biodegradable Implants

Despite the many desirable properties of Mg alloys for biomedical implant applications, their rapid *in vivo* degradation remains a challenge [21-23]. Rapid degradation can result in the mechanical failure of Mg implants before the healing tissues regain their mechanical strength. Rapid Mg degradation also produces excessive amounts of hydroxide ions (OH^-) and hydrogen gas (H_2). The OH^- can significantly increase the local pH, which may adversely affect cells. The H_2 evolution can lead to the formation of gas cavities in the tissue [24] and delamination of coatings from Mg substrates [25]. Controlling the degradation rate of Mg alloys will mitigate these complications.

Most Mg degradation in physiological environments occurs through reaction 1 below [26-28]. In aqueous environments, a degradation layer composed of $Mg(OH)_2$ forms on the surface of Mg through reaction 1b. This degradation layer provides only limited protection to Mg from subsequent degradation due to its loose and porous microstructure.

$$Mg + 2H_2O \rightarrow Mg^{2+} + 2OH^- + H_2\uparrow \quad (1a)$$

$$Mg^{2+} + 2OH^- \leftrightarrow Mg(OH)_2\downarrow \quad (1b)$$

Abundant chloride ions (Cl^-) in physiological fluids undermine the degradation layers on Mg surfaces. Microgalvanic coupling causes the α phase of Mg alloys to degrade more rapidly than the β phase [29]. Cl^- is electrochemically transported to the more anodic α phase where it is adsorbed [30]. The adsorption of Cl^- to Mg was greater than the adsorption of other halide ions to Mg, which has been demonstrated by the greater surface capacitance of Mg after exposure to Cl^- [29]. Adsorption of halide ions onto Mg is competitive [31]. The magnitude by which halide ions reduce the corrosion potential of Mg is proportional to the solubility of the products that halide ions form with Mg [32], and $MgCl_2$ is highly soluble. Cl^- is corrosive to Mg alloys because of the combination of electrochemical transportation of Cl^- to anodic regions, high adsorption of Cl^- onto the surface of Mg alloys, and the high solubility of the products that Cl^- forms with Mg. For these reasons, Cl^- undermines the degradation layer and exposes the underlying Mg substrate, which makes it vulnerable to further degradation.

Other compounds or ions in physiological fluids may also influence Mg degradation [33], and some can have a protective effect. Phosphates can increase the

density of the degradation layer and increase its resistance to Cl^- attack [34]. Carbonates can increase the stability of the degradation layer and inhibit pitting degradation processes [35]. The amount of physiological fluids in a location also affects Mg degradation.

Mg tends to degrade more quickly in the soft tissue or bone marrow than in cortical bone due to the differing amounts of physiological fluids [2-5]. This can cause the thread and head of screws to dissolve more rapidly than the shaft [36]. The varying fluid content also causes differences between *in vivo* and *in vitro* degradation rates [37-40].

The degradation rate of bone implants should be tailored to match the growth rate of bone tissue [41-43]. Excessively rapid degradation may create a gap between the implant and bone [44], while excessively slow degradation may impair healing. Mg implants can have a clinically equivalent outcome to Ti implants when Mg degradation is sufficiently controlled [2]; which can be accomplished through methods such as alloying, processing, surface modifications, coatings, or a combination thereof.

1.4- Alloy Composition and Processing can Reduce Mg Degradation

Other elements are frequently added to Mg alloys to control their properties, such as increasing their degradation resistance. Yttrium (Y) is a commonly used alloying element for Mg alloys; and is added to increase their mechanical strength [45, 46], ductility [47], and degradation resistance [48-52]. However, Y exhibits both degradation inhibiting and degradation promoting activities in Mg alloys. The net effect of these contrary activities upon Mg degradation depend on the interactions between multiple

factors such as alloy composition, alloy surface type, and physiological ions in the environment [53].

Yttrium oxide (Y_2O_3) accumulates in the degradation layer when Y migrates to the metal surface and is oxidized [54-56]. When a stable degradation layer is present, yttrium oxide in the degradation layer can slow down Mg degradation by inhibiting cathodic reactions [56]. When the degradation layer is not stable, Y can promote microgalvanic corrosion by making the β phase more cathodic [54]. The initial alloy surface plays a critical role in determining the net effects of Y upon the degradation of Mg alloys [53]. Furthermore, certain alloy compositions and surface properties that improve degradation resistance in one environment may accelerate degradation in another environment. Therefore, it is important to elucidate the interactions between the factors influencing Mg alloy degradation; that knowledge is needed to tailor Mg alloys for their intended applications *in vivo*.

1.5- Mg Substrate Surfaces Affect Degradation and Coating Adhesion

In addition to the bulk properties of alloys, their surfaces also influence their degradation [57, 58] and the adhesion of coatings. For example, sandblasted Mg surfaces degrade faster than threaded Mg surfaces, which in turn degrade faster than smooth Mg surfaces [59]. A rougher surface provides a larger surface area for binding and can mechanically interlock with coatings. Substrate surfaces can also be modified to alter their chemistry, which may alter the surface's affinity for coatings. Different surface modifications have varying effects with different types of coatings [60, 61]. The surface roughness also affects the cell adhesion and bone volume/tissue volume ratio (BV/TV) *in*

vivo [62]. Substrate surface processing or modifications may work in conjunction with alloy composition, bulk alloy processing, and coatings.

1.6- Coatings can Control Mg Degradation and Surface Properties

Coatings are another mechanism for controlling Mg degradation, and can be combined with other methods of degradation control like alloy composition [63, 64]. Coating properties can be complementary to the bulk Mg properties; so that the coatings control Mg degradation and bioactivity, while the Mg substrates support load-bearing activities. Multiple coatings or surface treatments may also be combined with each other [65, 66]. Coatings can perform multiple functions simultaneously such as controlling degradation, controlling interactions with cells and tissue, and controlled release of drugs [67]. These abilities make coatings a versatile method for controlling Mg degradation.

1.6.1- Hydroxyapatite Coatings

Hydroxyapatite (HA; $Ca_{10}(PO_4)_6(OH)_2$) is the predominant phase of calcium phosphate (CaP) in natural bone and has excellent osteoconductivity [68-70]. The size and structure of HA influences its biological and mechanical properties. Nanophase-HA (nHA) has improved osteoconductivity compared to HA with larger particle sizes [71, 72]. The shape of HA particles affects their interactions with cells; rod shaped HA particles may have increased cell proliferation and ALP activity compared to flake shaped HA particles [73]. The barrier properties of coatings are also affected by HA particle size and morphology; nHA coatings may provide less protection from degradation to underlying Mg substrates than HA coatings with larger particle sizes [74].

Mesoporous HA structures can ameliorate damage from residual stress, reduce penetration of electrolyte, and reduce Mg corrosion rates [75]. The wide range of properties for HA enables it to be fine-tuned for specific applications.

HA as a single material alone has limited use in load-bearing applications due to its inherent brittleness, but is frequently used as a coating material for metallic substrates such as Mg due to its excellent biological properties [21]. However, the brittleness of HA and its thermal expansion coefficient mismatch with metallic substrates can cause cracking in coatings [76]. In addition, a HA coating that adheres weakly to its substrate may limit the adhesion strength between an implant and bone [77].

HA coatings can be deposited through numerous methods such as: plasma spray, sol-gel, chemical deposition [78-81], biomimetic deposition [82], electrophoretic deposition [83], and electrochemical deposition [21, 84]. There are two general strategies for depositing HA coatings: (1) synthesizing HA first and then depositing it onto the substrate; and (2) simultaneously synthesizing HA and depositing it onto the substrate. The first strategy offers the most control over the properties of HA, but requires multiple steps. Furthermore, the painstakingly fine-tuned properties of the HA may be altered during the coating deposition process. High temperature coating processes such as plasma spray can change the phase of HA [85], alter the crystallinity of HA [85], or increase the size of HA particles. Alternatively, low temperature coating processes often create coatings with lower adhesion strength unless there is subsequent heat treatment [21]. The second strategy for depositing HA coatings is often simpler, but provides less control over the properties of the HA in the coating.

1.6.2- Polymer Coatings

Polymers commonly used to coat Mg alloys include poly(lactic-co-glycolic acid) (PLGA) [25, 86, 87], poly(L-lactic acid) (PLLA) [88-90], and poly(caprolactone) (PCL) [66, 88, 89, 91, 92]. These polymers have good biocompatibility because their degradation products are naturally occurring metabolites such as lactic acid, glycolic acid, and 6-hydroxyl caproic acid [93]. These synthetic polymers degrade primarily by hydrolysis of their ester bonds by water molecules.

PLGA is one of the most commonly used polymers in implants due to its physical properties and biocompatibility [94, 95]. The degradation rate [96] and water absorption [97] of PLGA can be tailored by altering the ratio of lactic acid to glycolic acid. PLGA coatings have been used to significantly reduce Mg degradation [25, 86, 87], but may delaminate due to H_2 evolution [25]. PLGA also has mediocre cell adhesion [98, 99], which limits bone growth at the implant site.

PLLA is another commonly used polymer in implants because of its high mechanical strength and biocompatibility. PLLA has an additional methyl group that increases its hydrophobicity and sterically hinders hydrolysis of its ester bonds. These properties enable PLLA coatings to provide significant protection from degradation to Mg substrates [88-90]. However, PLLA is brittle, which limits its use as a load bearing material. Additionally, PLLA also has an excessively long degradation time and mediocre bioactivity, which can lead to poor bone ingrowth at the implant site [100-102]. The impaired bone ingrowth may be exhibited by an empty hole outlining the original implant site after implant dissolution or surgical removal [101, 103, 104].

PCL is one of the earliest used polymers for biomedical implants [93]. The low melting temperature of PCL makes it easy to process, especially when combined with pharmaceuticals or proteins that are vulnerable to heat or organic solvents. This makes PCL a good coating material when drugs or bioactive factors are incorporated into the coating. However, PCL has an excessively long degradation time and mediocre bioactivity.

The polymers PLGA, PLLA, and PCL were chosen for this investigation because of their extensive history as implant biomaterials, ease of use as coating materials, and diverse properties. Comparing the different outcomes of the coatings can provide knowledge about which properties are beneficial to their function in this application.

1.6.3- Nanocomposite Coatings

The combination of Mg substrates, nHA, and polymers has many advantages that mitigate some of the challenges encountered when using those materials alone (Figure 1.2). The Mg substrate provides the mechanical strength and fracture toughness needed for load bearing applications. The nHA/polymer coating reduces the degradation rate of the Mg substrate. Dispersing nHA in a flexible polymer matrix can prevent the crack propagation that is frequently observed in nHA coatings [66]. Dispersion of nHA particles throughout a polymer matrix improves both the mechanical strength and the bioactivity of that polymer matrix [105-109]. The incorporation of nHA has been shown to significantly improve cell adhesion to PLGA [110], PLA [111, 112], and PCL matrices [113]. Increased protein secretion and alkaline phosphatase (ALP) activity are often observed as well [114]. The nHA composites also improve bone ingrowth at the implant

sites *in vivo*; HA/PLLA interference screws did not leave behind the empty screw holes [115, 116] in bone tissue that were observed with pure PLLA screws [104, 117]. The mechanical properties of PLGA and cell adhesion onto PLGA both increase proportionally with nHA content until a ratio of 30 wt.% nHA to 70 wt.% polymer. Increasing nHA content beyond 30 wt.% in PLGA matrices has limited effect upon cell adhesion, but increases brittleness [108-110, 118, 119]. For this reason, the ratio of 30 wt.% nHA to 70 wt.% polymer was chosen for this investigation.

The nHA particles also have profound effects upon the uptake and diffusion of water in polymer matrices, which influences the degradation of underlying Mg substrates. The nHA particles can increase water uptake by polymer matrices in some cases [94], but generally tend to improve the barrier properties of coatings [25]. Diffusion through particle/polymer composites is reduced by the filler effect; which is caused by particles increasing the tortuosity of routes taken by diffusing molecules, and by particles increasing the local rigidity of the polymer matrix surrounding them [120]. The combination of mechanical, biological, and transport properties possessed by nHA/polymer coatings is well suited for controlling Mg degradation.

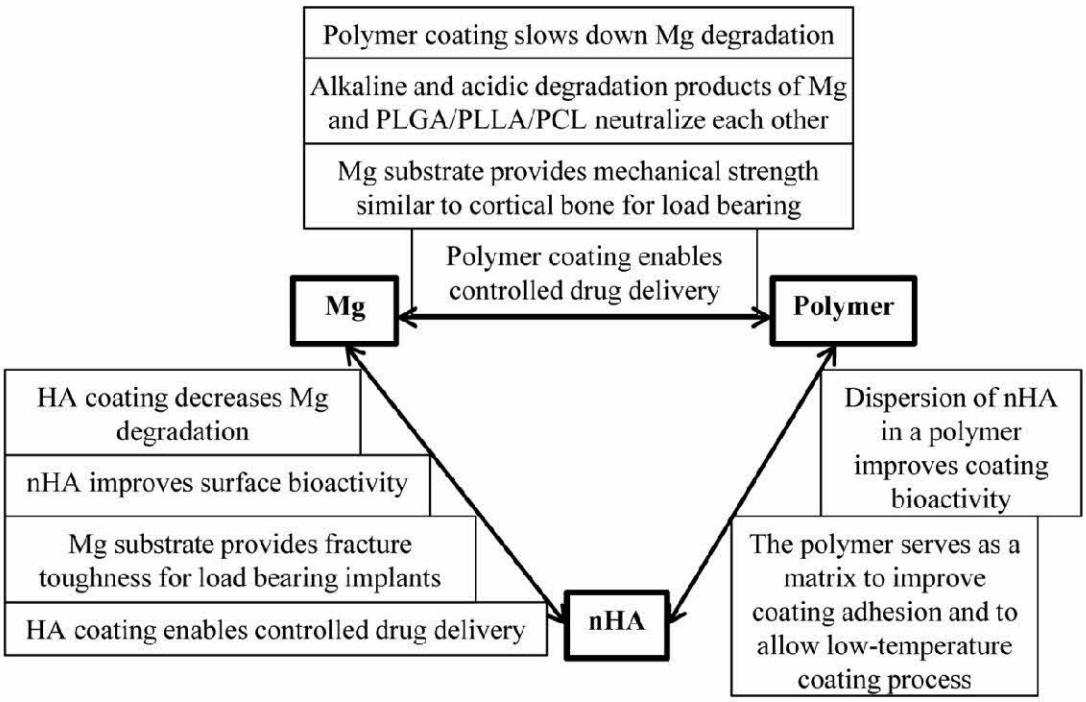

Figure 1.2: Illustration of the synergy between the nHA, polymer, and Mg substrates due to their complementary properties. The advantages of one material compensate for the disadvantages of another material.

1.6.4- The Spin Coating Process

Spin coating is a simple coating deposition method that creates homogenous coatings with well controlled thicknesses. After the coating solution/melt is deposited, the substrate is spun and centripetal force removes excess solution/melt to create a uniform coating. The thickness and structure of spin-deposited coatings are influenced by the amount of coating material added, solution/melt viscosity, solvent evaporation rate, and substrate surface roughness. The limitations of spin coating are that it can only be used on planar surfaces and that it is wasteful of coating materials. Spin coating was chosen as the

coating deposition process in this investigation because it can simply and rapidly create coatings with uniform structures.

1.7- Objective

Mg alloys have great potential as biodegradable implant materials, but their clinical translation is limited by their rapid degradation. The objective of this dissertation was to investigate that factors influencing Mg degradation in physiologically relevant environments, and then to develop nanocomposite coatings to reduce the degradation rate of Mg and increase the bioactivity of the surface.

Chapter 2- Mg Degradation is Influenced by Interactions between Multiple Factors

2.1- Specific Challenges and Aims

One of the first steps to the clinical translation of Mg alloys as implant biomaterials is to improve our understanding of their degradation in physiological environments; that knowledge is necessary to tailor their degradation rates. A broad range of experimental conditions was used to observe the interactions between the different factors influencing Mg degradation in physiologically relevant environments (Figure 2.1); those interactions can be as important as the factors themselves. The specific aims of this section were:

1. Determine the effects of alloy composition, alloy processing, and physiological salt ions upon Mg alloy degradation.
    a. The presence or absence of a Y alloying component was investigated because it is the subject of much scrutiny for diverse applications, from biomedical to automotive and aerospace.
    b. The metallic and thermal oxide surface types were investigated because they are both common surface types for metallic implants.
    c. The presence or absence of physiological salt ions was investigated because they are known to profoundly affect Mg degradation.
2. Determine if these factors influence Mg alloy degradation independently or through interactions with each other.

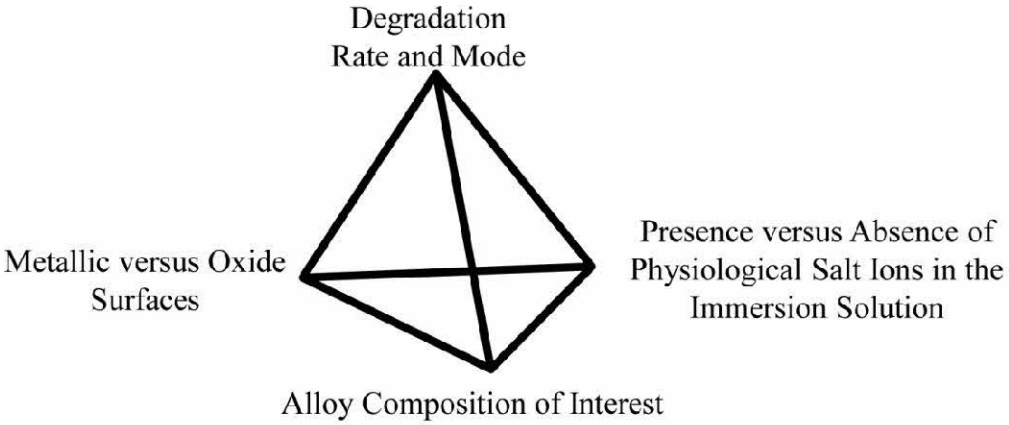

Figure 2.1: Mg degradation rate and mode are influenced by multiple interacting factors that include: alloy composition, surface type, and physiological salt ions.

2.2- Materials and Methods

2.2.1- Preparation of Pure Mg and Mg-Y Alloy Samples

Commercially pure Mg foil (Goodfellow Corporation, as-rolled, 99.9% purity) with a thickness of 250μm was used as a control in this study. The as-rolled Mg foil had a thermal oxide layer on its surface and was called cpMg_O, with "cp" indicating commercially pure and "O" indicating the presence of the thermal oxide layer on its surface. Some of the cpMg_O samples were ground sequentially using 600, 800, and 1200 grit silicon carbide abrasive papers (PACE Technologies) to remove the oxide layer on the surface, and were referred to as cpMg in this study. The term cpMg* was used to refer to both cpMg_O and cpMg.

Mg-4 wt.% Y alloy was prepared by melting magnesium with 4 wt.% Y in an argon protected environment and casting as an ingot. The as-cast My-Y alloy ingot was cut into 250μm thick discs using a wire electric discharge machine (AgieCharmilles, Agiecut 200 VHP). The as-produced alloy discs had thermal oxide layers on their surfaces and were called MgY_O in this study. Some of the MgY_O samples were ground sequentially using 600, 800, and 1200 grit silicon carbide abrasive papers to remove the thermal oxide layer from the surface, and were referred to as MgY in this study. MgY* was used to refer to both MgY_O and MgY in this manuscript.

All of the cpMg* and MgY* samples in this study were cut into dimensions of 10 mm x 10 mm, cleaned in isopropanol (Sigma-Aldrich, CAS number 67-63-0), and weighed. Both sides of the samples were disinfected under ultraviolet (UV) radiation for at least 8 hours before degradation experiments.

2.2.2- Degradation of cpMg* and MgY* in Immersion Solution

Degradation of cpMg* and MgY* was investigated by the immersion method. Briefly, both cpMg* and MgY* samples were immersed in two different immersion solutions for comparison: deionized (DI) water and phosphate buffered saline (PBS). DI water was produced by a Millipore Milli-Q® Biocel System and used as a control. PBS was prepared by dissolving 8 g NaCl, 0.2 g KCl, 1.5 g Na_2HPO_4, and 0.2 g KH_2PO_4 in 1000 ml of DI water and adjusting the pH to 7.4 (all chemicals from Sigma). PBS was chosen as one of the immersion solutions in order to determine the effects of aggressive physiological ions (e.g. Cl^-) on Mg degradation. Both PBS and DI water were sterilized by autoclaving. Immersion occurred under standard cell culture conditions (a 37 ºC, 5% CO_2 / 95% air, humidified, sterile environment) without stirring. Each sample was immersed in 3 mL of solution.

All cpMg* and MgY* samples were incubated in DI water and PBS according to the prescribed sequential time points. The incubation time was shorter (1 hour) at the beginning of the degradation experiment to provide a higher time resolution. A higher time resolution was necessary to track the initially rapid changes to the sample mass and the pH of immersion solution. Furthermore, the alloy degradation rate and local pH both have profound effects on cell survival and functions during the early stage of implantation. After 3 days of immersion, the incubation time was increased to 48 hours (2 days) to mimic normal cell culture conditions. When the prescribed incubation time ended, the samples were removed from their immersion solution and dried in a 37 ºC isotemp oven for 12 hours, or until the sample reached a constant mass. Degradation

products that precipitated on the surface of the cpMg* and MgY* samples were left intact, while soluble degradation products remained in the immersion solution. The pH meter was first calibrated with known standards, and then used to measure the pH of the immersion solution at the end of every prescribed incubation time. The samples were dried, weighed, photographed, disinfected under UV radiation, and then placed in fresh immersion solution for the next incubation time. The same procedure was repeated for each prescribed incubation time. When the sample mass was reduced to less than 3 mg, they became too small to handle and thus were considered as completely degraded at the next time point. The mass of the samples after each incubation time (M_i) was divided by its initial mass (M_0) to obtain the normalized mass change (M_i/M_0). The degradation tests were performed in triplicate for each sample type.

2.2.3- Statistical Analysis of Degradation Data

The three factors that control the dependent variable (i.e., sample degradation) were alloy composition (cpMg or MgY), sample surface (metallic or oxide), and immersion media (DI water or PBS). Factorial ANOVA was used to analyze the effects of these factors on the sample degradation. The Shapiro-Wilks test was used to verify that the data had a normal distribution. The Bartlett test was used to verify that the different sample groups had homogeneous variance. A significance level of $\alpha=0.05$ was used for all statistical tests. Two-way interaction plots were generated to illustrate the interactions between all possible combinations of the factors. All the statistical tests were performed using R.

2.2.4- Surface Characterization of cpMg* and MgY*

The cpMg* and MgY* samples were disinfected under UV radiation, and then incubated in DI water and PBS under standard cell culture conditions (37 ºC, 5% CO_2 / 95% air, humidified sterile environment) for 24 hours. After that, the samples were taken out of the immersion solution and dried in a vacuum oven at room temperature for 2 days. The surfaces of cpMg* and MgY* samples were characterized before and after 24 hours of degradation using a field emission scanning electron microscope (FESEM; Philips XL-30). Energy dispersive X-ray spectroscopy (EDX) analysis was performed with an accelerating voltage of 15 kV and an original magnification of 2500X to determine the elemental composition of the sample surface. Three different areas for each sample type were examined using EDX, and the results were averaged.

2.3- Results

2.3.1- Degradation of the cpMg* and MgY* Samples in DI Water

2.3.1.1- Appearance of Samples after Degradation in DI Water

The surface of cpMg_O (Figure 2.2A) did not show significant change until the 3rd day of degradation in DI water. Dark-colored degradation products appeared on one side of the sample at the 3rd day and progressed across the entire surface by the 5th day. The degradation layer appeared gray and relatively homogeneous to visual inspection after the 5th day. The degradation of samples initiated from the edges that slowly migrated inward while leaving behind a smooth contour. The surface of cpMg (Figure 2.2B) did not show significant change until the 2nd day of degradation in DI water. Dark-

colored degradation products appeared on one side of the sample and then progressed across the entire surface by the 3rd day. The cpMg degradation mode was similar to that observed on cpMg_O in DI water. The samples degradation began at the edges and migrated inward. In contrast, the surface of MgY_O (Figure 2.2C) turned dark after only 1 hour of incubation in DI water. Localized gray degradation products gradually accumulated on the sample surface until the entire surface became dark gray by the 3rd day. MgY_O shed fragments and lost structural integrity by day 11 and completely degraded after 19 days. The degradation mode of MgY (Figure 2.2D) appeared similar to MgY_O. Most of the visible degradation of MgY occurred between 5 and 7 days, and MgY completely degraded after 9 days. MgY degraded much more rapidly than the other sample types in DI water.

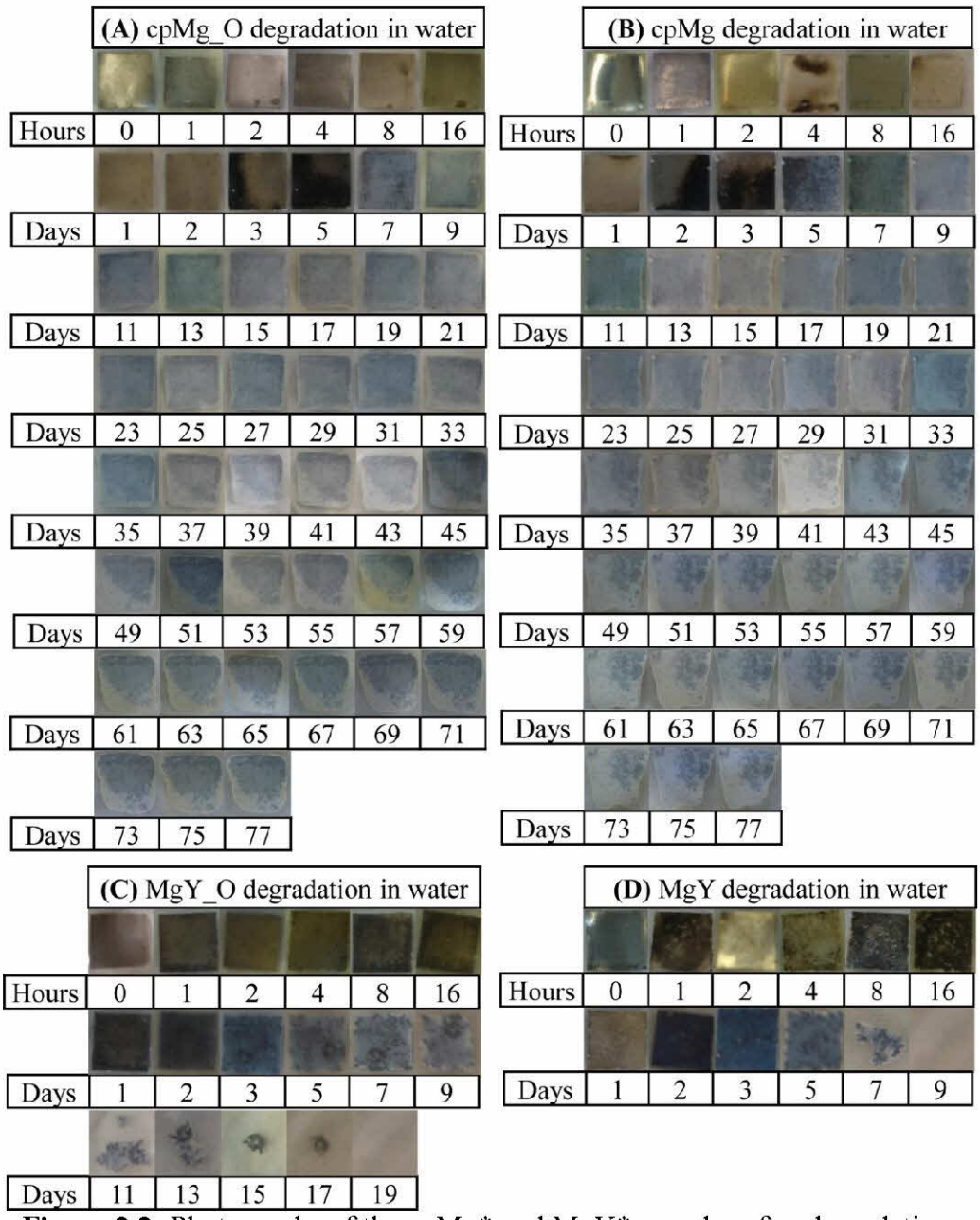

Figure 2.2: Photographs of the cpMg* and MgY* samples after degradation in DI water. Samples were incubated in DI water under standard cell culture conditions for the prescribed time points.

2.3.1.2- Changes to Sample Mass and pH of DI water

Figure 2.3 shows the mass change of the samples in DI water. The mass of cpMg_O samples was constant for the first 3 days of incubation in DI water, followed by slight mass loss between 3 and 5 days, slight mass gain between 5 and 9 days, and then slow mass loss for the rest of the study. The cpMg_O and cpMg samples had similar mass loss at each time point. However, MgY* degraded much more rapidly than cpMg* in DI water. MgY* had constant mass between 0 and 16 hours of incubation in DI water, followed by rapid mass loss. MgY had even more rapid mass loss than MgY_O, and the entire MgY sample was gone after 9 days of immersion.

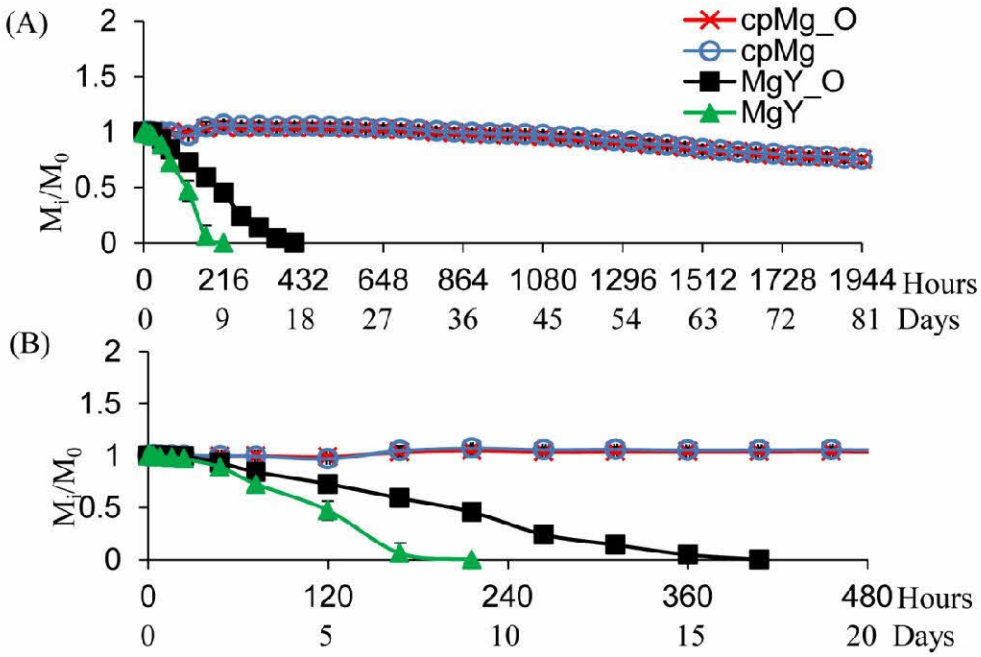

Figure 2.3: Sample mass change during degradation in DI water. M_i was the mass after the prescribed incubation time (i) and M_0 was the initial mass. (A) Sample mass for all time points in the study. (B) Sample mass for only the time points from 0 to 480 hours.

Figure 2.4 shows the pH change of DI water after sample immersion. Degradation of cpMg_O caused a rapid pH increase in DI water to 9.2 during the first 24 hours, and then the pH gradually decreased. Between 9 and 29 days, the pH of DI water stabilized in the range of 8.0 to 8.4. The cpMg degradation resulted in pH changes similar to cpMg_O, with a few exceptions at the early stage and at the end. The DI water containing cpMg was slightly more alkaline than cpMg_O at some time points. The DI water containing MgY_O reached its maximum pH of 9.29 during the first 2 hours of incubation, and the pH reached a plateau at 8.4 afterwards until 13 days of incubation. After 13 days, the pH decreased to 7.64 due to the significant reduction of the remaining sample material. MgY degradation resulted in a similar pH trend as MgY_O, except it slightly more alkaline during the first 4 hours.

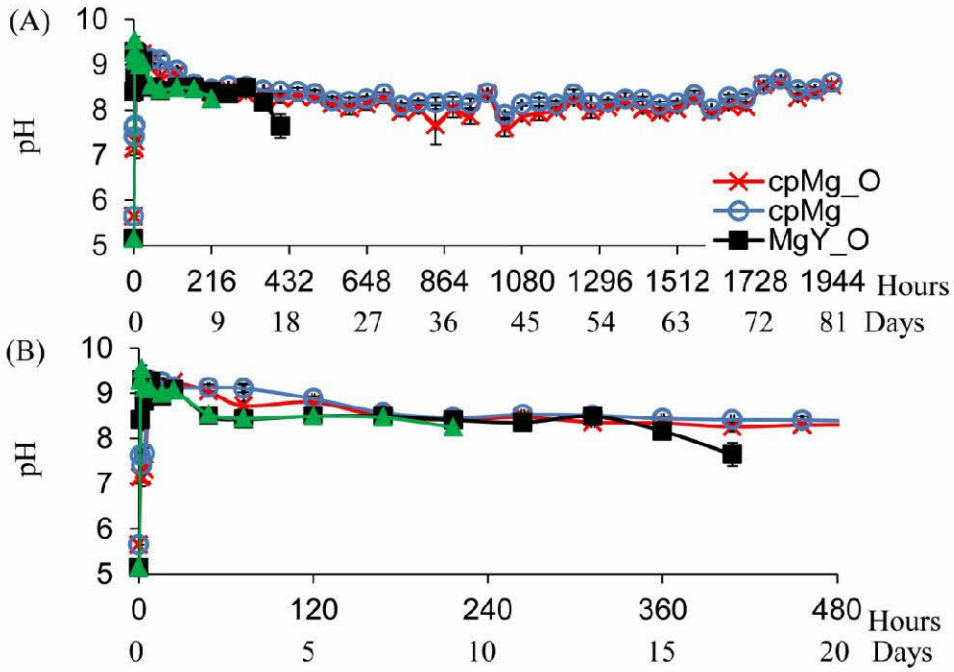

Figure 2.4: Sample pH change during degradation in DI water. (A) DI water pH for all time points in the study. (B) DI water pH for only the time points from 0 to 480 hours.

2.3.2- Degradation of the cpMg* and MgY* Samples in PBS

2.3.2.1- Appearance of Samples after Degradation in PBS

Rough and heterogeneous gray degradation products accumulated on the surfaces of cpMg_O after immersion in PBS for only 1 hour (Figure 2.5A). Once the degradation products covered the entire surfaces after 3 days, accumulation of white degradation products appeared near the center of the samples. The cpMg_O samples fragmented at the center on day 9, the large fragments continued to degrade and eventually dissolved after 23 days. In Figure 2.5B, similar degradation products accumulated on the surfaces of cpMg and spread at a similar rate. The cpMg samples fragmented near the center at day 5 and the remaining fragments continued to degrade until they completely dissolved after 27 days. In Figure 2.5C, white degradation products accumulated at the edges of MgY_O samples after immersion in PBS for 1 hour. The degradation layer was rough, porous, and heterogeneous; and it migrated inward from the edges until it covered the entire surface. MgY_O continuously shed fragments from its edges after 16 hours and completely degraded after 3 days. As shown in Figure 2.5D, localized white degradation products appeared on the surfaces of MgY after 1 hour of incubation in PBS and spread over entire surfaces in 2 days. The MgY samples started to release fragments from their edges after day 5 and completely degraded after 29 days.

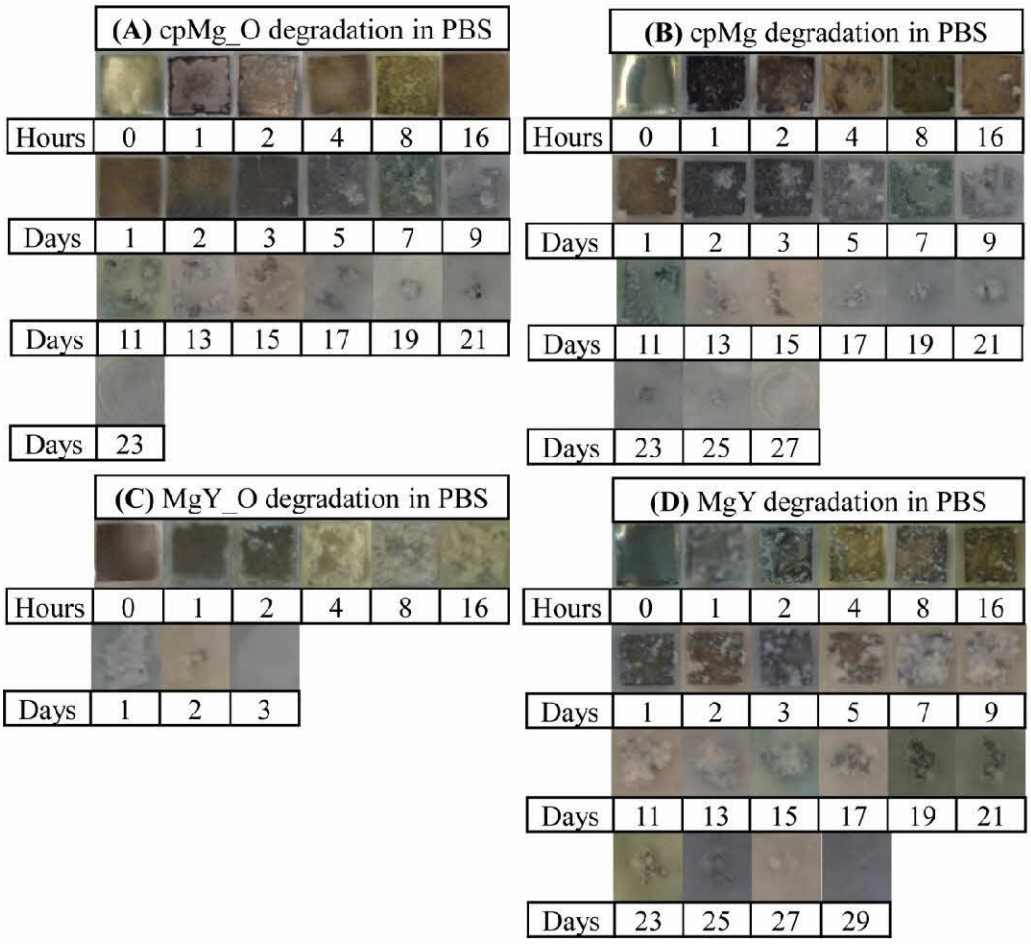

Figure 2.5: Photographs of the cpMg* and MgY* samples after degradation in PBS. Samples were incubated in PBS under standard cell culture conditions for the prescribed incubation times.

2.3.2.2- Changes to Sample Mass and pH of PBS

Figure 2.6 shows the mass changes of the samples in PBS. The mass of cpMg_O remained constant for the first 2 days, slightly increased until day 5, and rapidly decreased afterwards. The mass change of cpMg over time was similar to that of cpMg_O, with a few exceptions. For example, cpMg reached its peak mass in a shorter time (i.e., 2 days) and that peak lasted slightly longer than cpMg_O. Interestingly, MgY_O immersed in PBS reached its peak mass first, and showed the most rapid mass

loss among all the samples tested. The MgY samples had a higher peak mass than the cpMg* samples in PBS, but took longer to reach that peak mass. After reaching its peak mass, the mass of MgY started to decrease gradually.

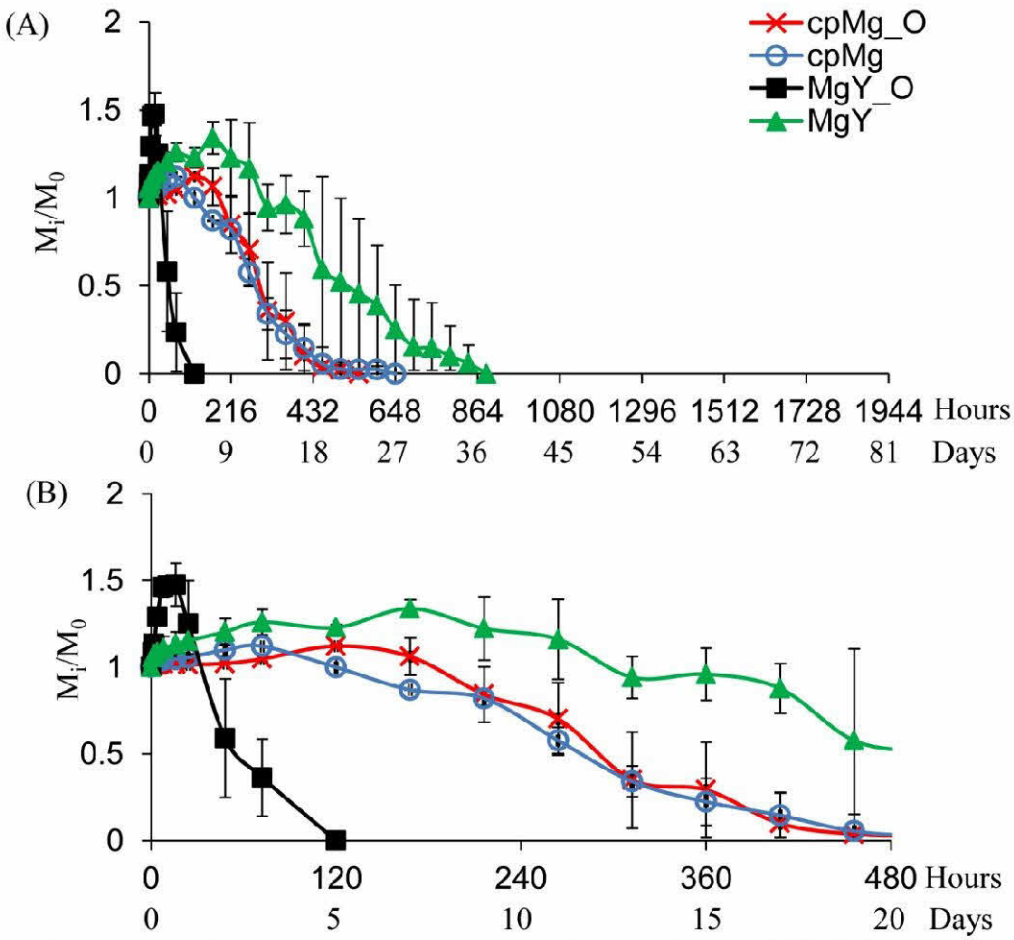

Figure 2.6: Sample mass change during degradation in PBS. (A) Sample mass for all time points in the study. (B) Sample mass for only the time points from 0 to 480 hours.

Figure 2.7 shows the pH change of PBS after sample immersion. The pH of PBS with immersed cpMg_O reached its maximum of 8.73 after 5 days of incubation, remained at that plateau until 13 days, and then slowly decreased to 7.62. The PBS containing cpMg had the same pH plateau as cpMg_O, although the plateau was reached

slightly earlier. The pH of the PBS containing MgY_O rapidly increased to 8.90 during the first hour, and then decreased slightly to around 8.40 until the samples degraded entirely. The pH of the PBS containing MgY rapidly increased to 8.2 during the first hour of incubation, reached its peak value of 8.49 at 5 days, and then continually decreased to 7.13 at the end.

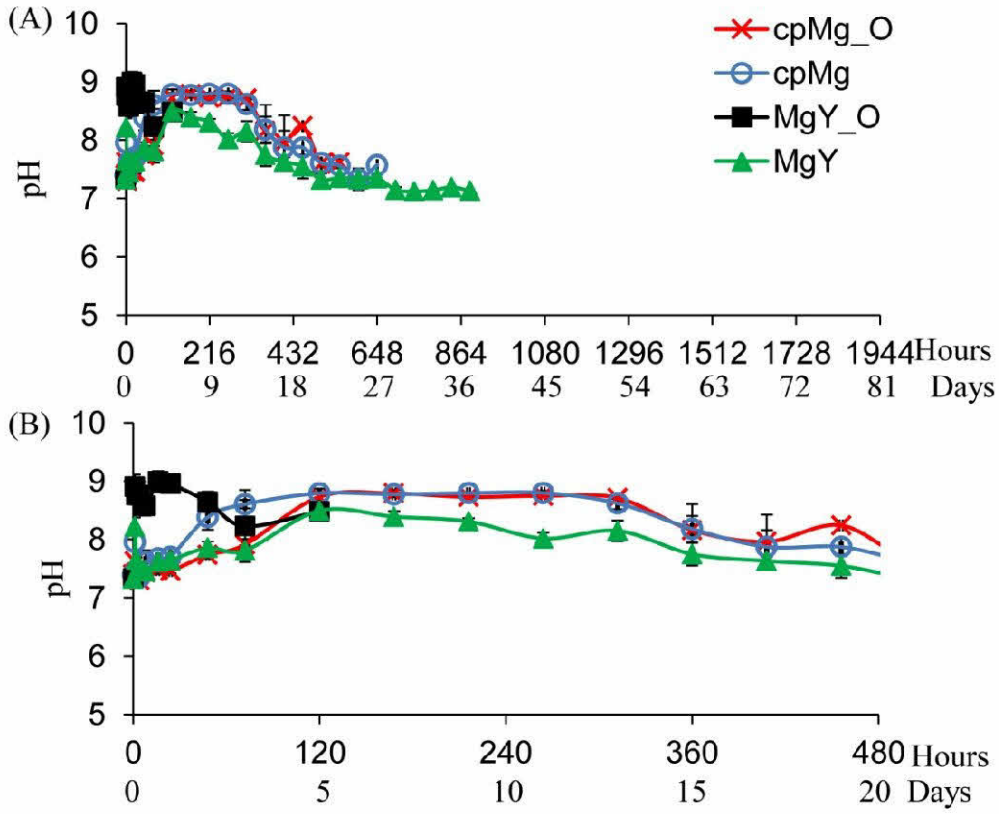

Figure 2.7: Sample pH change during degradation in PBS. (A) PBS pH for all time points in the study. (B) PBS pH for only the time points from 0 to 480 hours.

2.3.3- Statistical Analysis of Mass Loss during Degradation

There were significant interactions among alloy composition, sample surface type, and immersion media, as demonstrated through factorial ANOVA analysis. The

mass and pH data did not have homogenous variance, and thus were not suitable as the dependent variables for ANOVA. Therefore, the log (sample lifetime) was introduced as the dependent variable because it had normal distribution and homogenous variance, which met the criteria for factorial ANOVA. The sample lifetime was defined as the time point when the sample was considered as completely degraded or its residual mass was less than 3 mg. The lifetime of the samples that never fully degraded (i.e., cpMg* in DI water) by the end of the degradation study (i.e., 1944 hours) were calculated based on their maximum degradation rate recorded in the study.

Alloy composition, sample surface type, and immersion media all had statistically significant effects on sample lifetime, as shown in Table 2.1; with values of $p=1.10\text{x}10^{-13}$, $p=4.37\text{x}10^{-2}$, and $p=2.87\text{x}10^{-11}$ respectively. Furthermore, statistically significant two way interactions were observed between alloy composition and sample surface ($p=2.95\text{x}10^{-4}$), alloy composition and immersion media ($p=4.45\text{x}10^{-11}$), and sample surface and immersion media ($p=3.47\text{x}10^{-8}$). A statistically significant three way interaction was also observed between alloy composition, sample surface, and immersion media ($p=1.03\text{x}10^{-5}$).

Table 2.1: Statistical analysis of Mg* and MgY* degradation. Provides *p* values calculated using the factorial ANOVA test that compared the effects and interactions of three factors (alloy composition, sample surface, immersion media) upon sample lifetime.

Factorial ANOVA	Alloy	Surface	Media	Alloy: Surface Interaction	Alloy: Media Interaction	Surface: Media Interaction	Alloy: Surface: Media Interaction
p value	$1.10\text{x}10^{-13}$	$4.37\text{x}10^{-2}$	$2.87\text{x}10^{-11}$	$2.95\text{x}10^{-4}$	$4.45\text{x}10^{-11}$	$3.47\text{x}10^{-8}$	$1.03\text{x}10^{-5}$

Two-way interaction plots graphically demonstrate the relationships among the three factors and their combined effects on the log (sample lifetime), as shown in Figure 2.8. The different values for one factor are presented along the X axis, while the Y axis represents the log (sample lifetime). Two different lines in each plot present the different values for the second factor. The relationships between these two factors are further affected by the third factor and are thus plotted side by side for comparison. Figure 2.8A had two almost parallel lines with negative slopes for the left plot, and a "<" shape with one positive and one negative slope for the right plot. Figure 2.8B had two almost parallel lines with negative slopes for the left plot, and an intersected "X" shape with one positive and one negative slope for the right plot. Figure 2.8C had a "<" shape with two positive slopes for the left plot, and an intersected "X" shape with one positive and one negative slope for the right plot. The slopes of these lines, as well as the angles and types of intersections revealed the interactions among three factors. Interaction plots with two intersected lines showed substantial interaction between the two factors, while those with parallel lines showed no interaction between the two factors. A "<" shape showed consistent interactions between the two factors, while an "X" shape demonstrated that the interactions between the two factors had opposite effects at different values.

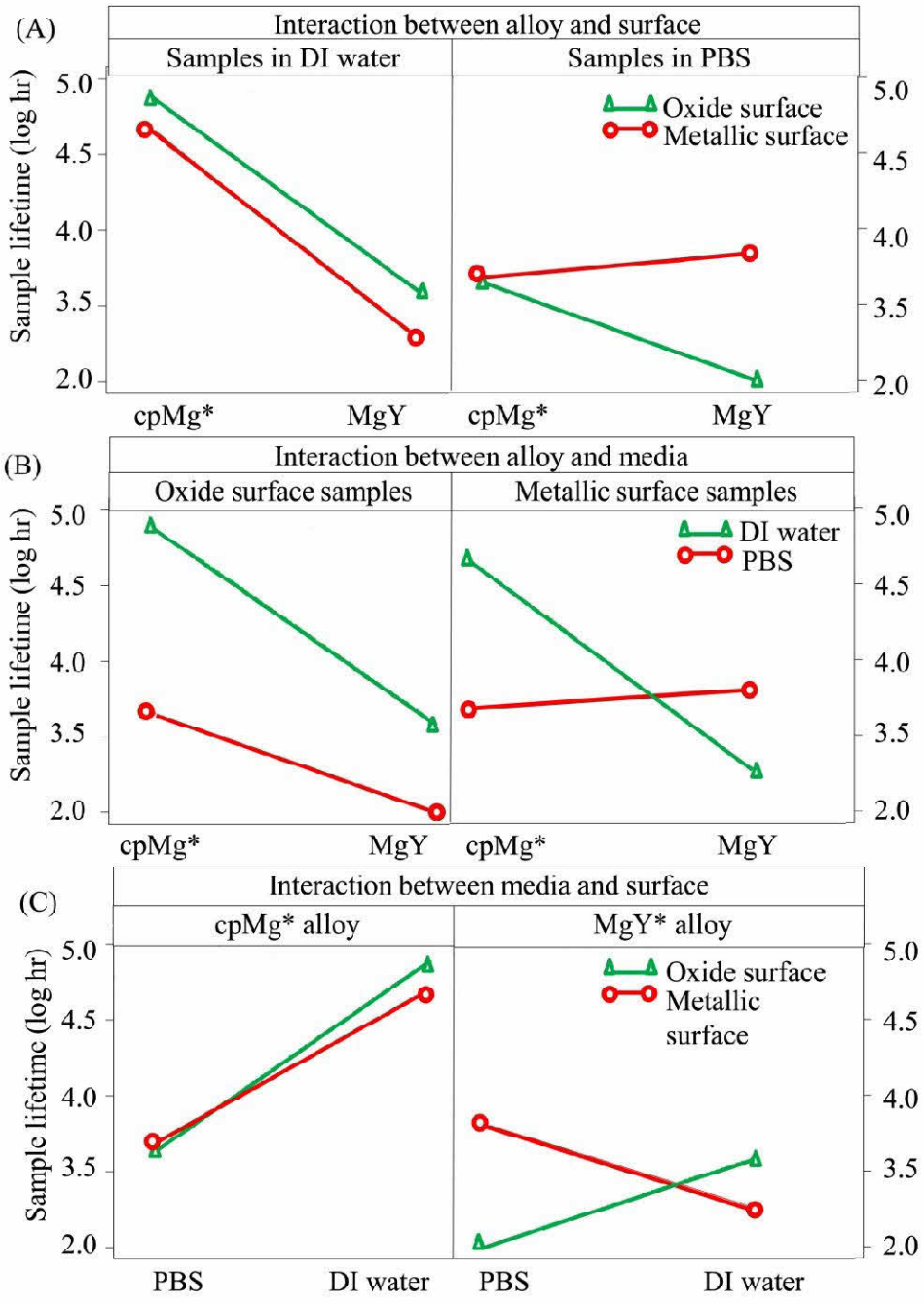

Figure 2.8: Interactions between three key factors that influence Mg* and MgY* lifetime. Two separate interaction plots with different levels of a third factor were placed side by side for comparison; the level of the third factor is shown directly below the graph title. (A) Alloy and surface with media as the third factor. (B) Alloy and media with surface as the third factor. (C) Media and surface with alloy as the third factor.

2.3.4- Surface Microstructure and Composition of cpMg* and MgY* Before and After Degradation

Scanning electron micrographs (Figure 2.9) showed that cpMg_O initially had a rough surface without cracks, MgY_O had a rough surface with cracks, and cpMg and MgY had relatively smooth surfaces with grooves from grinding. Incubation in DI water and PBS both resulted in cracks and formation of degradation products on the surfaces of all samples. Incubation in PBS also caused formation of degradation products with a network-like morphology on the samples with metallic surfaces.

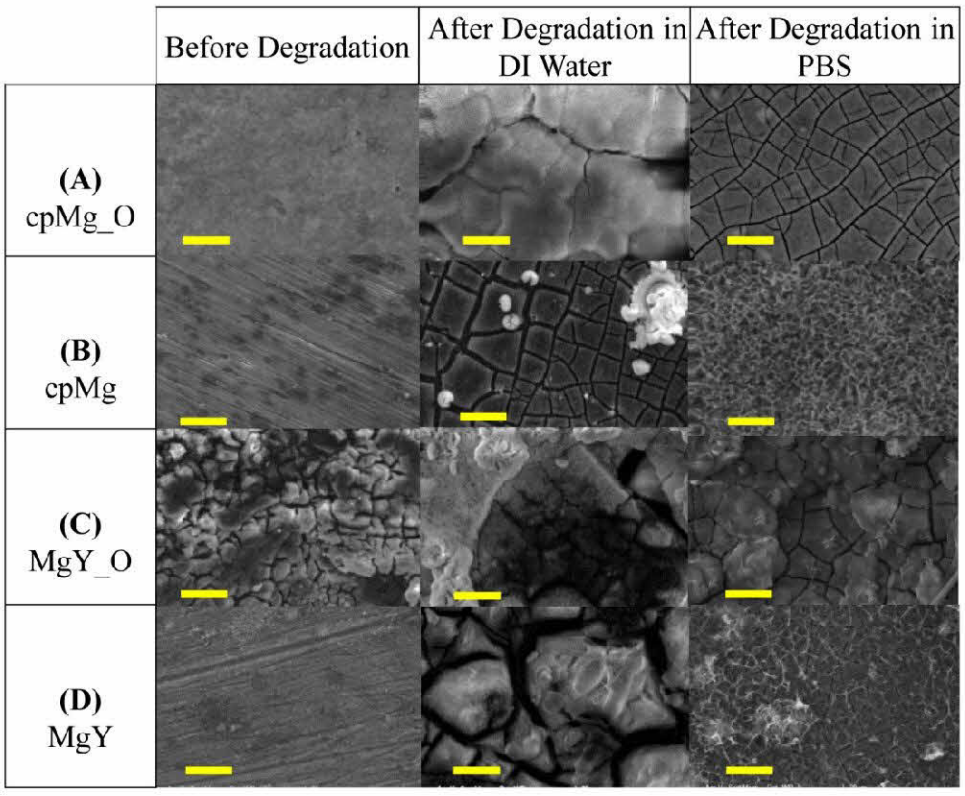

Figure 2.9: Mg* and MgY* surface microstructure before and after degradation. Scanning electron micrographs of the (A, B) cpMg* and (C, D) MgY* samples before and after 24 hours of degradation in either DI water or PBS. Scale bars: 20μm.

EDX analysis (Table 2.2) showed that alloy composition (MgY* versus cpMg*), initial surface condition (metallic versus oxide), and immersion solution (DI water versus PBS), all affected the surface composition after degradation. Degradation layers on the samples incorporated additional elements from the immersion media. All the cpMg* and MgY* samples incorporated more carbon (C) onto their surface in DI water than they did in PBS. Before degradation, the MgY_O samples had 5.20±0.71 wt.% Y on the surface and the MgY samples had 3.39±0.72 wt.% Y, both close to theoretical value of 4 wt.% Y. After degradation, Y percentage decreased on the surface of MgY_O samples in both DI water and PBS. In contrast, Y percentage increased on the surface of MgY in DI water.

Table 2.2: Effects of degradation upon Mg* and MgY* surface composition. The surface elemental composition of the cpMg* and MgY* before and after 24 hours of degradation in DI water or PBS, as determined by EDX at a 15 kV accelerating voltage.

(A) cpMg_O	Before degradation	Degradation in DI water	Degradation in PBS
Element	At%	At%	At%
C	0	21.51±0.16	9.86±0.80
O	12.80±0.86	57.95±0.13	49.75±1.53
Na	0	0	8.78±1.03
Mg	87.19±0.86	20.52±0.03	21.28±1.43
P	0	0	9.93±0.39
Cl	0	0	0.38±0.66

(B) cpMg	Before degradation	Degradation in DI water	Degradation in PBS
Element	At%	At%	At%
C	0	20.09±1.60	12.57±0.43
O	10.96±2.42	49.54±3.08	53.18±0.97
Na	0	0	6.53±0.79
Mg	89.03±2.42	30.36±1.57	17.42±1.12
P	0	0	8.40±0.61
Cl	0	0	1.88±0.73

(C) MgY_O	Before degradation	Degradation in DI water	Degradation in PBS
Element	At%	At%	At%
C	16.56±3.05	12.72±1.96	10.45±9.07
O	55.63±1.53	58.27±0.94	55.81±4.85
Na	0	0	10.14±1.24
Mg	26.68±1.71	28.36±3.66	14.91±1.60
Y	1.11±0.13	0.63±0.44	0.35±0.05
P	0	0	8.11±1.13
Cl	0	0	0.07±0.06

(D) MgY	Before degradation	Degradation in DI water	Degradation in PBS
Element	At%	At%	At%
C	0	25.85±0.89	13.58±0.44
O	18.98±0.54	52.23±1.37	47.57±1.43
Na	0	0	11.28±0.59
Mg	80.12±0.37	19.78±1.58	18.36±0.68
Y	0.89±0.19	2.12±1.01	0.91±0.20
P	0	0	7.25±0.64
Cl	0	0	1.02±0.62

2.4- Discussion

2.4.1- Surface Type and Alloy Composition Influenced Degradation in DI Water

The results of this study confirmed that both composition (alloying with Y versus pure Mg) and surface (metallic versus oxide) influenced the degradation in DI water. The surface effects were more pronounced for MgY* than for cpMg* samples in DI water, as demonstrated in Figures 2.2 and 2.3. The initial alkalinity in the DI water containing cpMg was caused by the degradation reactions. A protective thermal oxide layer was already present on cpMg_O, so reaction 1a was less prevalent initially. A more uniform degradation layer formed on cpMg* in DI water due to more uniform microstructure of the pure Mg. As a result, free corrosion (general dissolution of Mg) rather than pitting corrosion was the dominant corrosion mechanism for the cpMg* samples in DI water, as shown in Figure 2.2. In free corrosion mode, cpMg* degraded gradually without sudden fragmentation. The addition of Y as an alloying element accelerated the degradation in DI water. Yttrium had a net degradation promoting effect on MgY* in DI water due to instability of the degradation layers, as demonstrated by release of surface fragments from the samples. MgY_O degraded more slowly than MgY in DI water because the thermal oxide layer provided better protection as compared to the degradation layer formed by reaction 1.

2.4.2- Surface Type and Alloy Composition Influenced Degradation in PBS

It is still true that both surface (metallic versus oxide) and composition (alloying with Y versus pure Mg) influenced the degradation in PBS. The surface effects were still

more pronounced for MgY* than for cpMg* samples in PBS, as shown in Figures 2.5 and 2.6. In PBS, penetrating and undermining by Cl^- ions changed the degradation mode of cpMg* from free corrosion to localized corrosion. Cl^- attack also increased localized corrosion on MgY*. MgY was the only sample that lasted longer in PBS than in DI water, possibly because a more stable degradation layer was able to form on the MgY surface by incorporating protective constituents from PBS.

The importance of surface and composition, as well as presence of physiological ions on degradation was demonstrated in Figure 2.10. The maximum degradation rates of cpMg* and MgY* were calculated using the Equation 2.1 below and the mass change data.

$$Degradation\ Rate = \Delta Sample\ Mass / Sample\ Surface\ Area\ / \Delta Time \quad \text{Eq 2.1}$$

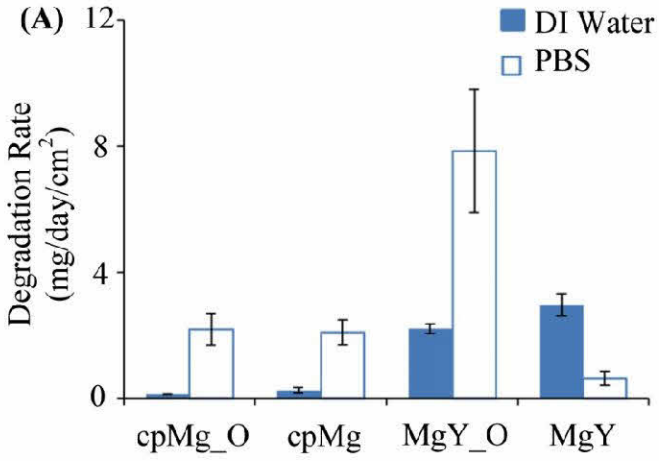

(B) Samples	Maximum Degradation Rate (mg/day/cm^2)	
	In DI Water	In PBS
cpMg_O	0.12±0.00	2.18±0.51
cpMg	0.25±0.09	2.08±0.39
MgY_O	2.20±0.15	7.84±1.95
MgY	2.96±0.35	0.56±0.25

Figure 2.10: Mg* and MgY* degradation rates in DI water and PBS. The maximum degradation rates of cpMg* and MgY* samples in DI water and in PBS were calculated based on sample mass loss using Eq 1. Values are average ± standard deviation; N=3.

Considering that cpMg_O had a similar degradation rate as cpMg either in DI water or PBS, the metallic or oxide surfaces did not have significant effects on degradation of pure Mg. However, MgY degraded faster than MgY_O in DI water and vice versa in PBS. This indicated that surface condition (with or without oxide layer) and composition of immersion solution (with or without physiological ions) both had significant effects on the degradation of MgY*. In other words, the protective surface barrier formed by Y passivation was influenced by both the initial surface microstructure and the composition of the immersion solution.

2.4.3- Interactions Between Surface Type, Alloy Composition, and Immersion Media Influenced Degradation

Alloy composition, alloy surface type, and immersion media type significantly affected the sample degradation rates not only as factors acting separately, but also as factors interacting with each other. This was confirmed in Table 2.1 by the low p values for each individual factor, the two-way interactions, and the three-way interaction.

The interaction plots graphically demonstrated significant interactions between the three factors upon the sample lifetime (Figure 2.8). The almost parallel slopes in the left plot of Figure 2.8A suggested that the alloy:surface interaction was minor in DI water, while the intersections in the left plot showed the alloy:surface interaction was significant in PBS. The negative slope for the combination of Y alloy component, metallic surfaces, and DI water indicated that the metallic surface decreased MgY sample lifetime in DI water. Conversely, the negative slope for the combination of Y alloy component, oxide surface, and PBS indicated that the oxide surface decreased MgY_O sample lifetime. The positive slope for the MgY in PBS indicated that the combination of MgY and metallic surface prolonged sample lifetime in PBS.

In Figure 2.8B, the angle between the slopes on the left plot indicated some observable alloy:media interaction for samples with oxide surface, and the negative slopes indicated that cpMg had a longer sample lifetime than MgY in either media when samples had oxide surfaces. The "X" shaped slopes on the right indicated significant interaction between alloy and media for samples with metallic surfaces. The "X" shape indicated that sample lifetime was longer for cpMg and shorter for MgY in DI water, but

vice versa in PBS. This suggested that the degradation behavior of magnesium alloys could be reversed by different physiological conditions (e.g. concentration of salt ions). Because of this important implication, the design of a biodegradable material must be tailored for specific anatomical locations or specific environmental conditions in the body.

In Figure 2.8C, the small angle between the slopes on the left plot indicated little media-surface interaction for cpMg* samples, and the positive slopes indicated that cpMg* had a longer lifetime in DI water than PBS. The larger angle between the slopes on the right plot indicated significant interaction between media and surface for MgY* samples. The "X" shape for the right plot showed that MgY_O had a shorter lifetime in PBS and a longer lifetime in DI water, but vice versa for MgY.

Understanding the interactions that control Mg degradation is a crucial step in developing Mg alloys as biodegradable implant materials. Physiological fluids are rich in aggressive ions that not only interact with alloy and surface directly, but also alter the effects of alloying and surface on degradation behavior. These interactions must be taken into account when designing biodegradable implants.

2.4.4- Surface Microstructure and Elemental Composition Influenced Degradation

SEM images showed that the surfaces of cpMg_O, cpMg, and MgY were free of cracks initially, which limited penetration of aggressive Cl^- ions. In contrast, MgY_O had a significantly cracked surface initially, which increased its vulnerability to aggressive Cl^- ions. All cpMg* and MgY* samples had cracked surfaces after incubation in DI water. The thermal oxide layer on the MgY_O surface provided some initial protection from

degradation in DI water, but the cracked surface exposed the underlying metallic substrates to Cl^- ions. Electrochemical transport processes concentrated Cl^- ions in the cracks, which caused severely undermined the oxide layer. Therefore, the thermal oxide surface protected MgY_O in the fluid lacking aggressive ions (i.e., DI water), but accelerated the degradation in the fluid containing aggressive ions (i.e., PBS). The loss of the oxide layer at some sites led to localized corrosion cells that continued to propagate. Continuous propagation of the localized corrosion cells may have prevented the formation or maintenance of a protective layer on the MgY_O surface. Thus, MgY_O degraded the most rapidly in PBS.

MgY and cpMg initially had metallic surfaces without surface oxide layers or cracks. Because of this, their degradation was distributed across the entire sample surface rather than concentrated along cracks. Moreover, the initial degradation products formed a network-like morphology on MgY and cpMg in PBS (Figure 2.9). This network morphology of degradation products may have protected the surface underneath and physically restrained the release of large surface fragments, which limited the propagation of localized corrosion. As a result, a protective degradation layer was able to form on the metallic surfaces of MgY and cpMg and their degradation was slower than the respective samples with oxide surfaces in PBS. Eventually, MgY broke into fragments because the propagation of localized corrosion became too severe to keep the protective degradation layer intact.

Surface elemental composition played an important role in determining the susceptibility of samples to degradation. The relative amount of Y decreased on the

surface of MgY_O after 24-h exposure to either immersion solution. MgY_O incubated in PBS had the lowest relative Mg content on the surface and the largest mass gain among all the samples. The low percentage of Mg on the surface prevented the formation of an effective degradation layer in PBS. The absence of a stable surface layer compromised the protective effects of Y and other protective components like carbonate or phosphate. In contrast to MgY_O, the MgY surface became Yenriched after degradation in DI water. MgY degraded the slowest in PBS because the degradation layer containing protective elements (e.g. carbonates) might have provided a more stable protection than surface oxides. Due to the more stable degradation layer, it took Cl^- ions longer to penetrate and undermine the surface. Eventually however, the degradation layer was undermined so severely that it provided little protection. Therefore, after reaching the peak mass, the slope of MgY mass loss was similar as cpMg in PBS.

2.5- Conclusions of Chapter 2

This investigation demonstrated that the alloy composition, surface type, and immersion media interacted with each other to influence Mg degradation. Specifically, the Y alloy component promoted degradation of Mg in DI water for either surface type. In PBS however, the Y alloy component inhibited degradation of the Mg alloy with the metallic surface, but promoted degradation of that same alloy with the thermal oxide surface. This study disentangled the complex relationship between these factors and their respective contributions to Mg degradation for the first time, and also presented design considerations for Mg based implants and devices.

Chapter 3- Nanocomposite Coatings Reduce Mg Degradation

3.1- Specific Challenges and Aims

Alloy composition and processing are critical to controlling Mg alloy degradation, but they are only part of the solution. Coatings can work in conjunction with alloy composition and processing; and can perform multiple functions simultaneously, such as controlling Mg degradation and improving cell adhesion. Composite materials are of interest for coatings because they can have properties that are difficult to obtain with single-phase materials.

The specific aims of this section were:

1. Develop nHA/PLGA nanocomposite coatings for controlling Mg substrate degradation.
2. Characterize the effects of the nHA/PLGA coatings upon Mg substrate degradation.
    a. Quantify the degradation rate of nHA/PLGA coated Mg in a simulated *in vivo* environment.
    b. Characterize the changes to the coatings during degradation.
    c. Identify challenges that limit the functionality of the coatings. These challenges will be resolved in a subsequent study.

3.2- Materials and Methods

3.2.1- Preparation and Characterization of Mg Substrates and the Controls

Mg, AZ31 alloy, and commercially pure Ti were prepared as the substrates for the coating processes. Specifically, a 1-mm thick Mg plate (97% purity; Miniscience), a 1-mm thick AZ31 plate (Alfa Aesar), and a 0.5-mm thick Ti plate (Alfa Aesar) were ground sequentially using 600, 800, and 1200 grit silicon carbide abrasive papers (Ted Pella) to remove the oxide layers on the surface. Ethanol (200 proof; Koptec) was used to lubricate the plates during grinding and wash away particulate debris. The plates were cut with a notcher (no. 100, Whitney Metal Tool Co.) into 10 x 10 mm squares. The four edges of each substrate were then ground in the same way as described above. All the substrates were cleaned in ethanol under sonication (Symphony™ Ultrasonic Cleaners, VWR) for 15 min. Before coating processes, the Mg substrates were examined using a field emission scanning electron microscopy (SEM; XL30-FEG, Philips) at an accelerating voltage of 15 kV.

3.2.2- Preparation and Characterization of nHA

The nHA was synthesized using a wet chemistry precipitation method followed by hydrothermal treatment. Briefly, a 1 M calcium nitrate [$Ca(NO_3)_2$; Sigma Aldrich] solution with a pH of 10 and a 0.6 M ammonium hydrogen phosphate [$(NH_4)_2HPO_4$; Sigma Aldrich] solution with a pH of 11 were prepared separately at 40°C. Ammonium hydroxide (NH_4OH; Sigma Aldrich) was used to adjust the pH of these solutions. Adding calcium nitrate solution drop wise into the ammonium phosphate solution at 40°C led to

precipitation of calcium phosphate (CaP). The mixture was stirred for an additional 20 hours at 40 °C, and then centrifuged at 10,000 revolutions per min (RPM). After centrifuge, the supernatant was removed and the pellet at the bottom of the centrifuge tube was resuspended in an equal volume of deionized (DI) water. The pellet was washed for 5 times by repeating the steps of centrifuge and resuspending in fresh DI water. After the excess reactants were washed away, the pellet was resuspended in DI water and hydrothermally treated at 200°C for 20 hours in an acid digestion bomb (Parr instruments). After hydrothermal treatment, the nHA was precipitated out of suspension via centrifugation and then dried in vacuum at 80°C. Finally, the dried nHA was ground into a fine powder form using a mortar and pestle. Subsequently, the nHA nanoparticles were used to prepare nHA/PLGA composites for spin coating.

The microstructure and elemental composition of nHA was characterized using a field emission scanning electron microscopy (SEM; XL30-FEG, Philips) and attached energy dispersive x-ray spectroscopy (EDX; EDAX) at an accelerating voltage of 10 kV. The crystal structure of HA was confirmed using x-ray diffraction (XRD; D8 Advance, Bruker AXS), performed at 35 kV and 20 mA with a 0.02° step size.

3.2.3- Spin Coating the nHA/PLGA Nanocomposites onto the Mg Substrates and the Controls

The nHA/PLGA nanocomposite suspension for spin coating was prepared by first dissolving 0.35 g PLGA (50:50, 40-75 kDa; Sigma Aldrich) in 3 mL chloroform ($CHCl_3$, Sigma-Aldrich) at 40°C under low-power sonication (Symphony™ Ultrasonic Cleaner, VWR) for 60 min. After the PLGA was completely dissolved, 0.15 g HA was added into

the PLGA solution at 40 °C under low-power sonication for an additional 60 min. The nHA/PLGA suspension was then sonicated using a high power sonicator (9 W, 20 kHz; Misonix Sonicator S-4000) for 10 min to improve the dispersion of nHA in PLGA. The nHA/PLGA suspension was then degassed in vacuum at room temperature for 5 min.

The same spin coating procedures were used to deposit nHA/PLGA nanocomposites on Mg, AZ31 and Ti substrates. Before spin coating, the clean substrates were first secured on the spin chuck in the spin coater (PWM32, Headway Research). The nHA/PLGA suspension was applied onto the substrates using a disposable borosilicate glass Pasteur pipette (VWR). The substrates were then spun at 300 RPM for 3 min. After spin coating, the substrates were placed in a polytetrafluoroethylene (PTFE) dish with the newly coated side facing up, and dried in air at room temperature for 24 hours. The remaining nHA/PLGA composite suspension was transferred into a PTFE dish, dried in air at room temperature for 24 hours, and saved for coating the other side of the substrates. Once the coated side was dried, the saved nHA/PLGA was re-suspended in chloroform at the same concentration and the opposite side of the substrates was spin coated under the same conditions. After spin coating of the nHA/PLGA nanocomposites onto the top and bottom surfaces, the four edges were dip coated and dried in air at room temperature for 24 hours. After 24 hours of drying in air, the coated substrates were dried in vacuum at room temperature for 48 hours.

The remaining nHA/PLGA solution was cast into a PTFE dish to form a thin film and dried in air for 24 hours followed by vacuum dry for 48 hours at room temperature.

The dried nHA/PLGA film was cut into 10 x 10 mm squares and used as a control for material characterization and degradation experiments.

3.2.4- Spin Coating Pure PLGA onto the Mg Substrates and the Controls

PLGA coatings (without nHA) were deposited onto the Mg, AZ31, and Ti substrates as controls using a spin coating procedure similar to the nanocomposite coatings, except that the PLGA solution was prepared by dissolving 0.45 g PLGA in 3 mL chloroform. The PLGA solution left from spin coating was cast and cut into films, following the same method as for the nHA/PLGA films.

3.2.5- Depositing CaP Control Coating onto the Mg Substrates and the Controls

The CaP coating was deposited onto the Mg substrates as a ceramic control using an immersion method described by Zhang *et al* [121]. A concentrated simulated body fluid (SBF) that had three times more Ca^{2+} and HPO_4^{2-} ions than 1x SBF, called 3CaP SBF, was used for CaP coating process. The prepared Mg substrates were first immersed in 100 mL 3CaP SBF solution at 42°C for 24 hours, and then dried in air at room temperature. The immersion was repeated with the dried substrates in 100 mL fresh 3CaP SBF solution for another 24 hours. Finally, the CaP coated Mg substrates were rinsed with DI water and dried in air at room temperature. This process led to the formation of a low-crystalline apatite coating on the Mg substrates.

3.2.6- Characterization of the Coatings and Controls

The thicknesses of nHA/PLGA coatings and PLGA coatings on the Mg substrates were measured based on the SEM images of the coating cross-sections using ImageJ.

Briefly, the Mg substrates (Goodfellow Corporation, as-rolled, 99.9% purity) with a thickness of 250 μm were spin coated with PLGA or nHA/PLGA composites by following the same procedures described above. The coated substrates were dried in air for 24 hours and in vacuum for 48 hours at room temperature, cut in half with scissors, and mounted onto a 90-degree sample holder for SEM imaging. The coating thickness was measured at the center of each sample and 1mm from the both edges, and then averaged. The average thickness of PLGA or nHA/PLGA coatings was determined based on three different samples.

The PLGA films, nHA/PLGA films, and their corresponding coatings on the Mg substrates were characterized using the SEM at an accelerating voltage of 5 kV with an original magnification of 100,000x. The CaP coated Mg was examined using the SEM at an accelerating voltage of 15 kV with an original magnification of 2,500x.The dispersion state of nHA in PLGA was determined through quantitative analysis of SEM images using ImageJ. The nHA particles dispersed in the PLGA matrix were first manually outlined and then converted into a binary mask using ImageJ. To quantify nHA dispersion in the PLGA matrix before and after spin coating, the Feret maximum diameter and the areal fraction of the nHA particles in the binary mask were measured and calculated using ImageJ.

3.2.7- Degradation Studies by Potentiodynamic Polarization Test

The degradation of the coated versus non-coated Mg samples were tested in revised simulated body fluid (rSBF), because rSBF has the same ionic concentration as human blood plasma and is commonly used for the testing of implant materials [122].

Potentiodynamic Polarization (PDP) tests are widely accepted for determining corrosion potential and corrosion rate of magnesium-based metallic materials [123] and were conducted in this study according to ASTM standard G 102-89 to predict the degradation rate of the samples. Potentiodynamic polarization curves were generated using a Potentiostat/galvanostat (model 273A; EG&G Princeton applied research). The nHA/PLGA coated Mg, PLGA coated Mg, and non-coated Mg samples were tested in triplicate in rSBF at 37°C. Each sample was clamped to the working electrode with half of the samples being immersed in rSBF and the other half above the rSBF solution. An Ag/AgCl reference electrode (part # CHI111, CHI Instruments) and a Pt counter electrode (part # CHI 115, CHI Instruments) were used and immersed in the same rSBF solution. The PDP test was performed at an electric potential ranged from +1 V to -3 V, with a 10 mV step size and a 0.5-second step time at a 100 mV/s scan rate. On the PDP plots, straight lines were drawn along the linear portion of the potentiodynamic polarization curves. From the intersection of these straight lines, the corrosion current (I_{corr}) and corrosion potential (E_{corr}) were extrapolated. The corrosion rate (CR) (in mm/year) of the samples was calculated using the following equation from ASTM standard G 102-89. The statistical significance of corrosion rate was determined by Kruskal-Wallis test with an α value of 0.05.

$$CR = \frac{I_{corr} \times K_1 \times EW}{\rho \times A} \qquad \text{Eq. 3.1}$$

where I_{CORR} is the corrosion current, K_1 is the constant for unit conversion, EW is the equivalent weight of Mg, ρ is the density of corroding species (Mg), and A is the area of

the sample submerged in rSBF. Specifically, K_1=3.27x10^{-3} (mm•g)/(μA•cm•year), EW=12.15, ρ=1.74 g/cm^3, A=1.2 cm^2.

3.2.8- Degradation Studies by Immersion Method

The degradation of nHA/PLGA coated Mg, PLGA-coated Mg control, CaP-coated Mg control, and non-coated Mg control were further investigated using immersion methods to complement the PDP test. The PLGA and nHA/PLGA films, their coatings on AZ31 and Ti substrates, and non-coated substrates were used as additional controls. All the samples were weighed, photographed, and disinfected under ultraviolet (UV) radiation before immersion. The samples were first placed into the wells of 12 well tissue culture plates in a laminar flow hood (Model no. NU-425-400, Nuaire), and 3 mL of rSBF was added to each well. The samples were incubated in rSBF under standard cell culture conditions (a sterile, 37°C, 5% CO_2/95% air, and humidified environment) until reaching the prescribed time points. The prescribed time points were 0 hours, 1 hour, 2 hours, 4 hours, 8 hours, 16 hours, and 24 hours to closely mimic the *in vivo* condition where circulation takes away degradation products regularly. After each time point, the rSBF was removed from the wells and the samples were dried in vacuum for at least 24 hours. The pH of the rSBF was measured using a pre-calibrated pH meter (Symphony SB70P, VWR). The dried samples were weighed and photographed. These samples were then placed into 3 mL of fresh rSBF and incubated for the next prescribed time point. This process was repeated for each prescribed time point. All the samples were handled in sterile conditions during the immersion study.

The rSBF collected at each time point was analyzed for Mg ion concentration ($[Mg^{2+}]$) and Ca ion concentration ($[Ca^{2+}]$) using inductively coupled plasma - atomic emission spectroscopy (ICP-AES; Optima 2000 DV, Perkin Elmer Instruments). A serial diluted $MgCl_2$ and $CaCl_2$ solutions were run in parallel to generate standard curves.

After 24 hours of immersion, the delaminated coatings were placed on a conductive copper tape for SEM imaging and EDX analysis. The PLGA coating was imaged at an accelerating voltage of 5 kV with an original magnification of 2500x. The nHA/PLGA coating was imaged at an accelerating voltage of 2 kV with an original of 2500x. EDX analysis was performed at an accelerating voltage of 10 kV with an original magnification of 2500x.

3.3- Results

3.3.1- Characterization of the nHA Particles

Figure 3.1 shows the SEM image, EDX spectrum and quantification of elemental composition, and XRD spectrum of nHA synthesized in this study. The nHA particles (Figure 3.1A) had an average Feret maximum diameter of 63±50 nm based on quantitative analysis of the binary masks of the SEM images (Figure 3.1B) using ImageJ. EDX analysis showed that the nHA particles had a Ca/P ratio of 1.67, same as the Ca/P ratio of natural bone (Figure 3.1C). XRD spectrum demonstrated that the synthesized particles had the desired HA phase (Figure 3.1D) and similar crystal structure as the HA extracted from bone [124].

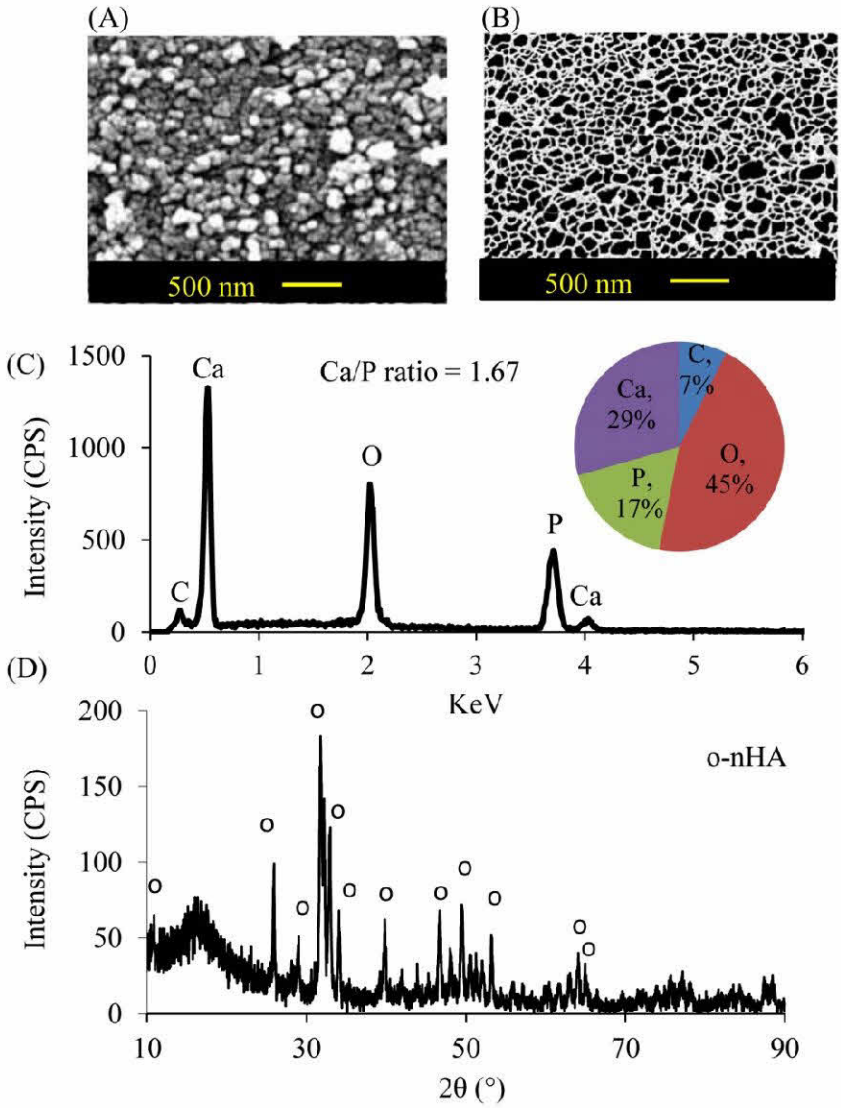

Figure 3.1: Characterization of nHA. (A) SEM image of the synthesized nHA particles. (B) Binary mask of the (A) SEM image of nHA particles. The Feret maximum diameter of the nHA particles was 63±50 nm based on the ImageJ analysis. (C) EDX spectrum of the nHA and quantification of its elemental composition. The nHA had the desirable Ca/P ratio of 1.67. Both SEM and EDX were conducted at a 10 kV accelerating voltage. SEM images were taken at a magnification of 100,000 x while EDX spectrum was taken at a magnification of 2500 x. (D) XRD spectrum of the nHA shows the peaks matching with the HA standard.

3.3.2- Characterization of the Coated and Non-coated Mg Substrates

Figure 3.3 shows the SEM images of the cross-sections of the PLGA and nHA/PLGA coatings on Mg substrates. The PLGA coating had a thickness of 53±8 μm (Figure 3.2A) and the nHA/PLGA coating had a thickness of 49±5 μm (Figure 3.2B), according to ImageJ analysis of the cross-section images. The thicknesses of the PLGA and nHA/PLGA coatings were intentionally controlled to be similar to each other during spin coating to ensure the comparability of their degradation results and eliminate the effects of the coating thickness factor on the degradation results.

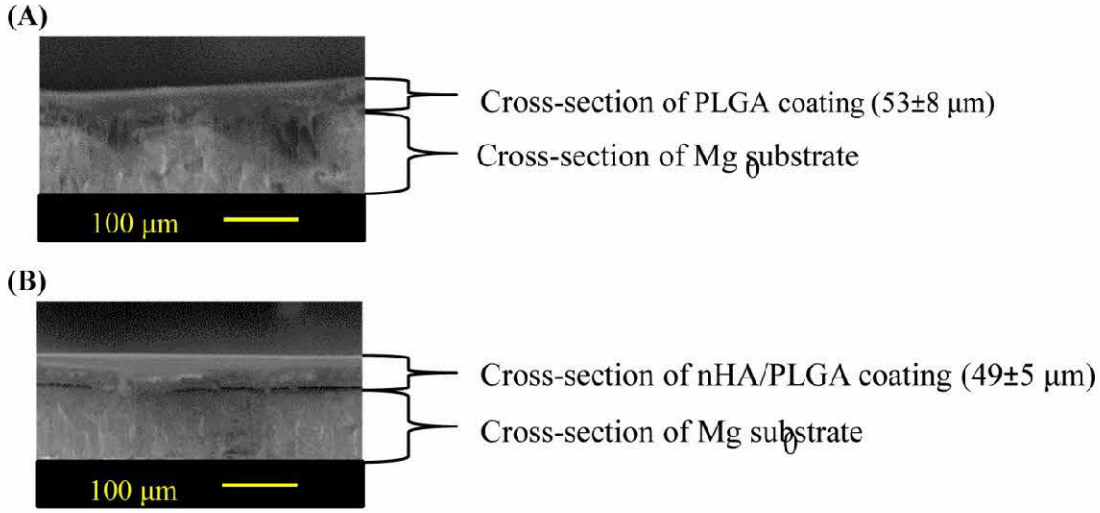

Figure 3.2: Coating cross-section images. (A) SEM image of the cross-section of PLGA coated Mg. The PLGA coating thickness was 53±8 μm. (B) SEM image of the cross-section of nHA/PLGA composite coated Mg. The coating thickness was 49±5 μm. The SEM images were taken at an original magnification of 250x with a 5 kV accelerating voltage.

Figure 3.3 shows the SEM images of the surfaces of the PLGA and nHA/PLGA films and their respective coatings on the Mg substrates in comparison with non-coated Mg and CaP coated Mg controls. The PLGA film was smooth without any significant

surface features (Figure 3.3A), while the nHA/PLGA film appeared rough due to the presence of nHA nanoparticles (Figure 3.3B). Figure 3.3C shows the binary mask of Figure 3.3B. Similarly, the PLGA coating on the Mg substrates was smooth (Figure 3.3D) and the nHA/PLGA coating appeared rough due to the presence of nHA nanoparticles (Figure 3.3E). Figure 3.3F shows the binary mask of Figure 3.3E. As expected, the non-coated Mg had a smooth surface (Figure 3.3G). The CaP coated Mg control had a rough surface with micron-scale CaP particulate features (Figure 3.3H).

The nHA particles in the nanocomposite film (Figure 3.3B) showed a Feret maximum diameter of 64±28 nm according to quantitative analysis of the ImageJ binary mask (Figure 3C). This diameter is very similar to the average Feret maximum diameter of nHA particles (i.e., 63±50 nm), which demonstrated the homogenous dispersion of nHA in the PLGA matrix. In comparison, the nHA particles in the nanocomposite coating (Figure 3E) showed a Feret maximum diameter of 269±130 nm according to quantitative analysis of the ImageJ binary mask (Figure 3F), which indicated some degree of agglomeration as compared with the nanocomposite film.

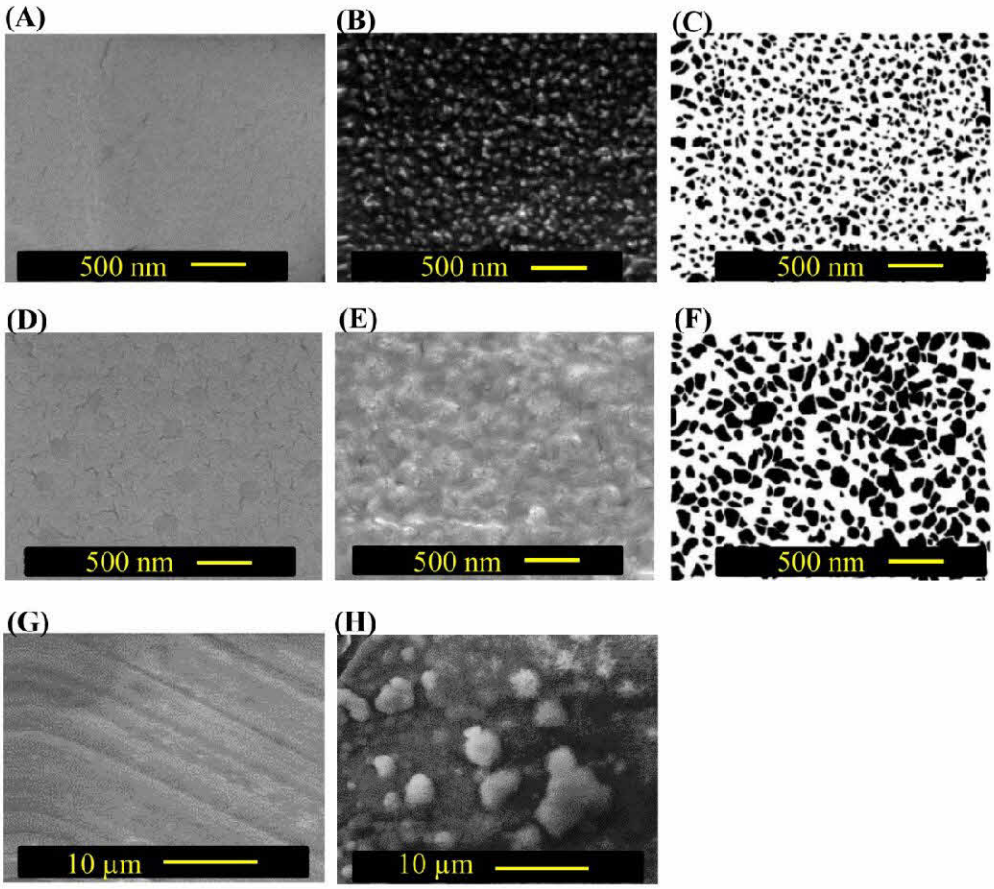

Figure 3.3: SEM images of the surfaces of the materials of interest before degradation studies. (A) The SEM of the PLGA film. (B) The SEM of the nHA/PLGA film. (C) The binary mask of the (B) SEM image of the nHA/PLGA film. (D) The SEM of the PLGA coated Mg. (E) The SEM of the nHA/PLGA coated Mg. (F) The binary mask of the (E) SEM image of the nHA/PLGA coated Mg. (G) The SEM of the non-coated Mg control. (H) The SEM of the CaP coated Mg control. SEM images of the PLGA and nHA/PLGA surfaces were taken at an original magnification of 100,000x with a 5 kV accelerating voltage. SEM images of the non-coated Mg and CaP coated Mg were taken at an original magnification of 2,500x with a 15 kV accelerating voltage.

3.3.3- Degradation Rate Determined by PDP Test

The PLGA and nHA/PLGA coatings significantly increased the corrosion potential (E_{corr}) and decreased the corrosion current (I_{corr}) of Mg substrates during PDP testing in rSBF at 37°C, as shown in Figure 3.4A. Therefore, the Mg corrosion rate (CR, mm/year) decreased, as shown in Figure 3.4B. The nHA/PLGA coating increased the average E_{corr} more than the PLGA coating, although both of them showed higher average E_{corr} than the non-coated Mg. The PLGA coatings reduced the I_{corr} one order of magnitude lower than non-coated Mg, and the nHA/PLGA coating reduced the I_{corr} one order of magnitude lower than the PLGA coating. Due to the reduction of I_{corr}, the calculated corrosion rates for the PLGA coated and nHA/PLGA coated samples were significantly decreased. Specifically, the corrosion rates were in the following order from the slowest to the fastest degrading: nHA/PLGA coated Mg < PLGA coated Mg < non-coated Mg. The effects of PLGA and nHA/PLGA coatings on the degradation rates of Mg were statistically significant, as demonstrated by the calculated p value of 0.00367 using the Kruskal-Wallis test.

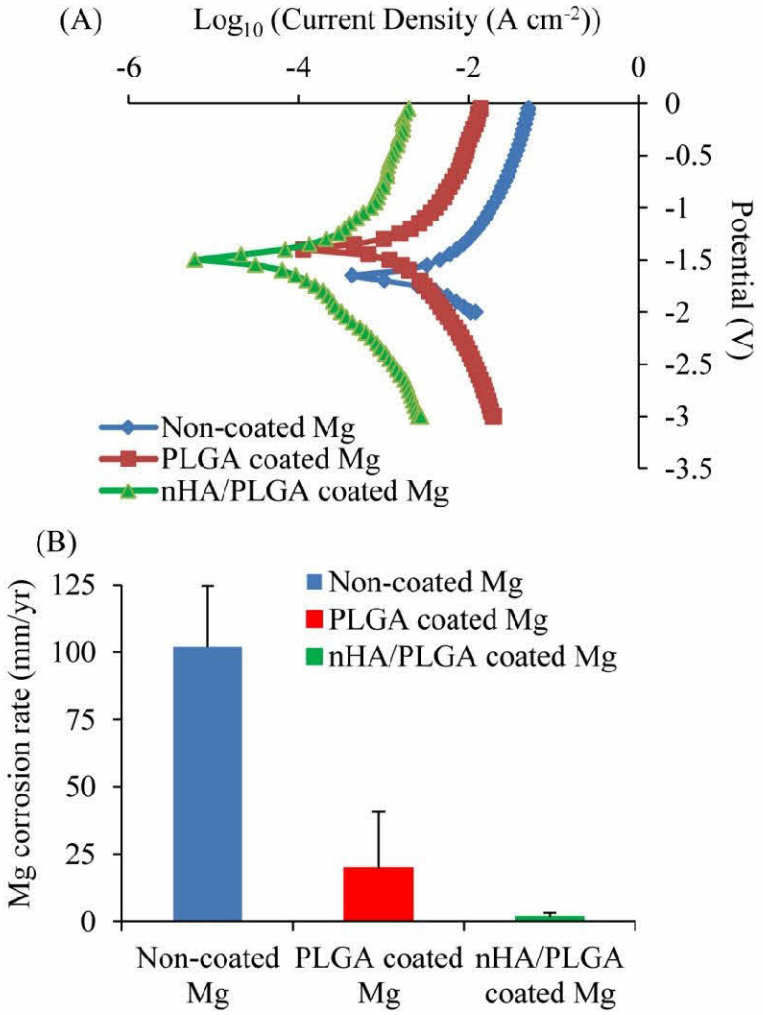

Figure 3.4: PDP analysis of coated and non-coated Mg. (A) PDP plots of non-coated Mg, PLGA coated Mg, and nHA/PLGA composite coated Mg measured in rSBF at 37°C. (B) The predicted Mg corrosion rates were calculated based on ASTM standard G 102-89

3.3.4- Degradation Determined by Immersion Method

3.3.4.1- Changes to Surface Morphology during Degradation

Immersion of the samples in the rSBF solution altered their surfaces, as shown in Figure 3.5. The non-coated Mg and AZ31 substrates initially had shiny silver colored and smooth metallic surfaces. After 1 hour incubation in rSBF, their shiny smooth surfaces turned into beige colored rough surfaces due to oxidation of Mg and deposition of degradation products. The non-coated Ti surfaces did not change much after incubation in rSBF, although they were slightly less shiny after 24 hours incubation. The PLGA and nHA/PLGA coatings on the Mg and AZ31 substrates initially were transparent, and their appearances changed dramatically after immersion in rSBF. Small pores started to form in both the PLGA and the nHA/PLGA coatings after 1 hour incubation, and then grew larger with formation of more pores as the incubation time increased. With the progression of the degradation, the adjacent pores started to merge with one another to form larger cavities, and the PLGA and nHA/PLGA coatings on both the Mg and AZ31 substrates became opaque white. Eventually, the propagation of the pores caused the coatings to delaminate from the Mg and AZ31 substrates. The nHA/PLGA coatings delaminated slightly earlier than the PLGA coatings from the Mg substrates, after 4 hours and 8 hours incubation, respectively. Similarly, from the AZ31 substrates, the nHA/PLGA coatings delaminated after 4 hours incubation while the PLGA coatings delaminated after 8 hours incubation. The immersion study was ended after 24 hours incubation since the nHA/PLGA coatings and PLGA coatings delaminated from Mg-based substrates. The CaP coated Mg control showed similar color throughout the

immersion study, and visible degradation products started to accumulate on the surface after 4 hours incubation. The PLGA and nHA/PLGA coatings on the Ti control substrates did not show any significant change throughout the study. The PLGA coatings on the Ti substrates remained transparent, but the nHA/PLGA coatings became slightly opaque after 24 hours incubation.

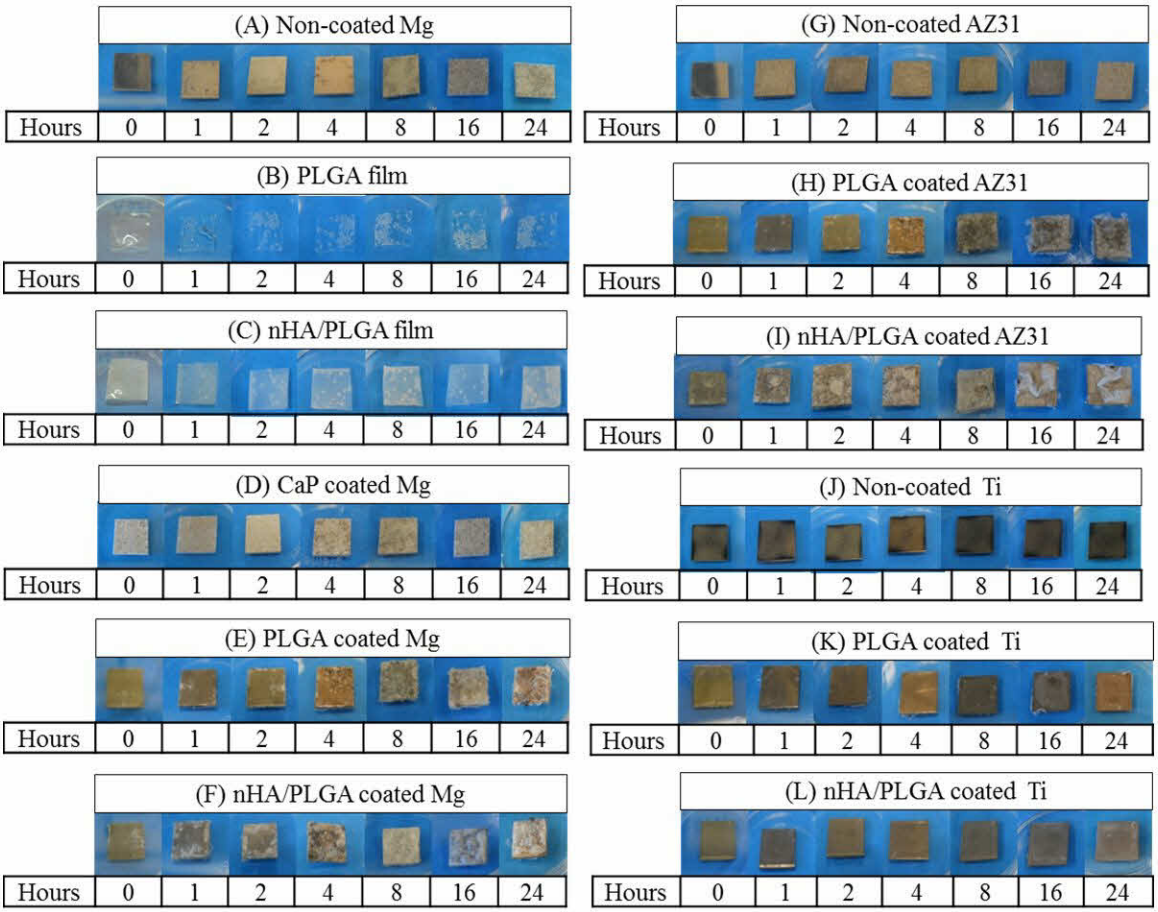

Figure 3.5: Photographs of the samples after immersion in rSBF. Samples were incubated under standard cell culture conditions for the prescribed time points. (A) Non-coated Mg. (B) PLGA film. (C) nHA/PLGA film. (D) CaP coated Mg. (E) PLGA coated Mg. (F) nHA/PLGA coated Mg. (G) Non-coated AZ31. (H) PLGA coated AZ31. (I) nHA/PLGA coated AZ31. (J) Non-coated Ti. (K) PLGA coated Ti. (L) nHA/PLGA coated Ti.

3.3.4.2- Changes to the Sample Mass during Degradation

Immersion of the coated and non-coated substrates in the rSBF solution had profound effects on the sample mass change due to the simultaneously occurring degradation, precipitation and deposition processes (Figure 3.6A-D). As shown in Figure 3.6A, similar mass changes were observed for all the samples initially, but after 24 hours incubation, the PLGA and nHA/PLGA coated Mg samples showed more mass gain than the non-coated Mg and CaP coated Mg samples. Figure 3.6B shows the mass change of the coated and non-coated AZ31 samples. The nHA/PLGA coated AZ31 samples showed mass gain after 16 hours incubation. After 24 hours incubation, however, the mass dropped to approximately equivalent to the initial sample mass. Figure 3.6C shows the mass change of the coated and non-coated Ti samples. The PLGA coated, nHA/PLGA coated, and non-coated Ti substrates had negligible mass change during their immersion in rSBF. This was expected since Ti is inert. Moreover, the mass of the Ti substrates was much greater than the mass of the PLGA and nHA/PLGA coatings, which made the relatively small mass changes from the coating degradation or CaP deposition less detectable. Figure 3.6D shows the mass change of the PLGA and nHA/PLGA films. The nHA/PLGA film gained more mass after 8 hours than the PLGA film.

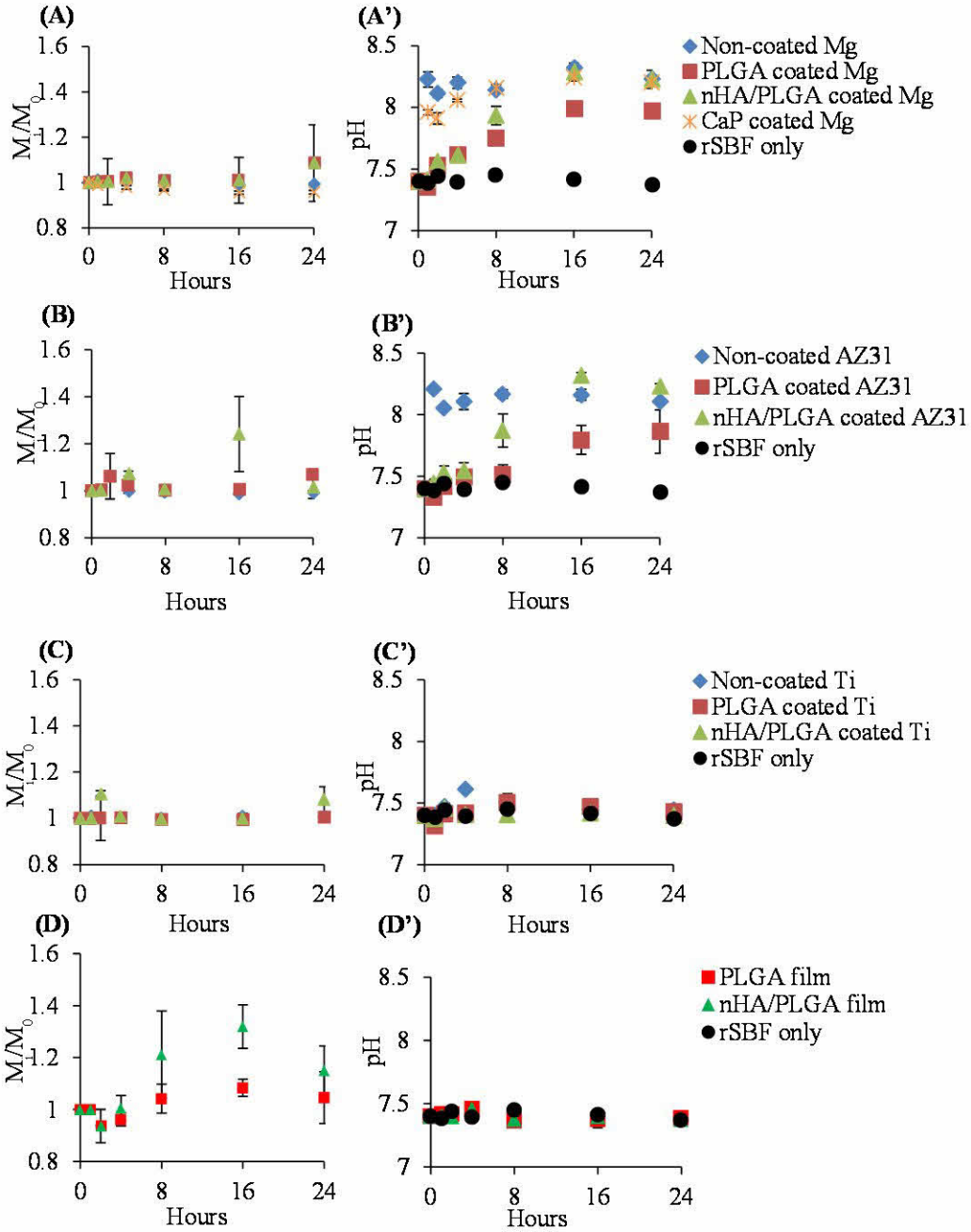

Figure 3.6: Sample mass and pH change in rSBF. (A-D) Mass change of the coated versus non-coated Mg, AZ31, and Ti samples and the controls and (A'-D') the respective pH change of rSBF during 24-hours incubation. M_i/M_0 is the sample mass at the respective time point divided by its initial mass. (A and A'): Mg as substrate. (B and B') AZ31 as substrate. (C and C') Ti as substrate. (D and D') films only (no substrate).

3.3.4.3- Changes to the pH of rSBF during Degradation

Immersion of the coated and non-coated Mg and AZ31 substrates in the rSBF resulted in pH increase, while the films and coated and non-coated Ti substrates did not show any significant pH changes (Figure 3.6 A'-D'). The effects of Mg degradation on the pH changes of the rSBF immersion solution were more pronounced than the mass changes of the samples. Figure 3.6A' shows the pH changes of rSBF when cultured with the coated and non-coated Mg samples in comparison with rSBF control. At the first 8 hours incubation, the pH of rSBF cultured with the non-coated and CaP coated Mg samples increased more significantly than the PLGA coated and nHA/PLGA coated Mg samples, which indicated that the PLGA and nHA/PLGA coatings alleviated alkalization of the rSBF. After the 8 hour time point, the PLGA coating decreased rSBF alkalization from Mg degradation more effectively than the nHA/PLGA.

As compared to Figure 3.6A', Figure 3.6B' shows the similar trend for the PLGA coated and nHA/PLGA coated AZ31 samples versus non-coated AZ31 samples. Briefly, before the 8 hour time point, the PLGA and nHA/PLGA coatings relieved alkalinity of rSBF to some degree as compared with much higher pH for the non-coated AZ31samples. However, the pH of rSBF containing the PLGA and nHA/PLGA coated AZ31 samples increased after the 8 hour time point, and reached a similar level as the non-coated AZ31 samples at 24 hour time point.

In contrast to the Mg-based substrates, the coated and non-coated Ti control samples did not cause any significant pH changes in rSBF, as shown in Figures 3.6C'.

Figure 3.6D' shows that the PLGA and nHA/PLGA films did not cause any detectable pH change in rSBF either.

3.3.4.4- Changes to Mg and Ca Ion Concentrations in rSBF during Degradation

Immersion of PLGA coated Mg, nHA/PLGA coated Mg, CaP coated Mg, and non-coated Mg samples in rSBF altered the Mg and Ca ion concentration of rSBF, as shown in Figure 3.7. Figure 3.7A shows that Mg ion concentration in rSBF increased for all the samples, including non-coated Mg, PLGA coated Mg, nHA/PLGA coated Mg, and CaP coated Mg; as compared to the constant Mg ion concentration of the rSBF control. Before the 8 hour time point, the non-coated Mg samples released more Mg ions than the PLGA coated and nHA/PLGA coated Mg samples. This indicated that the PLGA and nHA/PLGA composite coatings protected the Mg substrates from degradation. After the 8 hour time point, the Mg ion concentrations of rSBF containing the PLGA and nHA/PLGA coated Mg samples increased significantly. Specifically, at the 24 hour time point the nHA/PLGA coated Mg samples released a similar amount of Mg ions as the non-coated Mg control. Interestingly, the PLGA coated Mg samples released less Mg ions than the non-coated Mg control throughout the 24 hour incubation period. The CaP coated Mg released less Mg ions than the non-coated Mg after 24 hours immersion, but released more Mg ions than the PLGA and nHA/PLGA coated Mg during the initial 4 hours incubation.

Figure 3.7B shows that the PLGA coated Mg, nHA/PLGA coated Mg, and non-coated Mg samples all reduced the concentrations of Ca ions in the rSBF after 8 hours

incubation as compared with the rSBF control. The reduction of Ca ion concentration in rSBF indicated the deposition of Ca containing salts onto the samples during incubation. Specifically, after 8 hours incubation, the nHA/PLGA coated Mg samples showed more reduction in Ca ion concentration than the PLGA coated and non-coated Mg samples, indicating more Ca containing salts deposited on the nHA/PLGA coated surfaces. The Ca ion concentration of the rSBF containing the CaP coated Mg samples fluctuated during 24 hours immersion and became the same as the rSBF control at 24 hour time point.

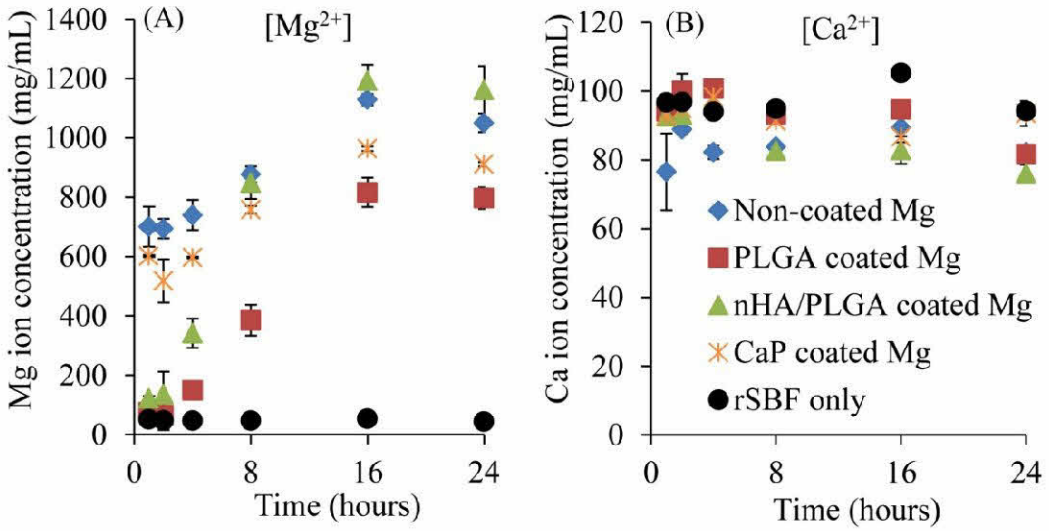

Figure 3.7: Ion concentration change in rSBF after sample immersion. The change of (A) Mg ion concentration and (B) calcium (Ca) ion concentration in rSBF after the non-coated Mg, PLGA coated Mg, and nHA/PLGA coated Mg samples were incubated in rSBF for the prescribed time points.

3.3.4.5- Changes to Surface Microstructure and Composition during Degradation

The PLGA and nHA/PLGA coatings on Mg substrates after 24 hours degradation in rSBF were examined using SEM and EDX, as shown in Figure 3.8. Figure 3.8A shows the presence of micropores on the PLGA coating. These micropores allowed water to

penetrate the coating and reach the Mg substrate. According to the EDX results shown in Figure 3.8A', no CaP deposition was observed on the PLGA coatings. The surface morphology of nHA/PLGA coating changed significantly due to the CaP deposition and Mg degradation, as shown in Figures 3.8B and 3.8C. According to the EDX results shown in Figures 3.8B' and 3.8C', a significant amount of CaP deposited onto the nHA/PLGA coatings. Apatite rosettes with increased surface elemental percentage of Mg were observed on the nHA/PLGA coating (Figure 3.8C), indicating possible Mg substitution of Ca in the CaP crystal structure.

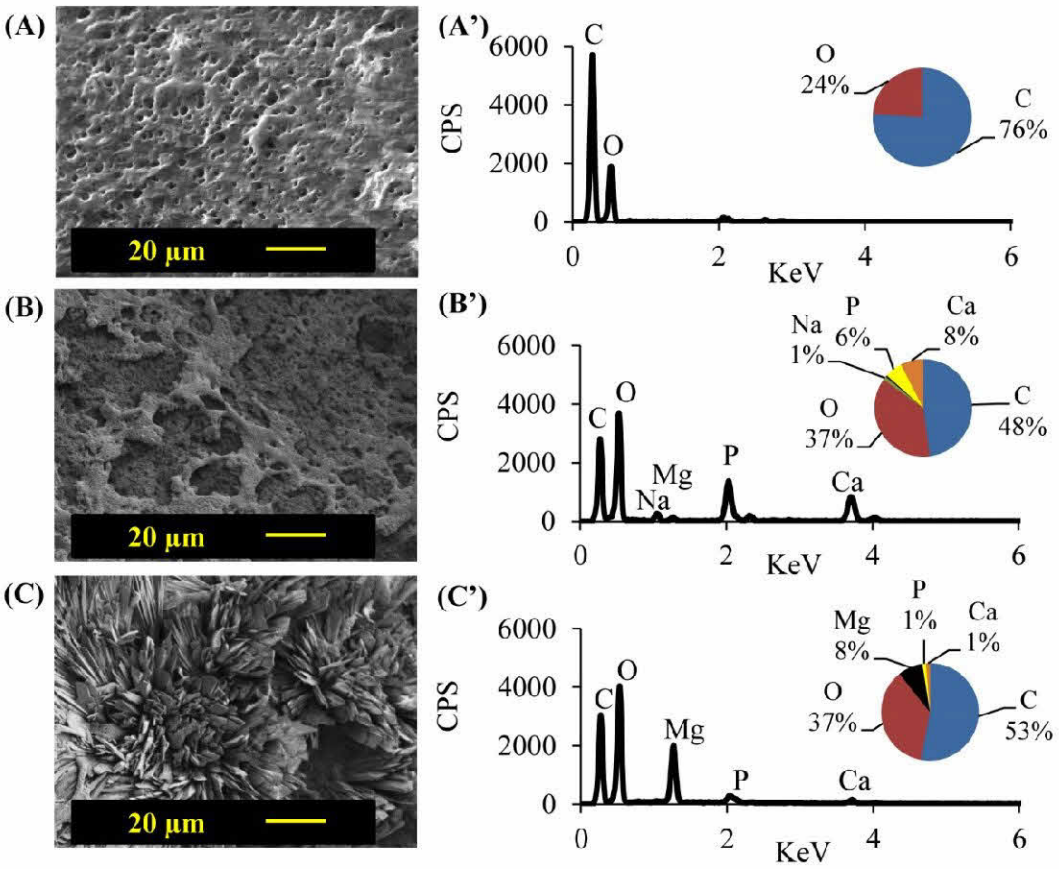

Figure 3.8: SEM images and respective EDX analyses of the coatings delaminated from Mg substrates after 24-hours degradation in rSBF. (A-C): SEM images and (A'-C'): respective EDX results. (A and A') PLGA coating, (B and B') nHA/PLGA coating, and (C and C') crystal deposited on the nHA/PLGA coating. Scale bars: 20 µm. Original Magnification: 2500 x. The SEM images of the PLGA and nHA/PLGA coatings were taken at an accelerating voltage of 5 kV and 2 kV respectively. EDX spectrum was obtained at a magnification of 2500 x with a 10 kV accelerating voltage.

3.3.4.6- Gas Evolution and Delamination of Coatings

Hydrogen gas (H_2) is another degradation product of Mg in addition to Mg ions and hydroxide ions. Figure 3.9 shows that visible gas bubbles formed in the rSBF containing the coated and non-coated Mg and AZ31 samples, but not in the rSBF

containing the coated and non-coated Ti samples or the PLGA and nHA/PLGA films. This indicated that the gas bubbles were from the H_2 produced by the reaction between Mg and water rather than hydrolysis of the coatings. The rSBF containing the non-coated Mg, the CaP coated Mg, and the non-coated AZ31 samples showed more bubbles than that of the PLGA coated and nHA/PLGA coated Mg and AZ31 samples. Moreover, the H_2 bubbles distributed across the culture wells for the non-coated and CaP coated Mg samples and the non-coated AZ31 samples. In contrast, the gas bubbles were only observed around the edges of the PLGA and nHA/PLGA coated Mg and AZ31 samples. As Ti is inert, there were no bubbles observed around the PLGA and nHA/PLGA coated Ti and non-coated Ti, confirming that the gas bubbles were H_2 gas released from Mg degradation rather than the coating degradation.

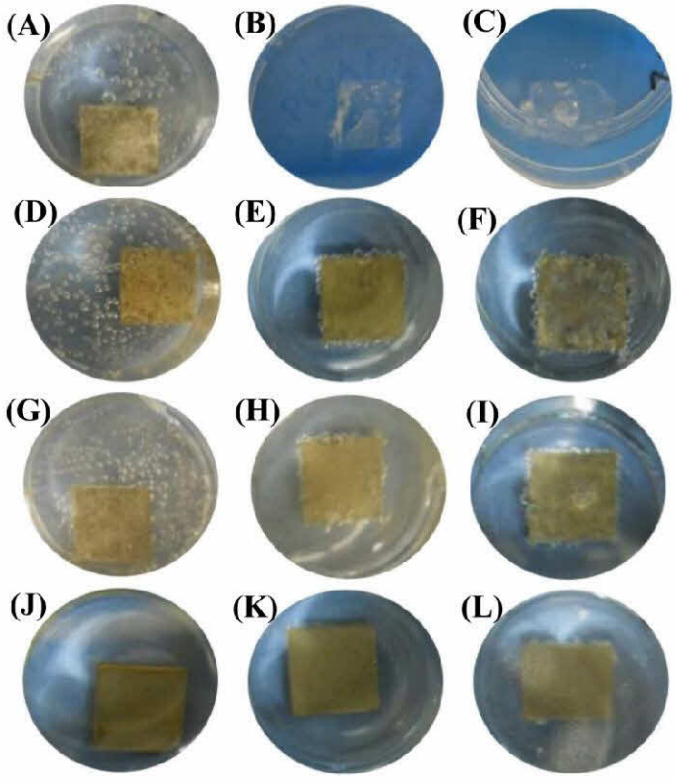

Figure 3.9: Hydrogen gas evolution after 2 hours of the sample degradation in rSBF. (A) Non-coated Mg. (B) PLGA film. (C) nHA/PLGA film. (D) CaP coated Mg. (E) PLGA coated Mg. (F) nHA/PLGA coated Mg. (G) Non-coated AZ31. (H) PLGA coated AZ31. (I) nHA/PLGA coated AZ31. (J) Non-coated Ti. (K) PLGA coated Ti. (L) nHA/PLGA coated Ti.

3.4- Discussion

3.4.1- Composite Coatings had Nanoscale Features

Even though the size of agglomerates in the nHA/PLGA coating was larger than that of the nHA crystals in deproteinated bone (25-50 nm) [125] and the synthesized nHA particles (63±50 nm), the coating still maintained surface features at the nano-scale (100 nm to 400 nm) that have been reported to promote osteoblast functions [126]. The agglomerates in the nanocomposite coating might have been caused by the time lapse between the high-power sonication and the spin coating process, which will be addressed in future studies by optimizing the coating deposition process.

3.4.2- The nHA was Well Dispersed in the nHA/PLGA Films and Coatings

The dispersion states of nHA particles in the nanocomposite film or coating play an important role in the mechanical and biological properties of nanocomposites. Specifically, it has been reported that homogenously dispersed nanoparticles in PLGA matrices enhanced the mechanical properties of the nanocomposites and improved the osteoblast adhesion and long-term functions *in vitro,* as compared with the agglomerated nanoparticles in PLGA composites [105, 127]. The procedures for the preparation of the nanocomposite suspension and spin coating process had significant effects on the dispersion of nHA in the final composite coatings. In this study, the nHA/PLGA composite suspension contained 30 wt.% nHA and 70 wt.% PLGA which corresponded to a 15.39 vol.% nHA and 84.61 vol.% PLGA theoretically, based on calculations using equation 3.2.

$$V_{HA} = \frac{\frac{M_{HA}}{\rho_{HA}}}{\frac{M_{HA}}{\rho_{HA}} + \frac{M_{PLGA}}{\rho_{PLGA}}} \times 100\% \qquad \text{Eq. 3.2}$$

V_{HA} is the volume percent of nHA in the nHA/PLGA composites. M_{HA} is the mass of nHA in the composites; ρ_{HA} is the theoretical density of nHA; M_{PLGA} is the mass of PLGA in the composites; ρ_{PLGA} is the theoretical density of PLGA.

The nHA particles occupied 27.90% of the area on the surface of the nHA/PLGA composite film and 45.30% of the area on the surface of the nHA/PLGA composite coating on Mg, according to the quantitative image analysis of Figures 3.3C and 3.3F. The area percentages of nHA particles on the surfaces of the composite film and the coating were both greater than the theoretical volume percentage of nHA particles in the PLGA matrix. This indicated that the nHA particles retained their nanoscale-size and remained on the surface rather than settling down to the bottom even though they may have some degree of agglomeration with each other. According to the Stoke's law, nanoparticles would be able to remain dispersed in the polymer matrix as long as the size of agglomerates was small enough to ensure a slower sedimentation rate than the solvent evaporation rate. It is also important to point out that residual PLGA might have adhered to the glassware used for preparing the nanocomposite suspension, which resulted in the decrease of the PLGA volume percent and increase of nHA volume percent in the composite films and coatings. This will be addressed in the future studies by optimizing the procedures for composite and coating preparation, e.g., using PTFE vessels instead of glassware to reduce the loss of PLGA. Moreover, initiating the spin coating process

immediately after high power sonication of the composite suspensions will further improve the dispersion of nHA in the nanocomposite coatings.

3.4.3- Delamination Limited the Duration of the Coatings Effectiveness

The appearance of the nHA and PLGA coatings on Mg deteriorated at every time point, after 8 hours immersion the coatings had numerous gas cavities and localized detachment from their substrates (Figure 3.5). This delamination prevented the coatings from effectively controlling substrate degradation at later immersion times. The delamination also liberated trapped Mg degradation products from previous time points on the substrate surfaces, which further increased the local pH and $[Mg^{2+}]$.

The PLGA and nHA/PLGA coatings on the Mg and AZ31 substrates initially prevented large increases to the local pH and $[Mg^{2+}]$. After 8 hours of immersion, the pH and $[Mg^{2+}]$ rose significantly, and the increased release of both ions mirrored each other (Figure 3.6, 3.7). The nHA/PLGA coated Mg eventually had pH and $[Mg^{2+}]$ that were nearly equal to non-coated Mg, while the PLGA coated Mg had slightly lower values in comparison to non-coated Mg. This demonstrated that PLGA and nHA/PLGA coatings can effectively control Mg degradation during the early stages of degradation, but improved engineering of these coatings is needed to extend the period of time that they can effectively reduce Mg degradation rates.

3.4.4- Dispersed nHA Improved CaP Deposition onto Coating Surfaces during Immersion

The PLGA coated Mg, nHA/PLGA coated Mg, and non-coated Mg samples all reduced the concentrations of [Ca^{2+}] in the rSBF after 8 hours incubation as compared with the rSBF control (Figure 3.7). The reduction of [Ca^{2+}] in rSBF indicated the deposition of Ca containing salts onto the samples during incubation. Specifically, after 8 hours incubation, the nHA/PLGA coated Mg samples showed more reduction in [Ca^{2+}] than the PLGA coated and non-coated Mg samples, indicating more Ca containing salts deposited on the nHA/PLGA coated surfaces.

The PLGA coatings on Mg substrates developed micropores after 24 hours of immersion (Figure 3.8A), which allowed water to penetrate the coating and reach the Mg substrate. No CaP deposition was observed on the PLGA coatings for Mg substrates (Figure 3.8A'). Contrastingly, the surface morphology of nHA/PLGA coating changed significantly due to the CaP deposition and Mg degradation (Figure 3.8B). A layer of deposits was clearly visible on the surface, and the micropores observed on the PLGA coating were not present on the nHA/PLGA coating. A significant amount of CaP was deposited onto the nHA/PLGA coatings (Figure 3.8B'). The nHA in the PLGA matrix served as the nucleation sites to attract the CaP mineral deposition. The deposition of CaP was also confirmed by the reduction of [Ca^{2+}] in the rSBF (Figure 8B).

Apatite rosettes with increased surface elemental percentage of Mg were observed on the nHA/PLGA coating (Figure 3.9C, C'), indicating possible Mg substitution of Ca in the CaP crystal structure. Mg substitution of Ca in the HA crystals has been known for

enhancing osteoblast adhesion and long-term functions on the HA [128], and improving osseointegration of the implants coated with HA [129]. Additionally, the incorporation of nHA in the PLGA matrix increased water absorption [94], which in turn may have resulted in more rSBF constituents locally available for deposition onto the surface.

3.4.5- Gas Evolution Promoted Delamination of Coatings

Hydrogen gas (H_2) is another degradation product of Mg in addition to [Mg^{2+}] and OH^-. Figure 3.9 shows that visible gas bubbles formed in the rSBF containing the coated and non-coated Mg and AZ31 samples, but not in the rSBF containing the coated and non-coated Ti samples or the PLGA and nHA/PLGA films. This indicated that the gas bubbles were from the H_2 produced by the reaction between Mg and water rather than hydrolysis of the coatings. The rSBF containing the non-coated Mg, the CaP coated Mg, and the non-coated AZ31 samples showed more bubbles than that of the PLGA coated and nHA/PLGA coated Mg and AZ31 samples. Moreover, the H_2 bubbles were distributed across the culture wells for the non-coated and CaP coated Mg samples and the non-coated AZ31 samples. In contrast, the gas bubbles were only observed around the edges of the PLGA and nHA/PLGA coated Mg and AZ31 samples. Less gas bubbles around the PLGA coated and nHA/PLGA coated Mg and AZ31 samples indicated that these coatings did protect the substrates from rapid degradation initially.

Although the degradation of PLGA releases carbon dioxide gas (CO_2), the gas bubbles observed in Figure 3.9 is unlikely to be CO_2. PLGA has to first degrade into lactic and glycolic acids (intermediate degradation products) in order to release CO_2 and water as the final degradation products. It takes several weeks for a PLGA scaffold to

degrade to a level where the dissolved lactic acid can be detected [130]. Therefore, the gas bubbles released during the first two hours immersion were not CO_2 from PLGA degradation. In addition, there were no bubbles observed around the PLGA and nHA/PLGA coated Ti and non-coated Ti, confirming that the gas bubbles were H_2 gas released from Mg degradation rather than the coating degradation.

The results indicated that Mg degradation and associated H_2 gas release initiated the coating delamination process. Figure 3.10 illustrates the speculated mechanisms for the coating delamination from Mg-based substrates. Before the PLGA coated Mg or AZ31 samples were immersed into the rSBF, the PLGA adhered onto the Mg or AZ31 substrates uniformly. As soon as the samples were immersed into the rSBF solution, PLGA started to absorb water, which resulted in water diffusion into coating-substrate interface and thus exposed Mg or AZ31 to water. Immediately, Mg started to react with water and release H_2 gas. As Mg degradation continued, more H_2 gas molecules evolved and started to cluster to minimize their free energy, resulting in pore formation and gas bubbles observed in Figures 3.8 and 3.9. Accumulation of gas bubbles led to delamination of the coatings from Mg-based substrates. In contrast, the PLGA and nHA/PLGA coatings did not delaminate from Ti substrates since Ti is inert and is considered non-degradable in rSBF. Therefore, water absorption by the PLGA and H_2 gas evolution from the Mg degradation both contributed to the coating delamination.

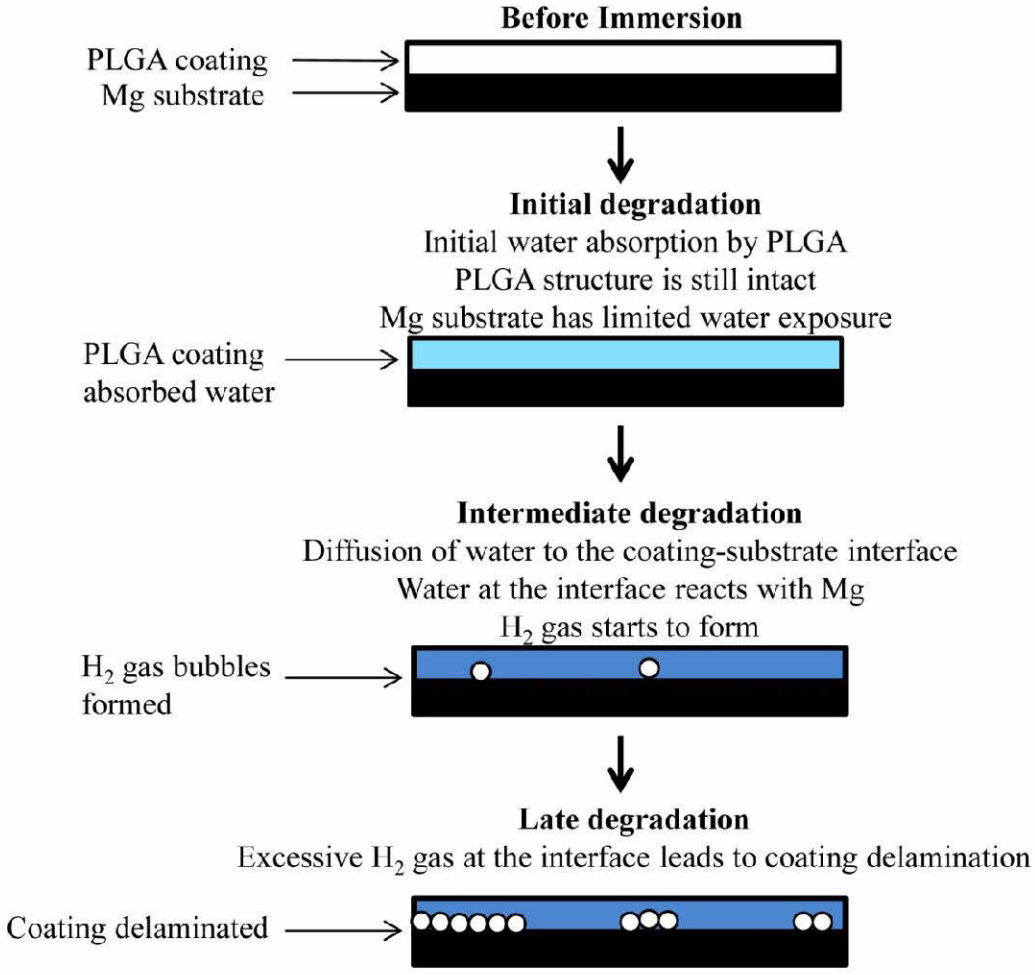

Figure 3.10: Illustration of the speculated mechanism for coating delamination from Mg-based substrates.

It is important to point out that the nHA/PLGA coated Mg showed an increase in corrosion potential as compared with the PLGA coated and non-coated Mg and should slow down Mg degradation more effectively if the coating does not delaminate. The nHA/PLGA coatings will also improve osteoconductivity compared to the PLGA coatings, which is critical for bone implant applications. Therefore, the coating properties

(e.g. hydrophobicity) must be engineered to reduce water uptake and permeability during immersion in the rSBF, which will alleviate the challenge of delamination.

3.5- Conclusions of Chapter 3

The nHA/PLGA nanocomposite coatings are promising for Mg alloys because they possess complementary mechanical, biological, and degradation properties. The PLGA and nHA/PLGA coatings significantly reduced the degradation rates of Mg and AZ31 substrates. Moreover, increased CaP deposition on the nHA/PLGA coated Mg substrates in rSBF could potentially improve the bioactivity of the surface for bone tissue integration. However, delamination of the PLGA and nHA/PLGA coatings from their substrates remains a challenge. This delamination can be prevented by reducing the permeability of the coatings so that less water reaches the Mg substrates, which will in turn reduce Mg surface instability and H_2 evolution.

Chapter 4- Optimization of Nanocomposite Coatings for Improved Interfacial Properties of Mg Substrates

4.1- Specific Challenges and Aims

The previous section demonstrated that nHA/PLGA coatings significantly reduced Mg degradation and alkalization of the local environment, but also discovered that delamination limited the duration over which the coatings protected their substrates from degradation [25]. This section investigated different polymer components, post-deposition processing routes, and substrate surface types to discover and address the causes of the rapid coating delamination. PLGA, PLLA, and PCL were chosen as the polymer coating components because of their extensive history as biomaterials, ease of use, and diverse properties. The different outcomes of the coating types shed light on the root causes of delamination and provided guidelines for the future design of coatings for Mg.

The specific aims of this section were:

1. Optimize the nanocomposite coatings to maximize the synergy between the three components (*i.e.* nHA, polymer component, Mg substrate).
    a. Screen the different combinations of coating parameters for the lowest corrosion rates using potentiodynamic polarization tests.
    b. Characterize the slowest degrading sample types from Objective 1a using immersion degradation studies.
2. Characterize bone cell adhesion to the slowest degrading sample type from Objective 1.

4.2- Materials and Methods

4.2.1- Preparation of Magnesium Substrates

Mg-based bars (97% Mg, 3% Al, 1 mm thick; Miniscience, Cat# MGFLAT) were ground with 600 grit silicon carbide paper (SiC; Ted Pella) while using ethanol (EtOH; Koptec) as a lubricant. The grinded Mg bars were then cut into 10 x 10 mm squares using a notcher (no. 100, Whitney Metal Tool Co). The Mg substrates were degreased in acetone (Sigma Aldrich) in an ultrasonic bath (VWR Symphony) for 30 minutes, and then cleaned in ethanol in the same ultrasonic bath for another 30 minutes. These Mg substrates had a metallic surface and were designated as M_Mg.

A separate group of M_Mg substrates had their surface modified using an alkaline heat treatment procedure to create a surface rich in $Mg(OH)_2$ [123]. Nucleating agents like $Mg(OH)_2$ could increase the crystallinity of polymers [131-134], which reduces the permeability of the polymer component of the nanocomposite coatings. The alkaline heat treatment was performed by immersing the M_Mg substrates in 1 M NaOH (Strem Chemicals) at 80 °C for 2 hours. After immersion, the substrates were gently rinsed with deionized (DI) water (Millipore Milli-Q® Biocel System) for three times and dried in air at room temperature. These alkaline-heat-treated substrates were named as A_Mg.

Before the coating deposition, the M_Mg or A_Mg substrates were cold mounted into epoxy resin (MG Chemicals, Cat # 832HT) with a diameter of 18 mm and a thickness of 2 mm. Only a single face of 10 x 10 mm of the Mg substrates was exposed for coating. Prior to mounting, a copper wire was secured underneath each Mg substrate using a copper tape for PDP measurements. The copper wire was encased in epoxy until

it exited the epoxy disk at one side, which insulated the copper wire from electrolyte when the exposed surface of the Mg substrate was completely immersed in rSBF.

4.2.2- Preparation of Nanocomposite Coatings on the Mg Substrates

The nHA was prepared using a wet chemistry precipitation method followed by hydrothermal treatment, as described previously [25]. The nHA was added to (85:15) PLGA (200 kDa, Cat# AP52), PLLA (230 kDa, Cat# AP65), or PCL (200 kDa, Cat# AP09) at a ratio of 30 wt.% nHA to 70 wt.% polymer. All polymers were procured from Polyscitech. The nHA/polymer mixtures were then suspended in a 10 wt./vol. % concentration in chloroform (Sigma Aldrich), and mixed in an ultrasonic bath (VWR Symphony) at 40 °C for 1 hour. The suspensions were dried in air for 1 hour on polytetrafluoroethylene (PTFE) dishes, and then re-suspended in chloroform again in the same ultrasonic bath at 40 °C for 2 hours, to reduce the settling of the nHA particles. To further improve the dispersion of nHA nanoparticles, the nanocomposites were sonicated at high power (9 W, 20 kHz; Misonix Sonicator S-4000) for 10 min.

The nHA/polymer suspensions were deposited onto the Mg substrates using a spin coater (Smart Coater; Best Tools, LLC). The spin coating speed was adjusted such that all the coatings had a similar thickness in the range of 30-40 μm. The other spin coating parameters were kept as constant. That is, the spin coating duration was always 60 seconds, and the spin-coating speed always increased by 1000 revolutions per minute for each second of acceleration until reaching the desired speed. Generally, the higher viscosity nHA/PLLA suspension required a higher spin coating speed to achieve the desired coating thickness, the lower viscosity nHA/PCL suspension required a lower spin

coating speed, and the nHA/PLGA suspension with an intermediate viscosity had an intermediate spin coating speed. For the same polymer component, the A_Mg substrates required a higher spin coating speed than the M_Mg substrates. The details of the spin coating parameters and coating thickness measurements are summarized in Table 4.1.

Table 4.1: Spin-coating speed and coating thickness for three nanocomposites with different polymer components on the Mg substrates with metallic surface (M_Mg) or alkaline heat treated surface (A_Mg). The thicknesses of nanocomposite coatings on the Mg substrates were quantified based on optical images of sample cross sections using ImageJ.

Spin-coating Parameters and Coating Thickness			
Substrate Surface	**Polymer Component in the Nanocomposite Coatings**	**Spin Speed (RPM)**	**Average Coating Thickness (μm)**
M_Mg	PLGA	400	34±1
A_Mg	PLGA	700	39±4
M_Mg	PLLA	700	34±2
A_Mg	PLLA	800	39±4
M_Mg	PCL	375	41±1
A_Mg	PCL	600	33±1

A digital micrometer (Marathon; Marathon Watch Company LTD) was used to measure the sample thickness before and after spin coating. The difference between the two measurements was the coating thickness. These coating thickness measurements were confirmed using optical images of the sample cross-sections. ImageJ was used to measure the thickness of the coating cross-sections in the optical images. To obtain the cross-section images, the Mg substrates were cut in half using a notcher and then mounted in epoxy side-by-side in their original orientation for spin coating. After spin coating, a razor was used to cut the coating in-between the two halves of the substrates,

and one of those halves was removed from the the epoxy mount so that its cross-sections could be imaged using an optical microscope (SE305R-P; AmScope) at an original magnification of 30x.

The coatings deposited on the Mg substrates were subjected to one of four different post-deposition processing routes: (1) no post-deposition processing, (2) melting the coating for 5 minutes, (3) annealing the coating for 30 minutes, and (4) melting the coating for 5 minutes followed by annealing the coating for 30 minutes. The nHA/PLGA and nHA/PLLA coatings were melted by heating in an oven (HeraTherm; Thermo Scientific) at 200°C for 5 minutes, and/or annealed by heating at 115°C for 30 minutes. A melting temperature of 200 °C was chosen because it is frequently used to melt PLLA [135, 136]. Melting temperatures are generally not given for PLGA because it is amorphous. The same 200°C melting procedure was used for nHA/PLGA because its polymer component was 85% PLA, and glycolic acid has a much higher thermal degradation temperature than PLA. The nHA/PLGA was viscous and sticky after the melting process. The annealing procedure for PLGA was chosen because it reduced water uptake by the polymer the most effectively [137]. The annealing temperature for PLLA was chosen because PLLA formed smaller crystals at 115°C as compared with higher temperatures [138] and developed higher crystallinity at 115°C as compared with lower temperatures [139]. The nHA/PCL coatings were melted by heating at 80°C for 5 minutes, and/or annealed by heating at 50°C for 30 minutes; these temperatures were chosen based on the literatures [140, 141]. Annealing PCL at 50°C is known to reduce the diffusion of water soluble drugs more efficiently than lower annealing temperatures,

which demonstrates a greater reduction to water diffusion rates [142]. All samples were cooled in air at room temperature for 10 minutes after post-deposition processing. The non-coated Mg controls did not go through the post deposition processing since there were no polymers involved.

4.2.3- Measurement of Surface Hydrophobicity

The surface hydrophobicity influences water permeability and cell activities on the surfaces. The polymer types and post-deposition processing could significantly alter the hydrophobicity of the nanocomposite coatings. To determine the surface hydrophobicity, the contact angle on the sample surface was measured using a goniometer (EasyDrop; Krüss). Specifically, the advancing contact angles were measured 20 seconds after depositing 2 μL of deionized (DI) water on the surfaces. The contact angles of three replicate samples were measured for each sample type; and each sample was measured three times in three different areas. The average and standard error of the measurements were calculated and plotted. The contact angle measurements were performed for all different combinations of variable parameters of Mg substrate surface conditions (M_Mg and A_Mg), polymer types in the nanocomposite coatings (PLGA, PLLA, and PCL), and post-deposition processing (None, Annealed, Melted, and Melted then Annealed), as listed in Table 4.2.

Table 4.2: List of nHA/polymer nanocomposite coated Mg samples with all the processing parameters that were investigated, screened, and compared for optimal outcome. Contact angle was measured to compare surface hydrophobicity. Potentiodynamic polarization (PDP) curve was measured to select the samples with the lowest corrosion current. For each pair of polymer component and substrate surface type, only the prescribed post-deposition processing that resulted in the lowest corrosion current were included in the subsequent studies. Only the best combination of all the variables (substrate surface type, polymer component, and post-deposition processing) that reduced Mg degradation most effectively was selected for further studies with BMSCs.

Parameters of Interest			**■ Indicates the samples that were included in respective study**		
Substrate Surface	Polymer Types	Post-Deposition Processing	Contact Angle	Immersion Degradation	BMSC Adhesion
			PDP Curve	Coating Adhesion	
M_Mg	nHA/PLGA	None	■	■	
M_Mg	nHA/PLGA	Annealed	■		
M_Mg	nHA/PLGA	Melted	■		
M_Mg	nHA/PLGA	Melted then Annealed	■		
A_Mg	nHA/PLGA	None	■		
A_Mg	nHA/PLGA	Annealed	■		
A_Mg	nHA/PLGA	Melted	■		
A_Mg	nHA/PLGA	Melted then Annealed	■	■	
M_Mg	nHA/PLLA	None	■	■	
M_Mg	nHA/PLLA	Annealed	■		
M_Mg	nHA/PLLA	Melted	■		
M_Mg	nHA/PLLA	Melted then Annealed	■		
A_Mg	nHA/PLLA	None	■		
A_Mg	nHA/PLLA	Annealed	■		
A_Mg	nHA/PLLA	Melted	■		
A_Mg	nHA/PLLA	Melted then Annealed	■	■	
M_Mg	nHA/PCL	None	■		
M_Mg	nHA/PCL	Annealed	■		
M_Mg	nHA/PCL	Melted	■		
M_Mg	nHA/PCL	Melted then Annealed	■	■	■
A_Mg	nHA/PCL	None	■		
A_Mg	nHA/PCL	Annealed	■		
A_Mg	nHA/PCL	Melted	■		
A_Mg	nHA/PCL	Melted then Annealed	■	■	

4.2.4- Potentiodynamic Polarization Measurements for Corrosion Rates

The poteniodynamic polarization (PDP) study was performed according to ASTM standard G 102-89. The PDP tests were conducted in rSBF using a Potentiostat/galvanostat (model 273A; EG&G Princeton applied research) to screen the corrosion rates of all the samples prepared using different parameters. The rSBF was used because it represents the same ionic concentration as in human blood plasma [122]. Each sample served as the working electrode, with an Ag/AgCl electrode as the reference electrode (part # CHI111, CHI Instruments) and a Pt foil as the counter electrode (part # CHI 115, CHI Instruments). The electrodes were immersed in rSBF at 37 °C for the PDP measurements. For all the PDP measurements, the potential ranged from +1 V to -3 V, with a 10 mV step size and a 0.5-second step time at a 100 mV/s scan rate. On the PDP curves, straight lines were drawn along the linear portion; the corrosion current (I_{corr}) and corrosion potential (E_{corr}) were extrapolated from the intersection of these straight lines. The corrosion rate (CR) (in mm/year) of the samples was calculated using the following equation from ASTM standard G 102-89.

$$CR = \frac{I_{corr} \times K_1 \times EW}{\rho \times A} \qquad \text{Eq. 4.1}$$

Where I_{corr} is the corrosion current, K_1 is the constant for unit conversion, EW is the equivalent weight of Mg, ρ is the density of Mg, and A is the area of the sample submerged in rSBF. EW and ρ were calculated for the Mg substrates with 97 wt.% Mg and 3 wt.% Al. Specifically, $K_1=3.27\text{x}10^{-3}$ (mm•g)/(μA•cm•year), EW=12.05, ρ=1.76 g/cm^3, and A=1 cm^2. PDP measurements were performed in triplicate for each sample type listed in Table 4.2.

4.2.5- Degradation Measurements via Immersion in rSBF

For each combination of Mg surface condition and polymer type of the nanocomposite coatings, the post-deposition processing that resulted in the slowest corrosion rates in the PDP measurements were selected for the subsequent immersion study in rSBF, as shown in Table 4.2. On the M_Mg surfaces, no post-deposition processing showed slower corrosion rates for nHA/PLGA and nHA/PLLA coatings, and the post-deposition processing of melted and then annealed showed slower corrosion rates for the nHA/PCL coatings. On the A_Mg surfaces, the post-deposition processing of melted and then annealed showed slower corrosion rates. Thus, the degradation of these samples was further studied in immersion. Non-coated Ti, nHA/PLGA coated Ti without post-deposition processing, and epoxy disks were included as controls and references. The immersion study was performed in triplicate for each sample type.

For the immersion study, each sample was sterilized in enthanol (Koptec) for 1 hour, and then immersed in 4 mL of rSBF for 7 days under standard cell culture conditions (that is, at 37 °C, 5% CO_2/95% air, humidified, sterile environment). After each day of incubation (i.e., every 24-hour incubation period), each sample was collected, dried for at least 24 hours until reaching constant mass, and photographed under sterile condition. After every 24 hours of incubation, the rSBF was collected for pH and ionic concentration measurements, and fresh sterile rSBF was added. The pH of rSBF was measured immediately after collection. The ionic concentration of rSBF was measured using inductively coupled plasma - optical emission spectrometry (ICP-OES; Optima 8000, Perkin-Elmer). The rSBF collected at every 24 hours was diluted to 1/100 in DI

water for measuring [Mg^{2+}] and [Ca^{2+}] using the ICP-OES. The ICP-OES system was calibrated using 0.5-5.0 mg/L Mg^{2+} standards and 0.1-1.0 mg/L Ca^{2+} standards.

After 7 days of immersion in rSBF, the samples were examined using scanning electron microscopy (SEM; Nova NanoSEM 450, FEI Co.) under low vacuum conditions with a 5 kV accelerating voltage. The surface elemental composition of the samples was measured using energy dispersive x-ray spectroscopy (EDX) under low vacuum conditions with a 15 kV accelerating voltage. All samples for SEM and EDX analyses were sputter-coated with Pt/Pd at 10 mA for 30 seconds (Cressington; Sputter Coater 108 Auto). The samples before the immersion study was also analyzed using SEM and EDX for comparison.

4.2.6- Measurements of Coating Adhesion Strength

Tensile testing was used to measure the coating adhesion strength before and after immersion, as illustrated in Figure 4.1. A mechanical testing system (Model #5969, Instron) was used to perform the tensile testing at an extension rate of 1 mm/minute. The coated samples were mounted for tensile testing following a procedure modified from the literature [89]. Specifically, two wooden rods with a dimension of 5 x 5 x 50 mm were mounted onto the top and bottom of the samples, which were then secured into the Instron grips (Figure 4.1). One of the wooden rod was attached to the surface of the nanocomposite coatings using cyanoacrylate-based adhesive (Loctite) and allowed to cure for 24 hours at room temperature. This wooden rod was then fixed into the upper Instron grip for moving upwards during tensile testing. Another wooden rod was embedded in the cylindrical epoxy (Jetset; MetLab, catalog # M135A) jigs to secure the

bottom of the samples, and then fixed into the lower Instron grip that remained stationary during tensile testing. It is important to mention that the coating was outlined around the perimeter of the attached wooden rod using a sharp blade, to ensure that it was the coating adhesion strength being measured, not the tensile strength of the coating material. The tensile testing was set to stop when the measured load dropped by 40%. The stress-strain curve was plotted to calculate the coating adhesion strength.

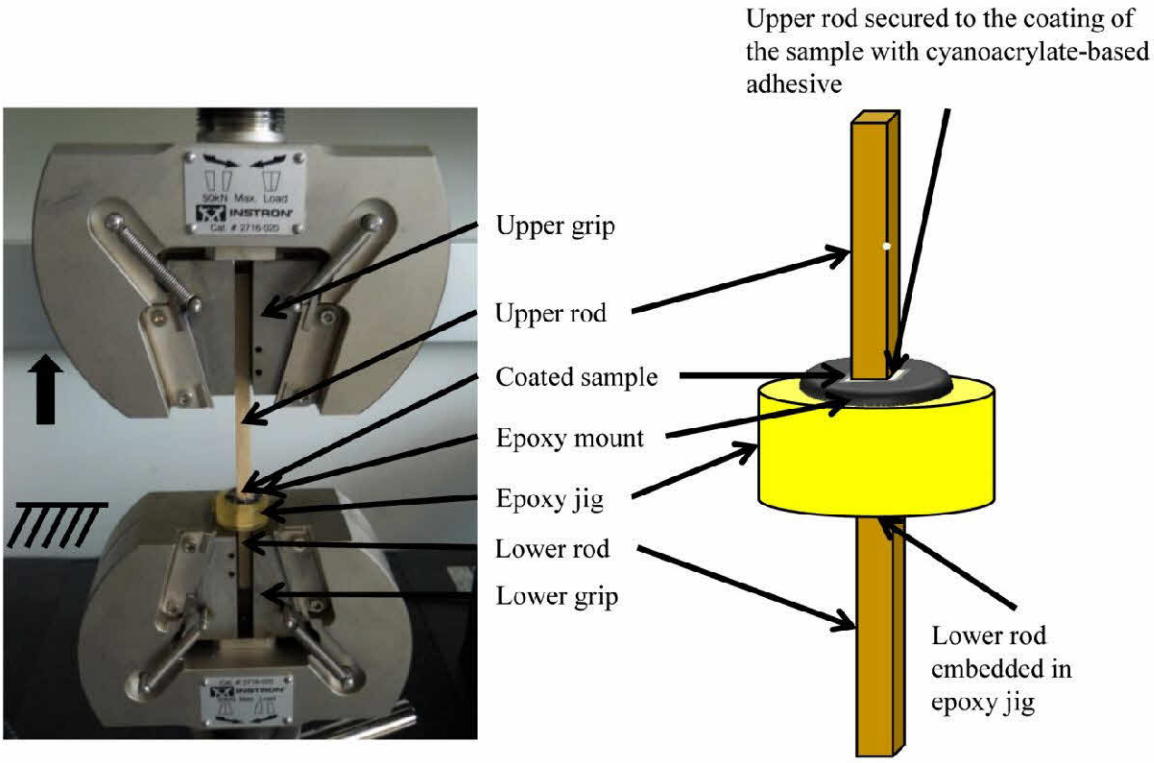

Figure 4.1: Experimental setup for measuring coating adhesion strength. Tensile testing was performed to measure the maximum force needed to detach the coating from the substrate. The maximum force was used to calculate the coating adhesion strength.

4.2.7- BMSC Study *In Vitro*

Bone marrow derived mesenchymal stem cells (BMSCs) were harvested from the marrow cavity of the femur and tibia of Sprague-Dawley rat weanlings for culturing with

the best sample that showed the slowest degradation and the best coating adhesion, i.e., nHA/PCL coated M_Mg with the post-deposition processing of melting and then annealing. Non-coated M_Mg, nHA/PCL films without Mg substrates, epoxy mounts without Mg substrates, glass, and polystyrene-tissue culture plate (PSTC) were used as controls and references. All samples were run in triplicate. The rat weanlings were euthanized by CO_2 asphyxiation using an established protocol approved by the Institutional Animal Care and Use Committee (IACUC) at the University of California at Riverside [143]. The distal ends of the femur and tibia were removed so that bone marrow could be flushed out with Dulbecco's Modified Eagle Medium (DMEM; Sigma Aldrich) supplemented with 10% fetal bovine serum (FBS; HyClone) and 1% penicillin/streptomycin (P/S; Invitrogen). The DMEM supplemented with 10% FBS and 1% P/S will be referred to as DMEM. A 70 μm nylon strainer was used to separate cell aggregates and remove tissue debris. The harvested BMSCs were cultured in DMEM under standard cell culture conditions to reach 90% confluency.

The samples were sterilized in ethanol for 1 hour before BMSC culture, placed into the wells of a 12-well tissue culture treated plate, and washed with 2 mL of DMEM to prepare the local environment for cell seeding. The BMSCs were detached using Trypsin (Invitrogen), seeded onto the samples at a concentration of 10,000 cells/cm^2, and incubated for 24 hours under standard cell culture conditions. After 24 hours of culture, each sample was washed with PBS to remove non-adherent cells. The adherent cells were fixed with 4% paraformaldehyde, and stained with Alexa Fluor® 488-phalloidin for F-actin and 4',6-diamidino-2-phenylindole (DAPI; Invitrogen) for nucleic acids. Five

random locations on the samples were imaged using a fluorescence microscope (Eclipse Ti; Nikon) with a 10x objective lens. The DAPI stained nuclei were counted in each image to calculate the average cell adhesion density (cells/cm^2). The stained F-actin was used to calculate the cell spreading area, maximum Feret diameter, and minimum Feret diameter using ImageJ. The aspect ratio of the BMSCs was calculated by dividing the maximum Feret diameter by the minimum Feret diameter.

4.2.8- Statistical Analyses

R was used to perform the statistical analyses. The normal distribution of the data was checked using the Shapiro-Wilks test. Homogeneity of variance was checked using the Bartlett test. The distribution and variance of the data were used to determine the suitable statistical tests.

The corrosion rates of the coated Mg substrates from the PDP measurements were analyzed using factorial ANOVA, after a cubic root transformation was applied to the data to ensure normal distribution and homogeneous variance. Factorial ANOVA was used to reveal the interactions between experimental parameters. The non-coated Mg substrates were not included in the factorial ANOVA analysis because their corrosion rates were much greater than the coated Mg substrates and did not have a normal distribution or homogenous variance. An unpaired two-tailed t-test was thus used to compare the corrosion rates of the non-coated M_Mg and A_Mg substrates.

A wild bootstrap test with Bonferroni correction was used to analyze the effects of the coating polymer component, the post-deposition processing, the substrate surfaces, and the immersion time on the [Mg^{2+}] measured in the immersion study, the key indicator

of the sample degradation rate. The wild bootstrap was used because the [Mg^{2+}] data did not have normal distribution or homogeneous variance. The Bonferroni correction was used to control familywise error. The data was stratified for each time point of immersion study in the wild bootstrap test.

The coating adhesion strengths before immersion and after immersion were separately examined using the Kruskal-Wallis test, and the results did not show statistically significant difference. This was mainly due to outliers that increased the standard deviation, and the small number of samples tested.

The Kruskal-Wallis test was used to analyze the data from the *in vitro* BMSC study to determine the statistical significance of sample type on cell adhesion density, cell spreading area, and cell aspect ratio. The Kruskal-Wallis test was used because the data did not have normal distribution or homogeneous variance. Post-hoc comparisons were made using the Dunn test with the Bonferroni correction.

4.3- Results

4.3.1- Thickness of the Nanocomposite Coatings on Mg Substrates

The thickness of the nanocomposite coatings on Mg substrates was measured, as listed in Table 4.1. The optical images of the sample cross sections are shown in Figure 4.2. The coating thickness was controlled at the narrow range of 30-40 μm for direct comparison of the effects of the nanocomposite coating parameters on the degradation of Mg substrates. It is important to mention that the coating thickness can be adjusted to control the degradation of Mg substrates if needed. However, the objective of this study

was to elucidate the effects of the parameters of nanocomposite coatings (i.e., substrate surface conditions, polymer types, and post-deposition processing). Thus, the coating thickness was not treated as a variable in this study.

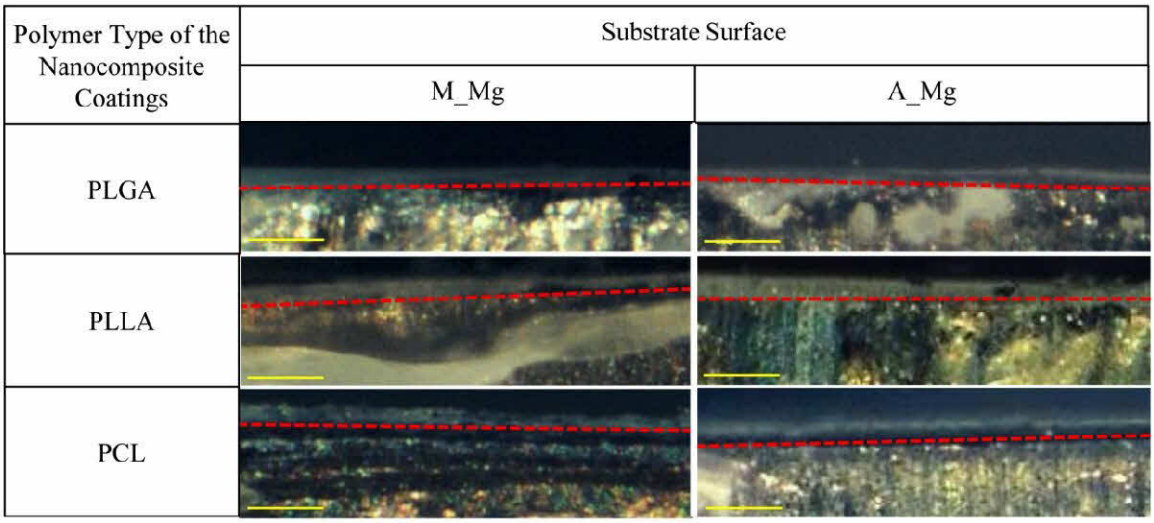

Figure 4.2: Optical images of cross-sections of nHA/polymer nanocomposite coatings on Mg substrates. The red dashed line indicates the interface of the coating (top) and the Mg substrate (bottom). Scale bars = 100 μm.

4.3.2- The Effects of the Coating Parameters on Surface Hydrophobicity

Surface hydrophobicity has been known to affect water permeability [144] and bioactivity [145-147]. Figure 4.3 shows the contact angles of deionized water on the nHA/polymer nanocomposite coatings on Mg substrates and non-coated Mg control substrates. The greater contact angle indicates the surface is more hydrophobic. The contact angles of the nanocomposite coated Mg substrates ranged from 74-86, and the M_Mg and A_Mg control substrates had a respective contact angle of 57 and 78. The contact angles of the nanocomposite coated Mg substrates varied in a relatively narrow range.

The nHA/PLGA coatings on M_Mg without post-deposition processing showed a slightly lower contact angle than the rest of nHA/PLGA coatings. For the nHA/PLLA coatings, the post-deposition processing of melting then annealing increased the coating contact angles on both M_Mg and A_Mg substrates. Melting caused slight increase in the contact angles of nHA/PLLA as compared with its corresponding coatings without heat treatments. For the nHA/PCL coatings, the post-deposition processing of melting then annealing slightly increased the average contact angle on both M_Mg and A_Mg substrates.

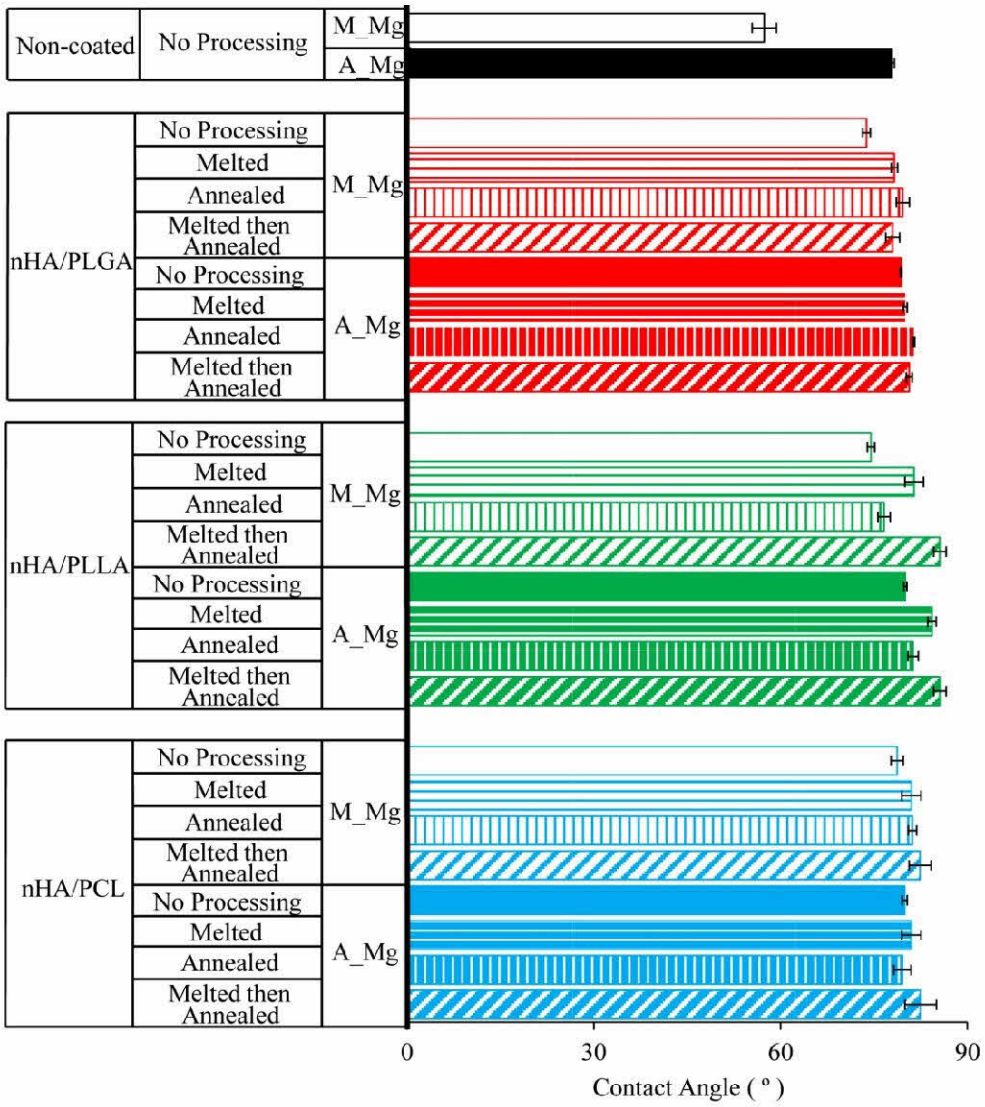

Figure 4.3: Contact angles of deionized water on the nHA/polymer coatings on Mg substrates and non-coated Mg control substrates. Values are mean ± standard error; n=9.

4.3.3- The Effects of the Coating Parameters on Corrosion Rates Calculated from PDP Testing

The representative PDP curves for the nanocomposite coated and non-coated Mg substrates with different post-deposition processing were plotted (Figure 4.4). The nHA/PLGA and nHA/PLLA coatings reduced the I_{corr}, but had little effect on the E_{corr}. In contrast, the nHA/PCL coatings reduced the I_{corr}, and some also had significant effect on E_{corr}. Post-deposition processing reduced the I_{corr} for the nHA/PLGA and nHA/PLLA coated A_Mg substrates, but showed little effect on the respective coatings on M_Mg substrates. The nHA/PCL coated M_Mg and A_Mg had similar E_{corr} and I_{corr} before post-deposition processing. Post-deposition processing reduced I_{corr} more on the nHA/PCL coated A_Mg substrates than the M_Mg substrates. Post-deposition processing also increased the E_{corr} for the nHA/PCL coated A_Mg substrates but had little effect on the E_{corr} for the M_Mg substrates.

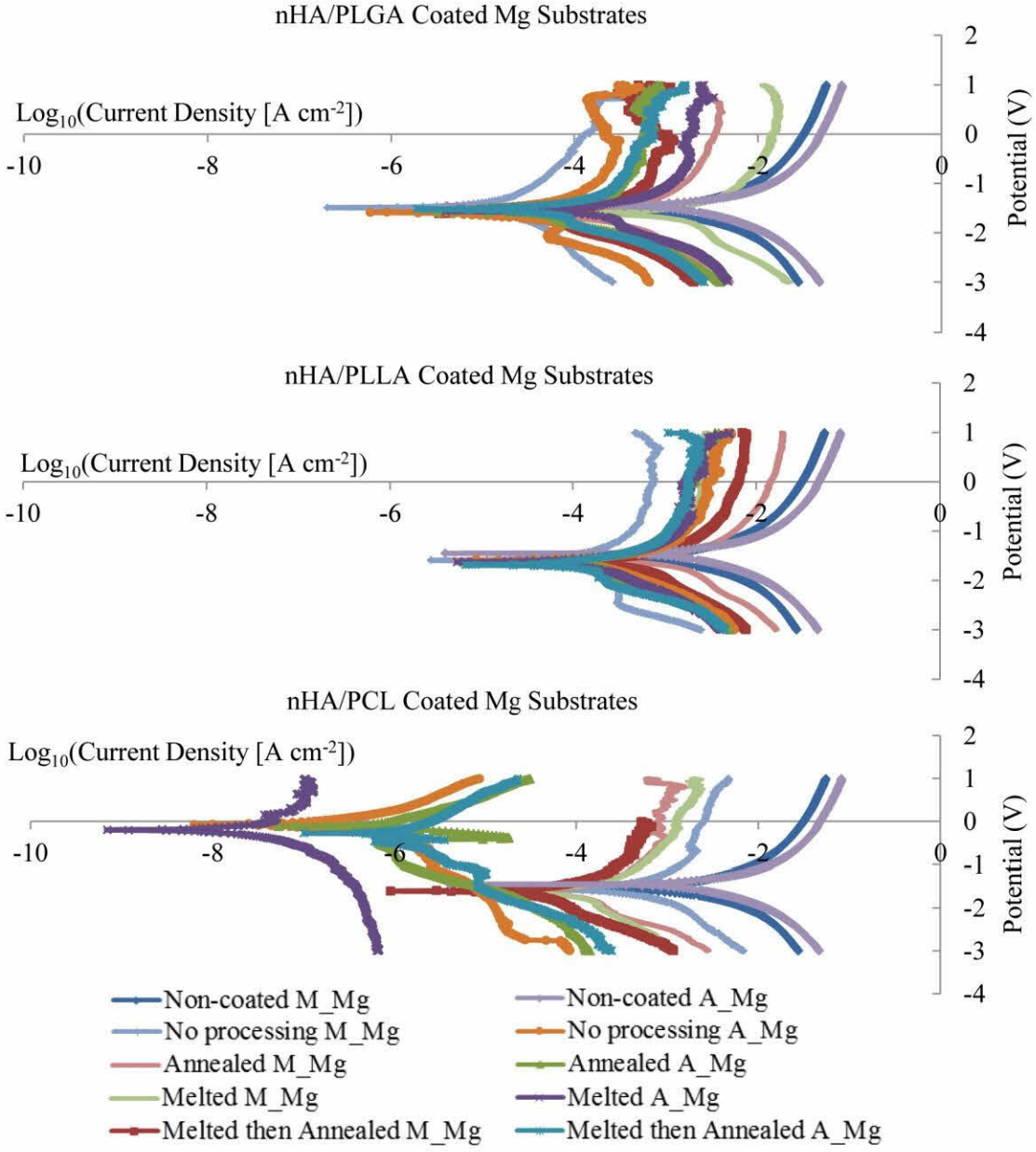

Figure 4.4: Representative potentiodynamic polarization curves of the nHA/polymer coated and non-coated Mg substrates with different post-deposition processing for the coatings on M_Mg and A_Mg.

The corrosion rates were calculated based on the corrosion current density extrapolated from PDP curves, as shown in Figure 4.5. All of the nanocomposite coatings reduced the corrosion rates as compared with the non-coated Mg substrates. When comparing the non-coated M_Mg with A_Mg substrates using a two-tailed t-test, their corrosion rates did not show statistically significant difference ($p = 0.24$). However, Mg substrate surface conditions did show statistically significant effects on the corrosion rates of the nanocomposite coated samples in factorial ANOVA, because the other parameters (polymer types, and post-deposition processing) interacted with Mg substrate surface conditions (i.e., M_Mg versus A_Mg). Specifically, the post-deposition processing increased the corrosion rates of nHA/PLGA and nHA/PLLA coated M_Mg substrates, but the post-deposition processing of melting then annealing reduced the corrosion rates of the respective coatings on A_Mg substrates. Post-deposition processing reduced the corrosion rates of nHA/PCL coated M_Mg and A_Mg. The nHA/PCL coated A_Mg substrates that underwent post-deposition processing showed the lowest corrosion rate among all of the sample types.

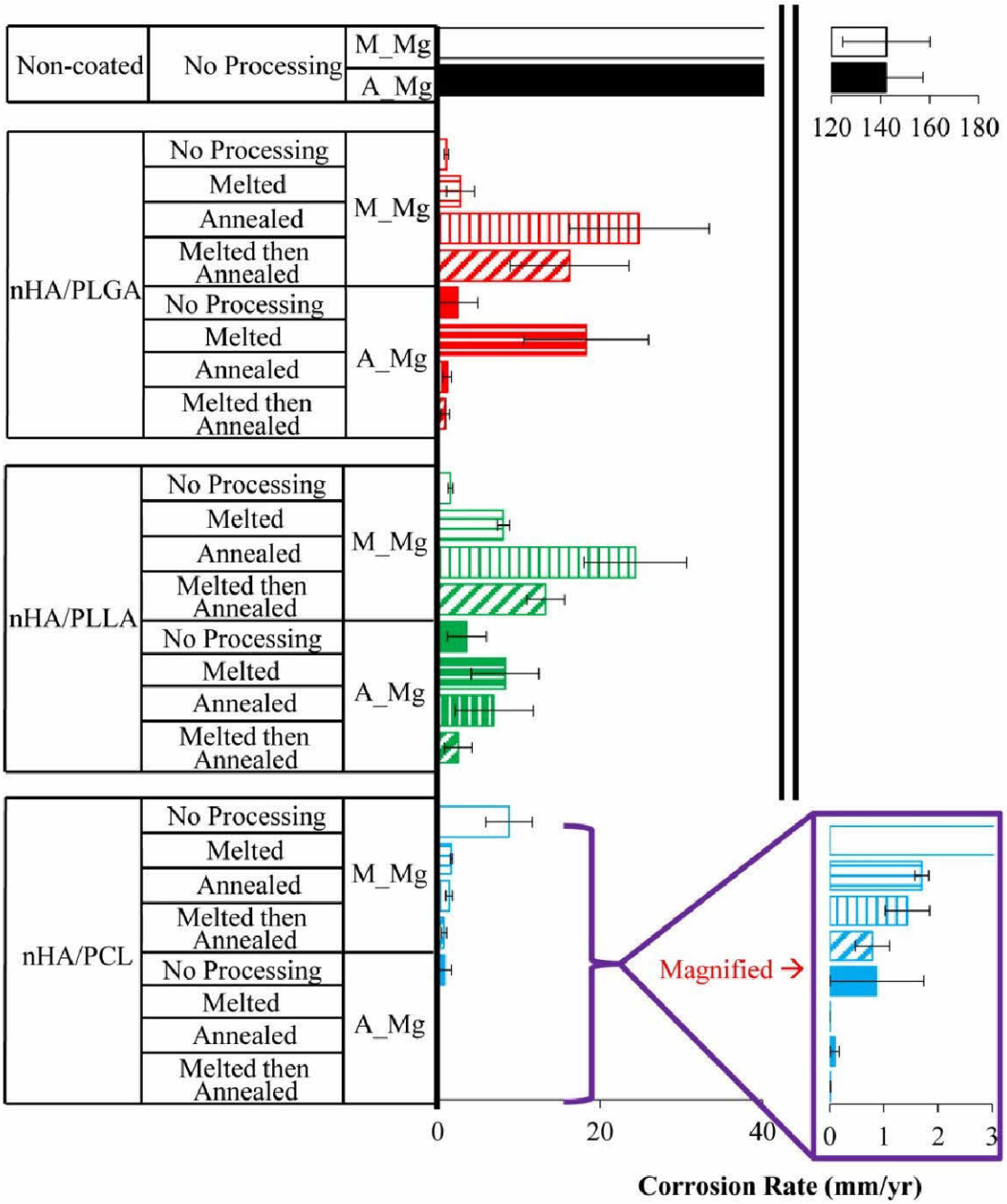

Figure 4.5: Corrosion rates of the nHA/polymer coated and non-coated Mg substrates that were calculated based on corrosion current density extrapolated from PDP curves. All coatings significantly reduced corrosion rates as compared with the non-coated Mg substrates. The post-deposition processing had different effects on corrosion rates, depending upon polymer component and substrate surface. Values are mean ± standard error; n=3.

The interactions of the coating parameters (polymer component of the nanocomposite coating, substrate surface, and post-deposition processing) were analyzed using factorial ANOVA, as summarized in Figure 4.6. Based on the *p* values in Figure 4.6D, most parameters showed statistically significant interactions, except the interaction between polymer component and substrate surface. In Figure 4.6A, the lines in the interaction plot for polymer component and substrate surface were parallel or near-parallel, indicating no or little interactions detected. Furthermore, all three lines for the polymer components sloped downwards from the M_Mg to A_Mg substrates, indicating slower corrosion rates on the A_Mg substrates. The line for the PLGA component was slightly below the line for the PLLA component, indicating that PLGA component had a slightly slower average corrosion rate. The line for the PCL component was far below the other two lines, indicating that nHA/PCL coating reduced the corrosion rate more significantly than the other two polymer types. In Figure 4.6B, some lines in the interaction plot for post-deposition processing and substrate surface were intersected, indicating statically significant interactions between them. The two lines for the annealing and the melting then annealing treatments were near parallel to each other, indicating these two heat treatments had similar effects on corrosion rates; their steeper slopes indicate that they significantly decreased the corrosion rates on the A_Mg substrates. The line for the melting treatment was nearly horizontal, suggesting the melting treatment had similar effects on the corrosion rates for M_Mg and A_Mg substrates. In Figure 4.6C, the interaction plot for post-deposition processing and polymer

component showed that post-deposition processing affected PCL differently than the other two polymer types. That is, the post-deposition processing increased the corrosion rates for the PLGA and PLLA polymer types, but decreased the corrosion rates for the PCL polymer type. The three lines for the post-deposition processing of annealing, melting, and melting then annealing were nearly parallel to each other, and showed a slight upward slope from the PLGA to PLLA polymer types and a steep downward slope to the PCL polymer type. The fourth line for no post-deposition processing was nearly straight, showed a slight upward slope from the PLGA, PLLA to the PCL polymer types, and intersected with the post-deposition processing lines at the positions above PCL but below PLGA and PLLA.

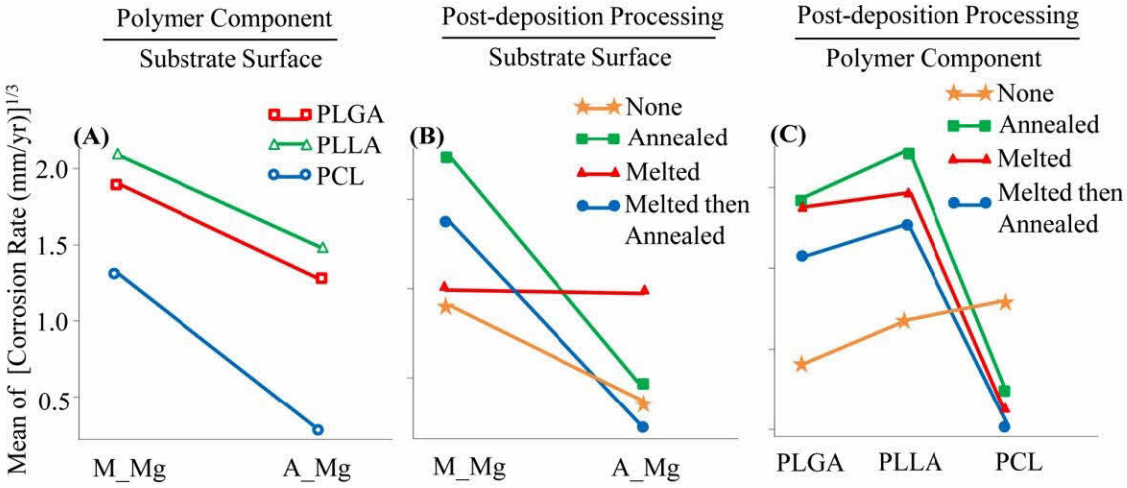

(D) Sample Type	*p* Value
Polymer Component	1.89×10^{-7}
Post-deposition Processing	0.04
Substrate Surface	5.83×10^{-7}
Polymer Component : Post-deposition Processing	3.39×10^{-3}
Polymer Component : Substrate Surface	0.35
Post-deposition Processing : Substrate Surface	3.98×10^{-3}
Polymer Component : Post-deposition Processing : Substrate Surface	4.90×10^{-3}

Figure 4.6: Interaction plots of the effects of polymer component of the nanocomposite coating, substrate surface, and post-deposition processing on corrosion rates. (A) Parallel or near-parallel lines indicate that no or little interactions were detected between polymer component and substrate surface. (B) Intersecting lines indicate statistically significant interactions between the post-deposition processing and substrate surface. (C) Intersecting lines indicate statistically significant interactions between the post-deposition processing and polymer component of the nanocomposite coating. These complex interactions suggested that post-deposition processing should be optimized for each specific pair of polymer component and substrate surface.

4.3.4- Degradation Results from the Immersion Study

The immersion study was performed in rSBF for 7 days to investigate the surface changes during immersion, and ion release from the sample degradation, which complemented the PDP measurements.

4.3.4.1- Surface Changes during Immersion Degradation

For each type of nHA/polymer nanocomposite coating on M_Mg or A_Mg substrate, the post-deposition processing that provided the slowest corrosion rate (Figure 4.5) was selected for further investigation of the sample degradation in the immersion study, as summarized in Table 4.2. That is, no post-deposition processing was used for the nHA/PLGA and nHA/PLLA coatings on M_Mg substrates, and the post-deposition processing of melted and then annealed was used on A_Mg substrates. The post-deposition processing of melted and then annealed was used for the nHA/PCL coatings on both M_Mg and A_Mg substrates. All of these nanocomposite coatings significantly reduced the degradation rate of Mg substrates without delamination after 7 days of immersion in rSBF (Figure 4.7). During the 7 days of immersion, the samples were observed and photographed every 24 hours, but only the images of 1, 3, 5, and 7 days were included in Figure 4.7 to compare with the respective sample before immersion (day 0). In general, all the coated or non-coated Mg samples showed some degree of change during the 7 days, when compared with the coated or non-coated Ti control. The epoxy that was used as the control for the mounting material showed no visible changes throughout the entire 7 days of immersion. During the immersion, small blisters were observed on the coated Mg substrates, but not on the coated Ti substrates. After 5 days of immersion, only the nHA/PLLA coatings on the A_Mg substrates showed a large blister emerged from small blisters. After 7 days of immersion, the nHA/PCL coatings on the M_Mg substrates showed much less blisters than the respective coatings on A_Mg substrates.

Coating	Post-deposition Processing	Substrate Surface	Immersion Time (Days)				
			0	1	3	5	7
Non-coated	No Processing	M_Mg					
		A_Mg					
nHA/PLGA	No Processing	M_Mg					
	Melted then Annealed	A_Mg					
nHA/PLLA	No Processing	M_Mg					
	Melted then Annealed	A_Mg					
nHA/PCL	Melted then Annealed	M_Mg					
		A_Mg					
Non-coated	No Processing	Ti					
nHA/PLGA	No Processing	Ti					
Non-coated	No Processing	Epoxy					

Figure 4.7: Photographs of sample surface morphology after immersion in rSBF for the prescribed period.

4.3.4.2- Analyses of the pH and Ion Concentrations in rSBF during Immersion Degradation

Figure 4.8 shows the pH measurements and ion concentrations in rSBF during immersion degradation. As shown in Figure 4.8A, all of the nanocomposite coatings significantly reduced the alkaline pH in the rSBF as compared with the non-coated Mg substrates. The non-coated Mg substrates showed the highest pH in rSBF throughout the immersion, while the controls without Mg substrates, i.e., rSBF only, epoxy mount, non-coated Ti, and nHA/PLGA coated Ti, had negligible effect on the pH of the immersion media. Generally, the nHA/PCL coated Mg substrates showed lower pH than the nHA/PLGA and the nHA/PLLA coated Mg substrates. The nHA/PCL coated M_Mg and A_Mg had similar pH on day 1, but later the nHA/PCL coated M_Mg showed lower pH than the same coating on A_Mg on day 2, 3, 4, and 7. Figure 4.8B shows the Mg^{2+} ion concentrations [Mg^{2+}] in rSBF during immersion, the key indicator of Mg degradation. All of the nanocomposite coatings reduced the release of Mg^{2+} ions when compared with the non-coated Mg substrates. In consistent with the pH results, the nHA/PCL coated Mg substrates showed much lower [Mg^{2+}] in rSBF than the nHA/PLGA and nHA/PLLA coated Mg substrates. Moreover, the nHA/PCL coated M_Mg showed lower [Mg^{2+}] in rSBF than the same coating on A_Mg. Remarkably, the nHA/PCL coated M_Mg showed very similar [Mg^{2+}] as the controls that did not contain Mg and the baseline [Mg^{2+}] in rSBF. Figure 4.8C shows the Ca^{2+} ion concentrations [Ca^{2+}] in rSBF during immersion, which ranged from 1.6 to 2.3 mM in average for all the sample types, a much narrower distribution than [Mg^{2+}]. In average, the [Ca^{2+}] decreased for all Mg containing samples,

but did not change much for the Ti-based and epoxy controls, when compared with the baseline [Ca^{2+}] in rSBF. Among the Mg-based samples, non-coated Mg samples showed the lowest [Ca^{2+}], nHA/PCL coated Mg samples showed the highest [Ca^{2+}], and nHA/PLGA and nHA/PLLA coated Mg samples were in between.

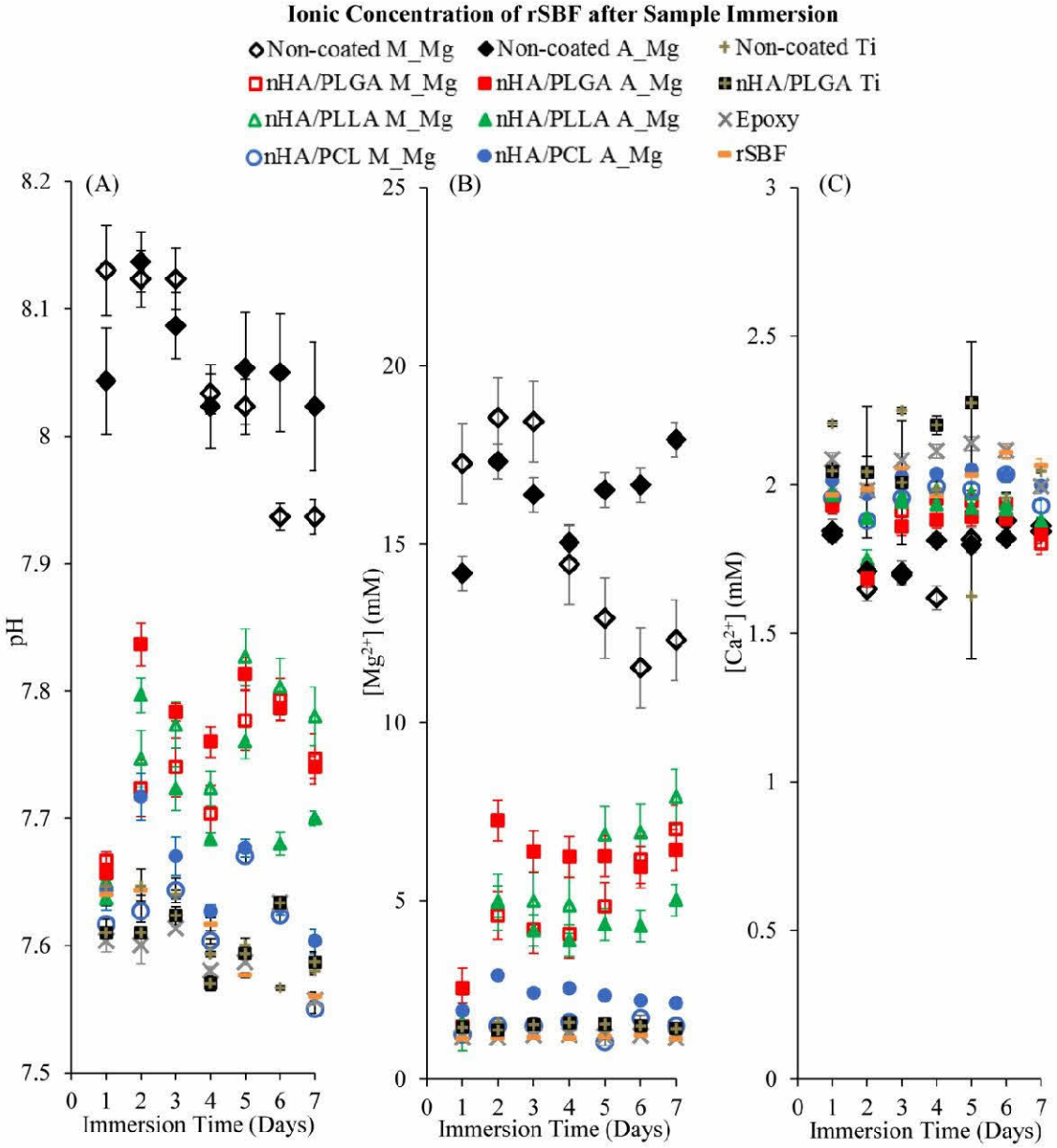

Figure 4.8: Characterization of rSBF immersion media. (A) pH of the rSBF, (B) $[Mg^{2+}]$, and (C) $[Ca^{2+}]$ in the rSBF after sample immersion under standard cell culture conditions for the prescribed period. Values are mean ± standard error; n=3.

The statistical analyses of the parameters that influenced Mg degradation in immersion study are summarized in Table 4.3. The interactions among the parameters of substrate surface conditions, the types of polymer component in the nanocomposite

coatings, and immersion time showed statistically significant effect on Mg degradation, i.e., [Mg^{2+}] in rSBF, except the interactions of substrate surface:polymer component:time. This corroborates the statistical analyses of the corrosion rates reported in Figure 4.6D. Moreover, the substrate surface alone (M_Mg versus A_Mg) did not show any significant effect on Mg degradation in rSBF in terms of pH and [Mg^{2+}], although non-coated M_Mg showed less release of Mg^{2+} ions in average than the non-coated A_Mg after 5 days of immersion in rSBF.

Table 4.3: Statistical analysis of the parameters that affected Mg degradation in immersion study using the Wild Bootstrap method. The [Mg^{2+}] concentration was measured as the key indicator of Mg degradation after immersion in the rSBF.

Statistical Significance of the Parameters and their Interactions that Affected Mg Degradation	
Parameter	**Bonferroni Corrected *p* Values**
Substrate Surface	1
Polymer Component	5.97×10^{-5}
Time	5.97×10^{-5}
Substrate Surface : Polymer Component	3.9×10^{-3}
Substrate Surface: Time	1.49×10^{-2}
Polymer Component : Time	3.9×10^{-4}
Substrate Surface : Polymer Component : Time	0.6

4.3.4.3- Surface Characterization Before and After Immersion Degradation

Figure 4.9 shows the SEM images of the nanocomposite coated and non-coated Mg samples before and after immersion in rSBF for 7 days. The nHA/PLGA coatings and nHA/PCL coatings remained intact on both M_Mg and A_Mg substrates. The nHA/PCL coated M_Mg and A_Mg attracted significant deposition after immersion, and the deposition appeared to be more abundant on the nHA/PCL coated M_Mg than the same coating on A_Mg. However, the nHA/PLGA coatings on the A_Mg substrates showed large cracks and craters after 7 days of immersion, which were not observed for

the same coatings on the M_Mg substrates. Figure 4.10 shows the craters formed in the nHA/PLGA coating on A_Mg after 7 days of immersion in rSBF due to H_2 gas evolution from Mg degradation.

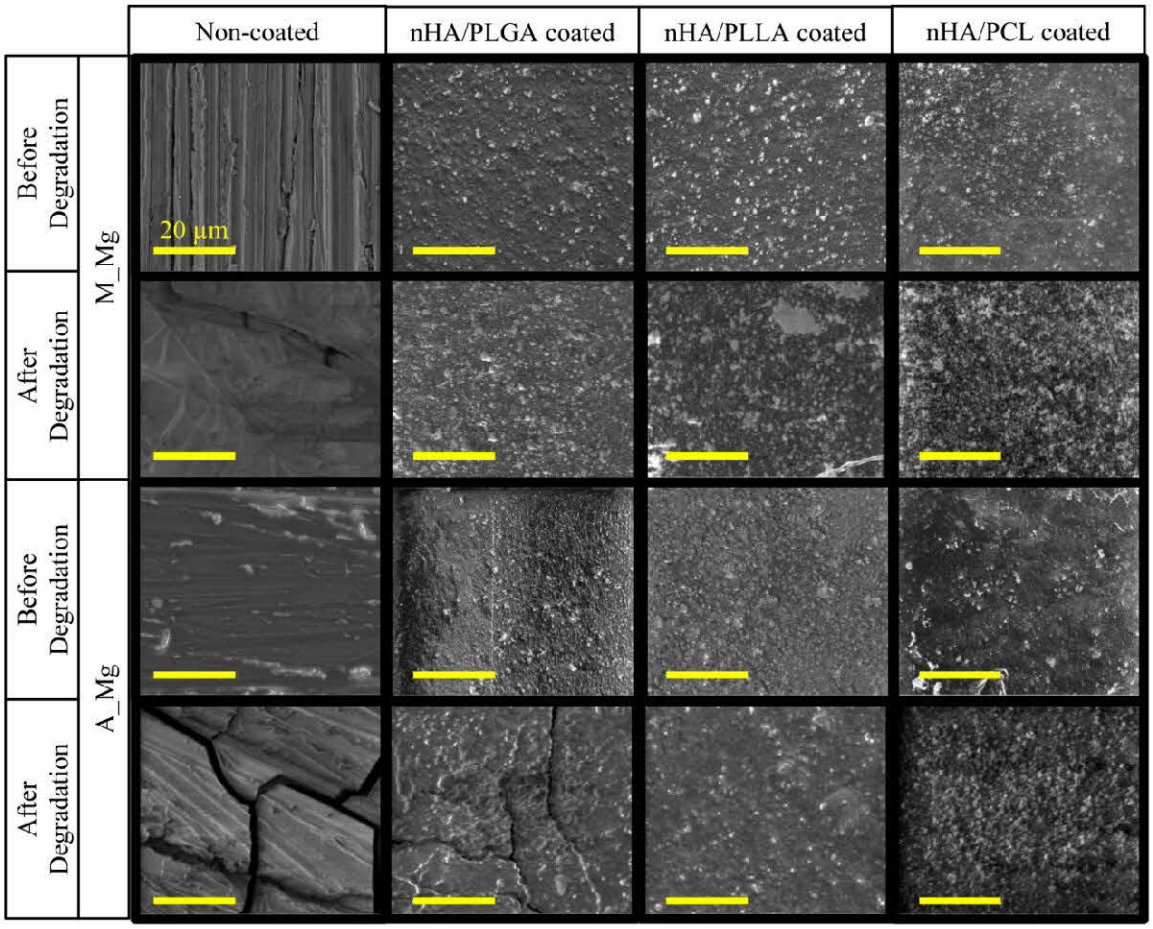

Figure 4.9: SEM images of the samples before and after immersion in rSBF for 7 days. Scale bars = 20 µm.

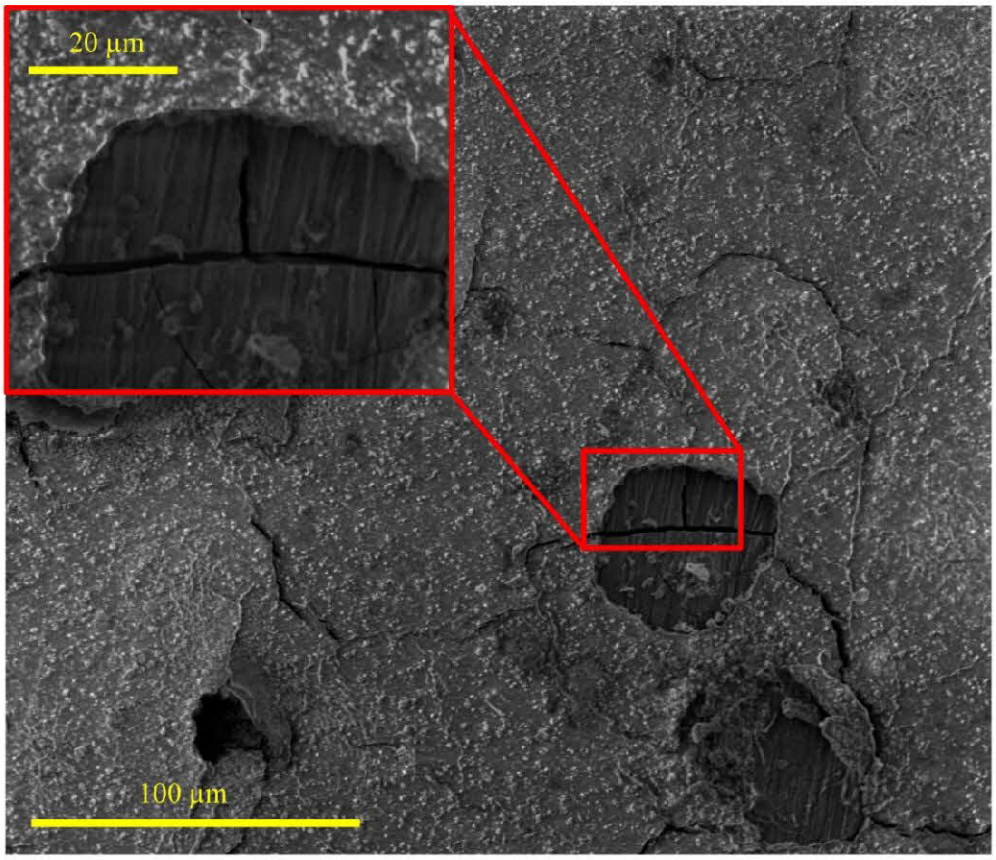

Figure 4.10: SEM image of craters in the nHA/PLGA coating on A_Mg after 7 days of immersion in rSBF. The craters formed due to hydrogen gas evolution from Mg degradation.

Figure 4.11 shows the surface elemental compositions of the nanocomposite coated and non-coated Mg samples before and after immersion in rSBF for 7 days. All of the nanocomposite coated Mg samples showed C, O, Ca and P as the main elements on the surface before and after immersion in rSBF. Mg was not detected on any of the nanocomposite coated Mg samples before immersion. The amount of Ca and P increased on the surface of nHA/PLGA and nHA/PCL coated Mg but not on nHA/PLLA coated M_Mg. The non-coated Mg substrates did not show Ca and P on the surface before immersion, but showed Ca and P on the surface after immersion. Before immersion, non-

coated A_Mg showed greater amount of C and O, while non-coated M_Mg showed greater amount of Mg.

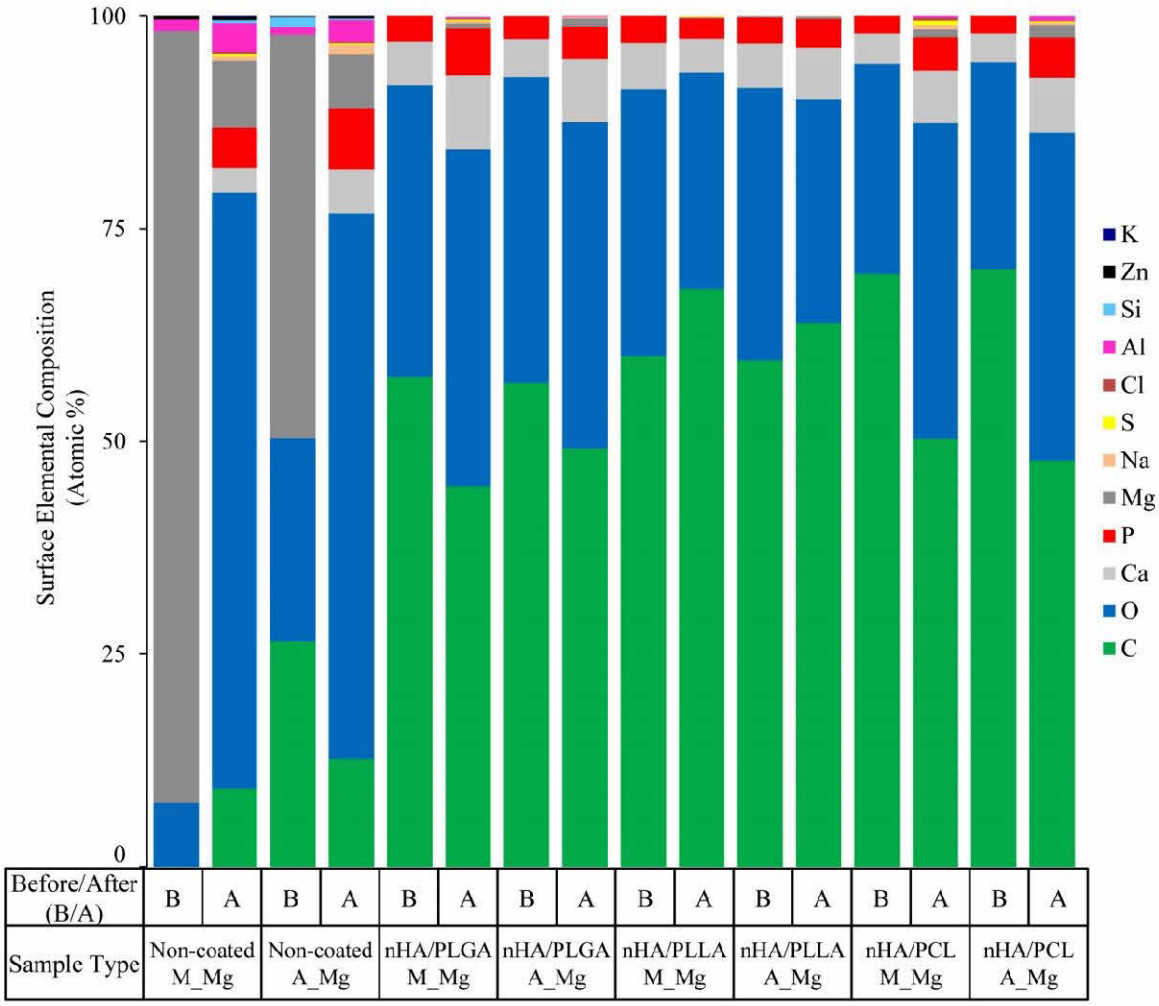

Figure 4.11: Surface elemental compositions of the nanocomposite coated Mg and non-coated Mg before and after immersion in rSBF for 7 days, according to EDX analyses.

4.3.5- Coating Adhesion Strength

Figure 4.12 shows the coating adhesion strength before and after immersion in rSBF for 7 days. Before immersion, the nHA/PLGA and nHA/PLLA coatings showed similar adhesion strengths around 9 MPa, and the nHA/PCL coatings showed slightly higher adhesion strengths at 11-12 MPa. The Mg substrate surface conditions (M_Mg versus A_Mg) had negligible effect on the coating adhesion strength before immersion. After 7 days of immersion, all of the nanocomposite coatings showed significantly reduced adhesion strength. After immersion, the nHA/PCL coated M_Mg showed the greatest adhesion strength among all the sample types, with the average adhesion strength of 0.9 MPa. In contrast, the nHA/PCL coated A_Mg showed the average adhesion strength of 0.13 MPa after immersion. The nHA/PLGA coated M_Mg and A_Mg showed similar coating adhesion strength at 0.14-0.15 MPa after immersion. The nHA/PLLA coated M_Mg showed slightly higher coating adhesion strength than the same coating on A_Mg after immersion, 0.15 MPa versus 0.05 MPa, respectively.

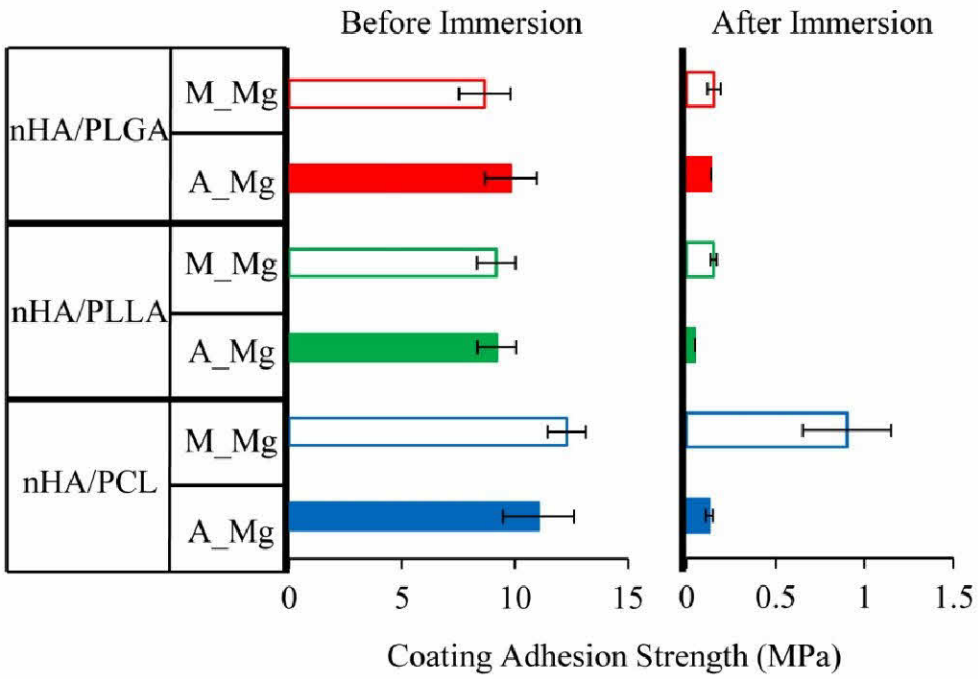

Figure 4.12: Coating adhesion strength measured before and after immersion in rSBF for 7 days. Values are mean ± standard error; n=2.

4.3.6- BMSC Adhesion and Morphology

Figure 4.13 shows the representative fluorescence images of BMSCs directly cultured on the samples and controls for 24 hours. Figure 4.14 shows the quantified results of BMSC adhesion density, spreading area, and aspect ratio. Kruskal-Wallis tests showed that the sample type had statistically significant effects on BMSC adhesion density (p=2.2x10^{-16}), spreading area (p=2.2x10^{-16}), and aspect ratio (p=1.2x10^{-4}). Pairwise comparisons using the Dunn test showed that the nHA/PCL coatings minimized the impact of Mg degradation upon the BMSCs, as described below (Figure 4.14).

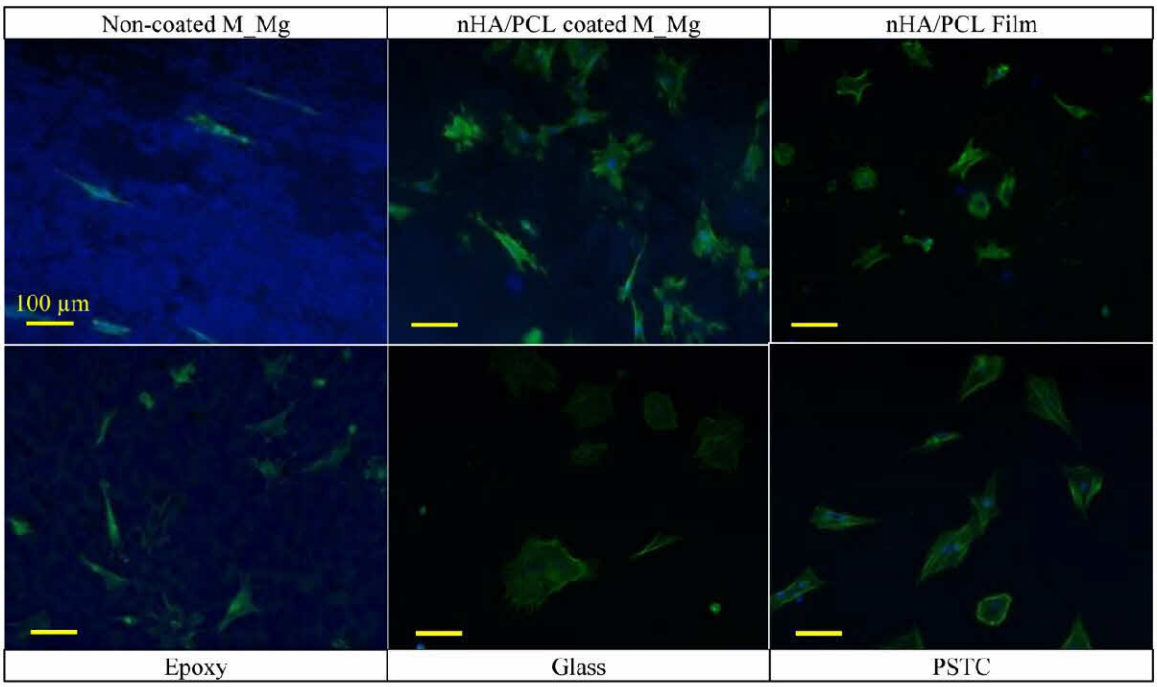

Figure 4.13: Fluorescence images of BMSCs after direct culture on the samples and controls for 24 hours. Blue indicates DAPI stained nuclei and green indicates Alexa Fluor® 488 stained F-actin. Scale bars = 100 µm.

In average, the nHA/PCL coated M_Mg substrates showed the greatest BMSC adhesion density, the non-coated M_Mg showed the least, and the control samples of nHA/PCL film, epoxy, glass, and PSTC were in between (Figure 4.14A). The results of the pairwise comparisons showed that the nHA/PCL coated Mg was statistically different from all samples except for PSTC and epoxy, which had the second and third highest average BMSC adhesion, respectively.

The BMSCs on non-coated M_Mg, nHA/PCL coated M_Mg, nHA/PCL film, and epoxy samples had average spreading areas that were well below 3000 μm^2 per cell (Figure 4.14B). The glass and PSTC samples had higher spreading areas of over 4000 μm^2 per cell. The results of the pairwise comparisons showed that the nHA/PCL coated

Mg was statistically different from the nHA/PCL film, non-coated Mg, and PSTC. The epoxy samples had the closest average spreading area to nHA/PCL coated Mg, and the glass samples had a large standard deviation; which is why their spreading areas were not statistically different from nHA/PCL coated Mg.

The BMSCs had a much higher average aspect ratio of 3.7 on non-coated M_Mg, and the rest of samples and controls had an aspect ratio of 1.6-1.9 (Figure 4.14C). The results of the pairwise comparisons showed that no pairs were statistically different unless the pair included non-coated Mg.

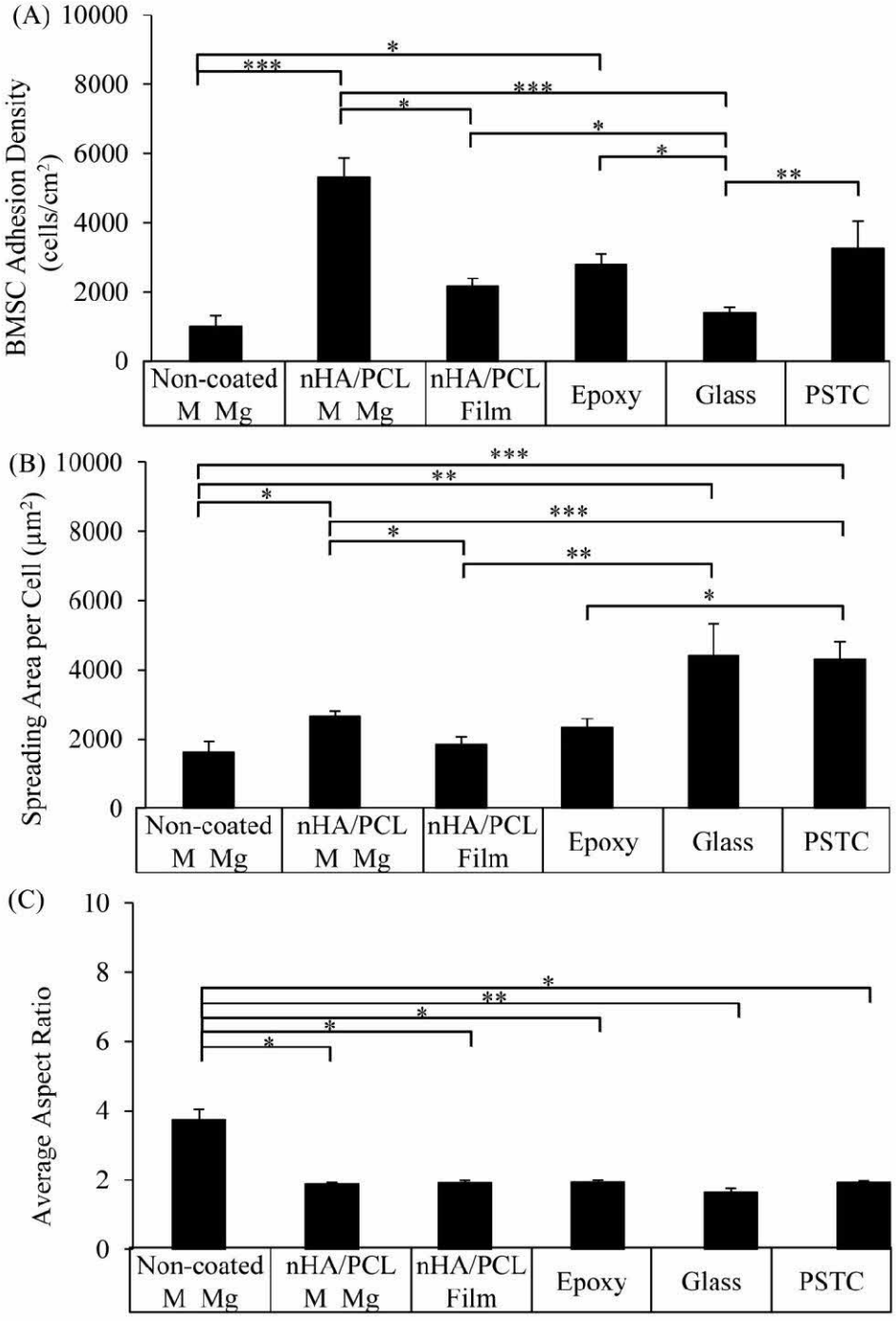

Figure 4.14: Quantitative analyses of BMSC adhesion and morphology using ImageJ. (A) Average BMSC adhesion density directly on the sample surface. (B) Average spreading area of BMSCs directly on the sample surface. (C) Average aspect ratio of BMSCs directly on the sample surface. Values are mean ± standard error; n=15. *$p < 0.05$, **$p < 0.01$, ***$p < 0.0001$.

4.4- Discussion

4.4.1- A Defined Model System for Studying the Key Parameters Affecting Nanocomposite Coatings on Magnesium

Nanocomposite coatings provide synergistic properties at the tissue-implant interface by decreasing the degradation rate of Mg alloys and improving cellular interactions; however, delamination remains a key challenge because it limits the functional lifetime of the coatings in mediating the degradation of Mg alloys [148]. The objective of this study was to optimize the nanocomposite coatings to address the challenge and to elucidate the engineering guidelines for improving the nanocomposite coatings on Mg substrates for skeletal implant applications. The key parameters, *i.e.*, Mg substrate surface conditions (M_Mg versus A_Mg), the polymer component type in the nanocomposite coatings (PLGA, PLLA versus PCL), and the post-deposition processing (melting, annealing, the combination of the two versus none), were investigated to determine their effects on the sample degradation, coating adhesion strength, and BMSC responses. For this purpose, a model system based on spin coating was established and used for the systemic study of the key parameters that affect nanocomposite coatings on Mg substrates.

The spin coating process was revised based on our previous investigation in order to provide a more accurate model system for characterizing the material properties of nanocomposite coatings on Mg substrates. In our previous study, the substrates were spin coated on both faces and the edges of the substrates were dip coated; as a result, the edge had greater coating thickness than substrate faces, which promoted delamination because

internal stress is concentrated at edges and thicker coatings are more likely to delaminate [149]. Furthermore, the boundary regions between the spin and dip coatings may have created additional internal stress, and delamination often initiated at the edges of the samples and then propagated inwards, which damaged the coating-substrate interface within 8 hours of immersion [148]. The rapid delamination caused by the combination of spin and dip coatings made it difficult to characterize how the key parameters of material and surface affect the performance of the nanocomposite coated Mg substrates. Therefore, the model coating system was modified by mounting the Mg substrates in epoxy so that only one surface of a Mg substrate would be exposed and coated with the nanocomposites, which eliminated the edge effects and other irrelevant factors from the key material parameters of interest. It is worth mentioning that the spin coating process serves as a well-defined model system for studying the coating materials and their interactions with the substrates, but other coating methods for conformal coatings on three-dimensional skeletal implants are still needed for clinical translation.

4.4.2- The Polymer Component in the Nanocomposite Coatings Influenced the Coating Permeability and Interface with the Mg Substrate

Permeability was one of the key differences among the polymer components (PLGA, PLLA, or PCL) in the nanocomposite coatings. PCL had the lowest water diffusion coefficient among the three polymers, and PCL and PLLA had much less water absorption than PLGA. Table 4.4 lists a summary of relevant properties of PLGA, PLA, and PCL [150-155]. The slow water transport through PCL is one of the reasons that the

nHA/PCL coatings reduced Mg degradation more effectively than the nHA/PLGA and nHA/PLLA coatings.

Table 4.4: The properties of each polymer type used in the nanocomposite coatings on the Mg substrates. The polymer properties play important roles on the properties of the nanocomposite coatings on Mg substrates. The first values for thermal expansion coefficient that are denoted with a "#" occur below the T_g, while the second values occur above the T_g. PCL has such a low T_g that only the thermal expansion coefficient above the T_g was given. Values with an asterisk* are the median values based on the data found on the Polymer Database (Polyinfo: http://polymer.nims.go.jp/index_en.html). The calculation of median values for each polymer type included different variations of that polymer.

Polymer	Tg (°C)	Tm (°C)	Thermal Expansion Coefficient (1/°K)	Elastic Modulus (MPa)	Ultimate Tensile Strength (MPa)	Elongation at Break (%)	Water Absorption (wt %)	Water Diffusion Coefficient (cm^2/s)
Reference	[79*]	[79*]	[79*, 83]	[79*]	[79*]	[79*]	[79*, 84]	[80, 81, 82]
PLGA	48	N/A	$2.14x10^{-4}$ #/ 0.134	431	17	3.6	20	$8.49x10^{-9}$
PLA	57	163	$1.08x10^{-4}$ #/ $2.12x10^{-2}$	4614	60.6	4.4	0.27	$1.17x10^{-8}$
PCL	-62	55	$7x10^{-4}$	245	12.3	336	0.32	$9.11x10^{-10}$

Another key difference among the polymer components studied in the nanocomposite coatings is their viscosity. The nHA/PCL suspension had a lower viscosity than the nHA/PLGA or nHA/PLLA suspensions when the nHA/polymer weight ratio (30/70) and the nanocomposite/solvent ratio (10 wt./vol. %) were fixed. This required slower spin coating speeds for the nHA/PCL suspensions than the nHA/PLGA and nHA/PLLA suspensions to achieve the same coating thickness. The combination of lower viscosity and slower spin-coating speed enabled the nHA/PCL suspension to fill in the grinding grooves on M_Mg substrates better than nHA/PLGA and nHA/PLLA suspensions that had higher viscosity and faster spin-coating speed. Filling in the grinding grooves with the nanocomposite suspension increased the adhesion strength of

the nHA/PCL coatings due to improved physical interlocking. The nanocomposite suspensions solidified in less than 1 minute during spin coating, which limited the time for more viscous suspensions to flow into the grinding grooves. If the grinding grooves were not filled with the nanocomposite suspension due to the higher viscosity or faster spin-coating speed (in the cases of nHA/PLGA and nHA/PLLA suspensions), there would be less physical interlocking and the possible micro-spaces at the coating-substrate interface would act as reservoirs for water to promote degradation of Mg substrates.

4.4.3- The Post-Deposition Processing and Substrate Surface Conditions Influenced the Coating Permeability

The melting treatment for the nHA/PCL coatings reduced their permeability because the melted PCL was able to flow and seal residual voids in the coating or at the interface, while the annealing treatment for the nHA/PCL coatings reduced their permeability due to the increase of PCL crystallinity [156]. In contrast, the effects of melting and annealing treatments on the nHA/PLGA and nHA/PLLA coatings were dependent on both the polymer component type in the nanocomposite coatings and the substrate surface conditions. Specifically, on the A_Mg substrates, the post-deposition processing of melting then annealing for the nHA/PLGA and nHA/PLLA coatings reduced the sample corrosion rates; however, on the M_Mg substrates, the same post-deposition processing increased the sample corrosion rates, when compared with no post-deposition processing (Figure 4.5). This indicated that the effects of the post-deposition processing on the sample corrosion were more than just altering the coating permeability, because similar melting and annealing treatments reduced the permeability of PLGA

[137] and PLLA [157] films. It is speculated that the post-deposition processing might have affected the coating-substrate interface as well.

The interaction plots in Figure 4.6 indicated that the three key parameters (the polymer component in the nanocomposite coatings, the post-deposition processing, and the substrate surface conditions) interacted with one another; i.e., one parameter could increase or decrease the corrosion rates depending on the other parameters. The substrate surface condition alone did not have any statistically significant effect on the corrosion rates of the samples without coatings (t-test, p value = 0.24, Figure 4.5), but the substrate surface did have statistically significant effect on the corrosion of the samples with coatings (factorial ANOVA, p value = 5.83×10^{-7}, Figure 4.6). This suggested that the substrate surface conditions (A_Mg versus M_Mg) did not have any significant direct impact on the corrosion of Mg substrates, but instead indirectly affected the corrosion of Mg substrates by influencing the permeability of the coatings and the coating-substrate interface.

The alkaline heat treatment enriched the Mg substrate surfaces (A_Mg) with $Mg(OH)_2$ [21], which is a known nucleating agent for polymers [131-134]. The abundance of nucleating agents increased the number of polymer crystals formed on the surface and decreased the grain size, which correspondingly reduced the permeability of the polymer matrix. The smaller crystals also reduced the crack propagation in the polymer matrix in comparison with the larger crystals [158], which further increased the durability and protectiveness of the coatings. Furthermore, increased nucleation of polymer crystals directly on the Mg substrates could increase the interfacial strength

between the coating and substrate due to more sites of interactions [159].The abundance of nucleating agents on the A_Mg substrate surfaces was especially beneficial for the nHA/polymer coatings with the post-deposition processing.

4.4.4- Interactions among the Key Parameters and their Effects on Internal Stress and Corrosion

Figure 4.15 illustrates the interactions among the key parameters (polymer component in the nanocomposite coatings, substrate surface, post-deposition processing) and their effects on the sample performance, e.g., corrosion. The mechanical properties of the polymer components in the nanocomposite coatings, the post-deposition processing, and the substrate surface conditions affected the internal stress in the coatings. One of the most common sources of internal stress in coatings is shrinkage after deposition. Polymers generally expand when they undergo solid-liquid phase transition, and shrink when they solidify after deposition. The polymers in coatings are constrained by the substrate surface when they solidify, which creates internal stress. The volume changes of material during solidification and crystallization were reported to induce internal stresses in the range of 10-30 MPa [160, 161], which is significant as compared with the coating adhesion strengths. Internal stresses increase sharply at the edges and discontinuities, which explains why the coating delamination often initiates from the edges [149]. The stress could also accelerate the degradation of polymers [162] and reduce the adhesion strength of coatings [163]. Internal stress could cause the crack propagation in the coatings, which impairs the barrier properties of the coatings. Swelling is another source for internal stress. Polymers could swell as they absorb water, and the coatings have a

limited ability to accommodate this volume change due to the substrate constrain; for the same reason, the coatings also have a limited ability to accommodate shrinkage.

Interactions Among Polymer Component, Post-Deposition Processing, and Substrate Surface Influenced the Sample Performance

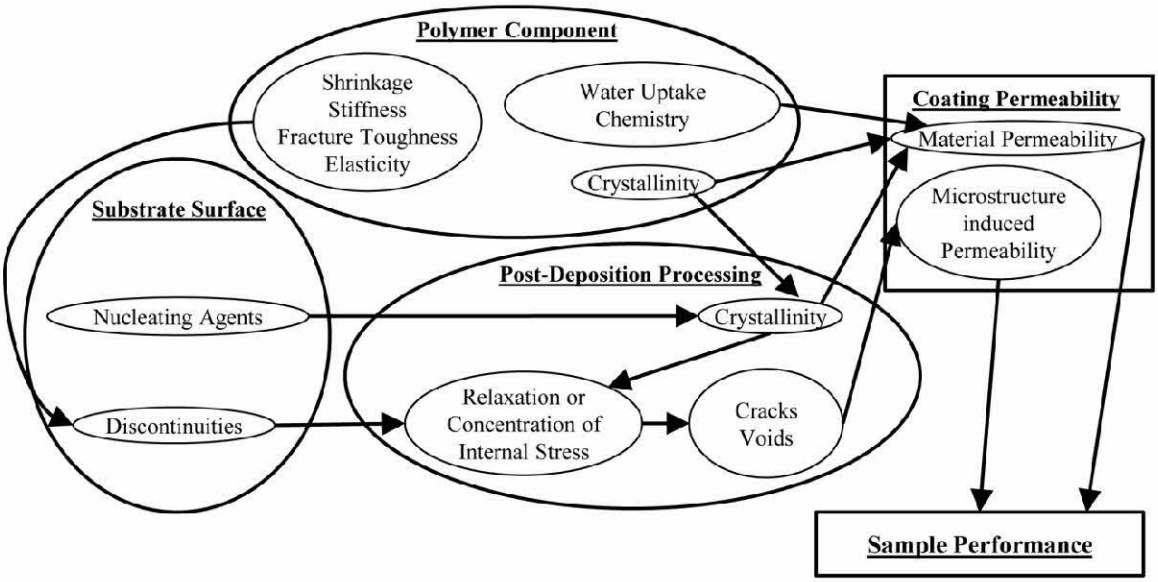

Figure 4.15: Interactions among the key parameters (polymer component in the nanocomposite coatings, substrate surface, post-deposition processing) and their effects on the sample performance. These interactions affected the permeability of the coatings and interfacial properties, and thus the overall sample performance.

As described in the equation 4.2, the residual stress (internal stress locked in the material) could emerge from the deposition of dissolved coating polymers (Eq. 4.2A) [164], deposition of melted coating polymers (Eq. 4.2B) [164], and/or hygroscopic swelling of the coating polymers (Eq. 4.2C) [165], all of which share striking similarities with one another. Specifically, the residual stress is directly proportional to the two key parameters, i.e., the elastic modulus and the volume change of the coating material, as shown in Eq. 4.2 A, B, and C. According to the elastic moduli listed in Table 4.4, PLA has the highest stiffness, PCL has the lowest stiffness, and PLGA is in between PLA and

PCL; thus, the stiffer PLA has greater internal stress from the parameter of elastic modulus. It is also important to know that minimizing the volume changes of the coating materials could significantly reduce the internal stress. For example, reducing the glass transition temperature (T_g) of the polymer can minimize the shrinkage originated from depositing dissolved polymers. This is because the difference in the volume fraction of the solvent (ϕ_s-ϕ_r) is reduced in the coating, as ϕ_s is delayed to the later stages of the drying process when there is less solvent [164, 166]. According to Table 4.4, PCL has lower T_g and thus has less internal stress generated by shrinkage. For depositing melted polymers on Mg substrates, using a polymer that has a lower thermal expansion coefficient (i.e., reducing $\Delta\alpha$) and allows a lower processing temperature (i.e., reducing ΔT) can minimize the shrinkage. The internal stress is generally lower for the polymer coatings annealed or cured at the lower temperatures than at the higher temperatures [167]. The parameters describing volume change in Eq. 4.2C are dependent on water uptake (i.e., water absorption) and relative humidity. The polymers with greater water uptake such as PLGA (Table 4.4) have higher internal stress according to Eq. 4.2C. Collectively, the polymers with lower elastic modulus, lower T_g, lower thermal expansion coefficient, and less water uptake will have less internal stress. For these reasons, the nHA/PCL coatings had less internal stress than the nHA/PLGA and nHA/PLLA coatings.

Eq. 4.2

$$\sigma = \frac{E}{1-\nu}\frac{\phi_s - \phi_r}{3} = \frac{E\Delta\alpha\Delta T}{1-\nu} = \frac{E\ \propto_f^h}{1-\nu}\Delta RH$$

Shrinkage after Deposition		
(A) Dissolved Coating Polymers	(B) Melted Coating Polymers	(C) Hygroscopic Swelling of Coating Polymers

σ = Residual Stress υ = Poisson Ratio E = Elastic Modulus

ϕ_s = Volume fraction of solvent at solidification point

ϕ_r = Volume fraction of solvent in dry coating

$\Delta\alpha$ = Difference in thermal expansion coefficients between coating and substrate

ΔT = Difference between processing and operating temperatures

α_f^h = Function derived from the ratio of water uptake volume and polymer volume

ΔRH = Change in relative humidity

The substrate surface affected the distribution of internal stress in the coatings. The grinding grooves on the M_Mg substrates came from 600 grit SiC paper that had a feature size of 15 μm, similar to the size range of the crystals formed in the polymers studied in the nanocomposite coatings. The surface groves acted as discontinuities in the coatings [168], and internal stress rises sharply at edges and discontinuities[149]. The abundance of discontinuities on the M_Mg surfaces required significant accommodation from the polymer component of the coatings after deposition and post-deposition

processing. The more elastic PCL were able to compensate the discontinuities better than PLLA and PLGA. Furthermore, the coating material may have been pulled out of the grinding grooves during the polymer shrinkage since the coating could only shrink perpendicular to the plane of the substrate. Polymer crystals may also have grown larger than the width of the grinding grooves during post-deposition processing and been physically excluded, as illustrated in Figure 4.16A. PLLA is amorphous after spin-coating because the solidification occurred much faster than the crystallization [89], but annealing could induce the formation of crystals larger than 15 μm [168]; which explains why annealing nHA/PLLA coatings on M_Mg increased the corrosion rates (Figure 4.5). In contrast, PCL is semi-crystalline after spin-coating [89], and annealing led to the formation of crystals smaller than those in PLLA **[169]**; which explains why annealing nHA/PCL coatings on M_Mg reduced the corrosion rates (Figure 4.5). Additionally, the smaller crystals restricted crack propagation more effectively than the larger crystals **[158]**. PLGA is an amorphous polymer, and annealing nHA/PLGA coatings on M_Mg increased the corrosion rates (Figure 4.5). After alkaline heat treatment, hydroxides filled the grinding grooves and reduced their sharp edges, which reduced the concentration of internal stress, as illustrated in Figure 4.16B. The abundant nucleating agents on A_Mg surfaces might have also reduced crystal growth and prevented the coating material from being pulled out of the grooves as the polymer shrinks. These are the possible reasons why the alkaline heat treatment of the Mg substrates reduced the corrosion rates of some nanocomposite-coated samples (Figure 4.5).

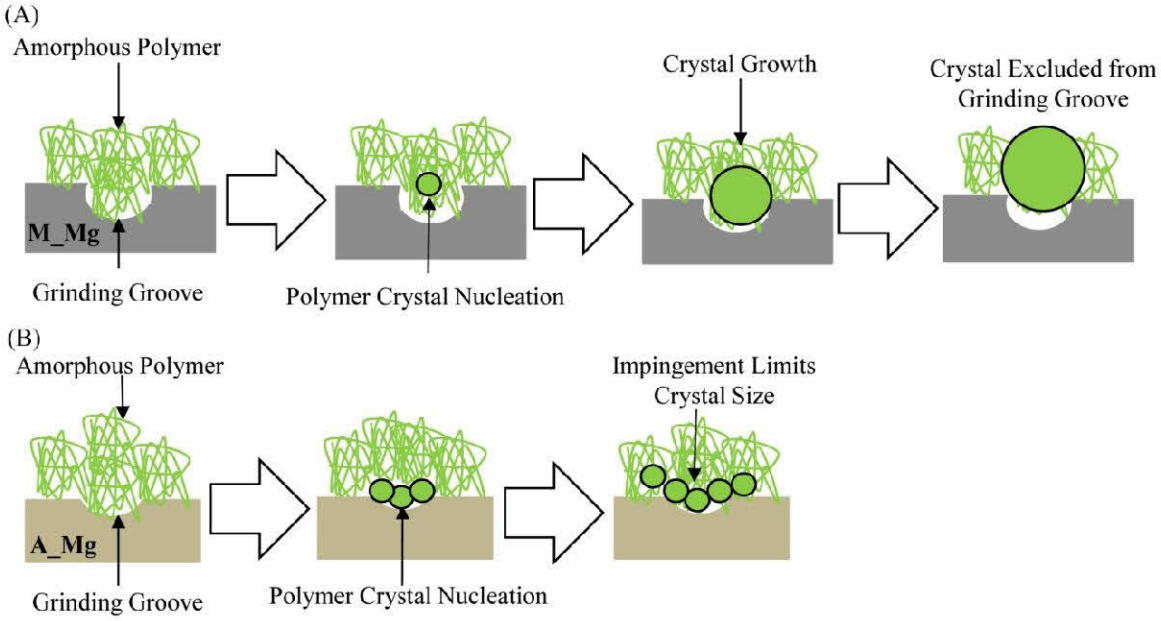

Figure 4.16: (A) The grinding grooves on the M_Mg substrate surfaces negatively interacted with PLGA and PLLA during post-deposition processing. The larger size of individual crystal led to physical exclusion from the grinding grooves. (B) The A_Mg substrate surfaces had less steep slopes along the grinding groves and had abundant nucleating agents. Impingement of the crystals limited their size and prevented their physical exclusion from the grinding grooves.

4.4.5- The Key Parameters Affecting the Coating Integrity and Adhesion Strength before and after Immersion Degradation

The immersion degradation study was performed to complement the PDP measurements of corrosion, because the immersion study takes into account how gas evolution and long-term exposure to body fluids would affect the coating properties and sample degradation.

The nanocomposite coatings maintained their structural integrity and adhesion throughout the 7-day immersion study (Figure 4.7). This is a significant progress considering the rapid onset of coating delamination from Mg substrates in the published

literature [170, 171] and our previous results [148]. The microstructure of all the nanocomposite coatings was thoroughly examined using SEM (Figure 4.9) and showed that the coatings remained intact after 7 days of immersion, except that the nHA/PLGA coated A_Mg showed the cracks and holes and exposed the underlying substrate (Figure 4.9 and 4.10). Notably, the edges around the holes on the the nHA/PLGA coated A_Mg (Figure 4.10) still attached to the Mg substrate, indicating good coating adhesion. The cracks and holes were only found in the nHA/PLGA coated A_Mg sample, possibly because PLGA had the highest permeability that increased Mg degradation, and the highest water absorption and hygroscopic swelling that increased internal stress in the coating (Table 4.4). The holes only formed on the A_Mg substrates because they were less stable than the M_Mg substrates at later immersion time points, as shown by the higher pH and [Mg^{2+}] of the non-coated A_Mg substrates (Figure 4.8).

The polymer component of the nanocomposite coatings and Mg substrate surface conditions had significant effects on the coating adhesion strength, especially after immersion (Figure 4.12). The nHA/PCL coatings had the greatest average adhesion strength before and after immersion. In contrast, other published results showed that pure PLLA coating had stronger adhesion to Mg than pure PCL coating [89]. The presence of dispersed nHA in the polymer matrix in this study might have contributed to this difference. Before immersion, the nHA/PCL coatings on the M_Mg had slightly greater average adhesion strength than on the A_Mg substrates, possibly because the nHA/PCL coating physically interlocked with the grinding grooves that were deeper in the M_Mg than in the A_Mg substrates. After 7 days of immersion in rSBF, the nHA/PCL coatings

on the M_Mg substrates retained their average adhesion strength significantly more than the nHA/PLGA and nHA/PLLA coatings did. After immersion, the nHA/PCL coatings also retained their average adhesion strength significantly more on the M_Mg than on the A_Mg substrates, possibly because the M_Mg substrate surface was less susceptible to aggressive ions at later immersion time points.

4.4.6- The Most Effective Nanocomposite Coatings in Reducing Degradation and Improving BMSC Adhesion

Overall, the nHA/PCL coatings on the M_Mg substrates with the post-deposition processing of melted then annealed provided the best combination in reducing sample degradation and improving BMSC adhesion. Specifically, the nHA/PCL coatings on the M_Mg substrates showed the least release of Mg^{2+} ions and the least pH increase during immersion degradation, and the highest average adhesion strength before and after immersion. This is most likely because PCL had a combination of desirable mechanical, thermal, and transport properties that minimized internal stress and water permeability when compared with the other polymers studied, as illustrated in Figure 4.17. Generally, the coating materials should have low elastic modulus, high fracture toughness, low T_g, low thermal expansion coefficient, low water uptake, and low water permeability to achieve the best outcome in reducing Mg substrate degradation. PLGA and PLLA had some of the desirable properties, but not an optimal integration of all. The nHA/PCL coatings on the M_Mg performed better than the same coatings on the A_Mg substrates because the combination of nHA/PCL coatings with the M_Mg substrates provided desirable physically interlocking between the coatings and the grinding grooves of the

substrates, and became less susceptible to degradation at later time points of immersion. Although the nHA/PLGA and nHA/PLLA coatings were not the optimal, they still significantly reduced the degradation of their Mg substrates.

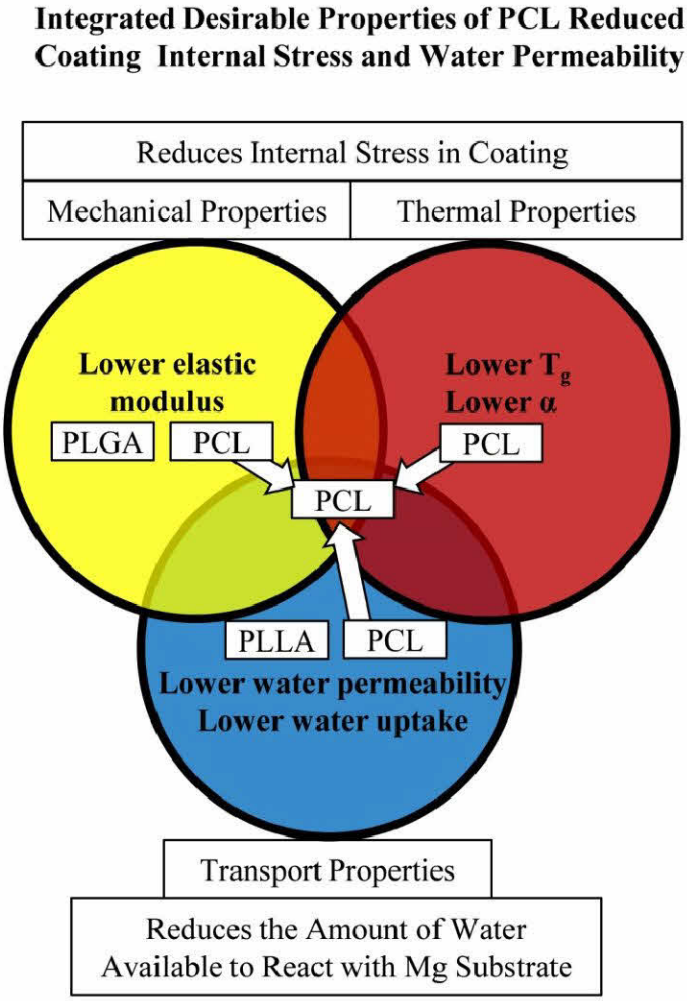

Figure 4.17: Comparison of the mechanical, thermal, and transport properties of the polymer components used in the nanocomposite coatings. PCL reduced Mg degradation more effectively than PLGA and PLLA because its lower elastic modulus, glass transition temperature (T_g), and thermal expansion coefficient (α) minimized internal stress; while its lower water permeability and uptake reduced the amount of water available for Mg degradation reactions.

The nHA/PCL coated M_Mg was selected for the cytocompatibility study in BMSC culture because it showed promising results in immersion degradation and coating adhesion testing. The nHA/PCL coated M_Mg showed the highest BMSC adhesion density among all the samples tested (Figure 4.13, 4.14A), most likely because the synergy between Mg^{2+} and nHA was beneficial for bone cell adhesion. It has been known that both Mg^{2+} and nHA could increase bone cell adhesion [19, 172-174]. The non-coated Mg showed lower BMSC adhesion density and less spreading area per cell than the nHA/PCL coated Mg (Figure 4.14A and 4.14B) because of the higher pH and unstable surface conditions caused by rapid degradation. The nHA/PCL films also showed lower BMSC adhesion density and less spreading area per cell than the nHA/PCL coated Mg, possibly due to the lack of Mg^{2+}. The epoxy and PSTC controls showed similar BMSC adhesion densities (Figure 4.14A), indicating the epoxy mounts for the Mg substrates did not have significant effects on BMSC adhesion. Interestingly, the aspect ratios of BMSCs on the non-coated M_Mg (~4) were significantly higher than the BMSCs on all the other sample types (~2) (Figure 4.14C), possibly because the M_Mg had a surface feature size of around 15 μm (similar to the size range of BMSCs) from grinding with 600 grit SiC paper. It has been reported that supplementing the cell culture media with Mg^{2+} ions did not significantly affect the cell aspect ratio (~2), and non-coated pure Mg and Mg-Zn-Ca alloys did not significantly alter the cell aspect ratio either (~2) when they were polished with 0.25 μm diamond paste [175]. The difference in surface feature size due to polishing might be the reason for the observed difference in the aspect ratio of BMSCs.

4.4.5- Conclusions of Chapter 4

The results of this study demonstrated that the nanocomposite coatings could provide dual functions of controlling Mg degradation and improving bone cell responses simultaneously, both important for clinical translation of Mg-based biomaterials. The nHA/polymer nanocomposite coatings significantly reduced the degradation of Mg substrates during immersion in rSBF. Optimization of the key parameters (i.e., substrate surface conditions, polymer component types in the nanocomposite coatings, and the post-deposition processing) further improved the sample performance, i.e., slower degradation and better BMSC adhesion. The nHA/PCL coated M_Mg with the post-deposition processing of melting then annealing provided the best overall results in decreasing Mg degradation and improving BMSC adhesion density, due to reduced internal stress and water permeability. Post-deposition processing could improve or impair the barrier properties of the nanocomposite coatings depending upon the properties of the polymer component in the nanocomposites and the substrate surface conditions, suggesting these key parameters should be considered collectively rather than separately due to their interactions. This systemic investigation of nanocomposite coatings on Mg substrates provided valuable design guidelines for polymeric and nanocomposite coatings on Mg-based substrates for potential skeletal implant applications.

Chapter 5- Major Conclusions and Proposals for Future Research

5.1- The Promise of Mg Alloys for Bone Implant Applications

Mg alloys have great potential as biodegradable implant materials because of their unique combination of mechanical and biological properties, but historically they have degraded too rapidly for many clinical applications. Modern advancements in material science offer solutions to this rapid degradation. Mg degradation can be controlled through alloy composition and processing, surface modifications, coatings, and combinations thereof. These methods of controlling degradation can make Mg bone implants clinically equivalent to similar Ti bone implants for some applications [2]. In an ideal case the degradation rate of Mg alloy bone implants will match the growth rate of bone tissue, so that the Mg implants will be replaced with natural bone tissue as they degrade. This ideal outcome will most likely require a combination of methods to control the degradation and improve the osteoconductivity of the implant. The nHA/polymer nanocomposite coatings developed in this investigation have the potential to be part of the solution to rapid Mg degradation because they can perform multiple functions simultaneously, and can be combined with other methods of degradation control like alloy composition or surface modification.

5.2- Design Criteria for Nanocomposite Coatings on Mg Alloys

Nanocomposite coatings for Mg alloys should be designed for reduced permeability and internal stress; which will improve the barrier properties of coatings and extend their functional lifetime.

1. Reducing the permeability of coatings will limit Mg surface instability from degradation reactions with water, and limit the amount of H_2 gas evolved. This can be achieved by using materials with low permeability and water uptake, or by using coating deposition and processing routes that seal structural flaws in the coating and increase the crystallinity of the coating.
2. Reducing internal stress will prevent crack propagation and delamination of coatings. Internal stress can be reduced by using coatings with uniform structure, low thickness, low elastic modulus, low thermal expansion coefficient, low T_g, and high elasticity. Some post-deposition processing routes can also relieve internal stress.

5.3- Summary of Major Conclusions

This investigation provided valuable insight concerning the development and characterization of nanocomposite coatings for Mg alloy biomaterials for bone implant applications. The degradation of Mg alloys in physiologically relevant environments was determined to be the result of multiple interacting factors. A set of Mg alloy parameters that reduces degradation under specific environmental conditions can also accelerate degradation under different environmental conditions. This knowledge is crucial for

designing Mg alloy implants because different regions of the body frequently have different environmental conditions.

The next stage of this investigation developed nHA/polymer nanocomposite coatings that controlled Mg alloy degradation in a simulated *in vivo* environment, discovered engineering challenges to those coatings, and then addressed those challenges. It was demonstrated that coating delamination can be promoted by the reactivity of the Mg substrates, but can be resolved through engineering controls. Finally, the nanocomposite coatings significantly improved bone cell adhesion to the Mg substrates in addition to controlling their degradation, which is critical to the function of Mg-based bone implants.

5.4- Future Research

Spin coating processes can only coat planar substrates, and many biomedical implants have complex three dimensional shapes. The next stage of this research should use a different coating deposition process to coat substrates that have complex three dimensional shapes identical to biodegradable bone implants (*e.g.* screws). Furthermore, the drug release capability of the nanocomposite coatings should be investigated so that the bioactivity and antimicrobial properties of the coatings can be improved.

References

[1] Castellani C, Lindtner R A, Hausbrandt P, Tschegg E, Stanzl-Tschegg S E, Zanoni G, Beck S and Weinberg A M 2011 Bone-implant interface strength and osseointegration: Biodegradable magnesium alloy versus standard titanium control *Acta Biomater* **7** 432-40

[2] Windhagen H, Radtke K, Weizbauer A, Diekmann J, Noll Y, Kreimeyer U, Schavan R, Stukenborg-Colsman C and Waizy H 2013 Biodegradable magnesium-based screw clinically equivalent to titanium screw in hallux valgus surgery: short term results of the first prospective, randomized, controlled clinical pilot study *Biomed Eng Online* **12** 62

[3] Minkowitz R B, Bhadsavle S, Walsh M and Egol K A 2007 Removal of painful orthopaedic implants after fracture union *J Bone Joint Surg Am* **89A** 1906-12

[4] DiCarlo E F and Bullough P G 1992 The biologic responses to orthopedic implants and their wear debris *Clinical Materials* **9** 235-60

[5] Purdue P E, Koulouvaris P, Nestor B J and Sculco T P 2006 The central role of wear debris in periprosthetic osteolysis *HSS J* **2** 102-13

[6] Jiang Y, Jia T, Wooley P H and Yang S Y 2013 Current research in the pathogenesis of aseptic implant loosening associated with particulate wear debris *Acta Orthop Belg* **79** 1-9

[7] Jain K K 2012 *The handbook of nanomedicine* (New York: Springer)

[8] Mavrogenis A F, Dimitriou R, Parvizi J and Babis G C 2009 Biology of implant osseointegration *J Musculoskel Neuron* **9** 61-71

[9] Brady R A, Calhoun J H, Leid J G and Shirtliff M E 2009 *The Role of Biofilms in Device-Related Infections*: Springer) pp 15-55

[10] Osmon D R, Berbari E F, Berendt A R, Lew D, Zimmerli W, Steckelberg J M, Rao N, Hanssen A and Wilson W R 2012 Diagnosis and management of prosthetic joint infection: clinical practice guidelines by the Infectious Diseases Society of America *Clinical Infectious Diseases* cis803

[11] Darouiche R O 2004 Current concepts - Treatment of infections associated with surgical implants *New Engl J Med* **350** 1422-9

[12] Kirchhoff C, Braunstein V, Kirchhoff S, Sprecher C M, Ockert B, Fischer F, Leidel B A and Biberthaler P 2008 Outcome analysis following removal of locking plate fixation of the proximal humerus *Bmc Musculoskel Dis* **9**

[13] Hanson B, van der Werken C and Stengel D 2008 Surgeons' beliefs and perceptions about removal of orthopaedic implants *Bmc Musculoskel Dis* **9**

[14] Staiger M P, Pietak A M, Huadmai J and Dias G 2006 Magnesium and its alloys as orthopedic biomaterials: A review *Biomaterials* **27** 1728-34

[15] Brar H S, Platt M O, Sarntinoranont M, Martin P I and Manuel M V 2009 Magnesium as a biodegradable and bioabsorbable material for medical implants *Jom-Us* **61** 31-4

[16] Zhang Y, Ren L, Li M, Lin X, Zhao H F and Yang K 2012 Preliminary Study on Cytotoxic Effect of Biodegradation of Magnesium on Cancer Cells *J Mater Sci Technol* **28** 769-72

[17] Zhai Z, Qu X, Li H, Yang K, Wan P, Tan L, Ouyang Z, Liu X, Tian B, Xiao F, Wang W, Jiang C, Tang T, Fan Q, Qin A and Dai K 2014 The effect of metallic magnesium degradation products on osteoclast-induced osteolysis and attenuation of NF-kappaB and NFATc1 signaling *Biomaterials* **35** 6299-310

[18] Zhang E, Xu L, Yu G, Pan F and Yang K 2009 In vivo evaluation of biodegradable magnesium alloy bone implant in the first 6 months implantation *J Biomed Mater Res A* **90** 882-93

[19] Park J-W, Kim Y-J, Jang J-H and Song H 2010 Osteoblast response to magnesium ion-incorporated nanoporous titanium oxide surfaces *Clinical Oral Implants Research* **21** 1278-87

[20] Castellani C, Lindtner R A, Hausbrandt P, Tschegg E, Stanzl-Tschegg S E, Zanoni G, Beck S and Weinberg A-M 2011 Bone–implant interface strength and osseointegration: Biodegradable magnesium alloy versus standard titanium control *Acta Biomater* **7** 432-40

[21] Guan R G, Johnson I, Cui T, Zhao T, Zhao Z Y, Li X and Liu H 2012 Electrodeposition of hydroxyapatite coating on Mg-4.0Zn-1.0Ca-0.6Zr alloy and in vitro evaluation of degradation, hemolysis, and cytotoxicity *J Biomed Mater Res A* **100** 999-1015

[22] Witte F 2010 The history of biodegradable magnesium implants: A review *Acta Biomater* **6** 1680-92

[23] Reifenrath J, Angrisani N, Erdmann N, Lucas A, Waizy H, Seitz J M, Bondarenko A and Meyer-Lindenberg A 2013 Degrading magnesium screws ZEK100: biomechanical testing, degradation analysis and soft-tissue biocompatibility in a rabbit model *Biomed Mater* **8**

[24] Witte F 2010 The history of biodegradable magnesium implants: a review *Acta Biomater* **6** 1680-92

[25] Johnson I, Akari K and Liu H 2013 Nanostructured hydroxyapatite/poly(lactic-co-glycolic acid) composite coating for controlling magnesium degradation in simulated body fluid *Nanotechnology* **24** 375103

[26] Song G L 2005 Recent progress in corrosion and protection of magnesium alloys *Adv Eng Mater* **7** 563-86

[27] de Mele M F L, Mueller W D, Nascimento M L and Zeddies M 2009 Degradation of magnesium and its alloys: Dependence on the composition of the synthetic biological media *J Biomed Mater Res A* **90A** 487-95

[28] Lindstrom R, Johansson L G, Thompson G E, Skeldon P and Svensson J E 2004 Corrosion of magnesium in humid air *Corros Sci* **46** 1141-58

[29] Heakal F E T, Fekry A M and Fatayerji M Z 2009 Influence of halides on the dissolution and passivation behavior of AZ91D magnesium alloy in aqueous solutions *Electrochim Acta* **54** 1545-57

[30] Ferrando W A 1989 Review of Corrosion and Corrosion Control of Magnesium Alloys and Composites *J Mater Eng* **11** 299-313

[31] Song G, Atrens A, St John D, Wu X and Nairn J 1997 The anodic dissolution of magnesium in chloride and sulphate solutions *Corrosion Science* **39** 1981-2004

[32] Ghali E, Dietzel W and Kainer K U 2004 General and localized corrosion of magnesium alloys: A critical review *J Mater Eng Perform* **13** 7-23

[33] Song G and Atrens A 2003 Understanding magnesium corrosion - A framework for improved alloy performance *Advanced Engineering Materials* 837-58

[34] Virtanen S and Rettig R 2009 Composition of corrosion layers on a magnesium rare-earth alloy in simulated body fluids *Journal of Biomedical Materials Research Part A* **88A** 359-69

[35] Chu P K, Xin Y C, Huo K F, Tao H and Tang G Y 2008 Influence of aggressive ions on the degradation behavior of biomedical magnesium alloy in physiological environment *Acta Biomater* **4** 2008-15

[36] Erdmann N, Angrisani N, Reifenrath J, Lucas A, Thorey F, Bormann D and Meyer-Lindenberg A 2011 Biomechanical testing and degradation analysis of MgCa0.8 alloy screws: A comparative in vivo study in rabbits *Acta Biomater* **7** 1421-8

[37] Witte F, Fischer J, Nellesen J, Crostack H A, Kaese V, Pisch A, Beckmann F and Windhagen H 2006 In vitro and in vivo corrosion measurements of magnesium alloys *Biomaterials* **27** 1013-8

[38] Mueller W D, Nascimento M L and de Mele M F L 2010 Critical discussion of the results from different corrosion studies of Mg and Mg alloys for biomaterial applications *Acta Biomater* **6** 1749-55

[39] Jensen J, Rolfing J H, Svend Le D Q, Kristiansen A A, Nygaard J V, Hokland L B, Bendtsen M, Kassem M, Lysdahl H and Bunger C E 2013 Surface-modified functionalized polycaprolactone scaffolds for bone repair: In vitro and in vivo experiments *J Biomed Mater Res A*

[40] Imwinkelried T, Beck S, Iizuka T and Schaller B 2013 Effect of a plasmaelectrolytic coating on the strength retention of in vivo and in vitro degraded magnesium implants *Acta Biomater* **9** 8643-9

[41] Hing K A, Wilson L E and Buckland T 2007 Comparative performance of three ceramic bone graft substitutes *Spine J* **7** 475-90

[42] Sung H J, Meredith C, Johnson C and Galis Z S 2004 The effect of scaffold degradation rate on three-dimensional cell growth and angiogenesis *Biomaterials* **25** 5735-42

[43] Dumas J E, Prieto E M, Zienkiewicz K J, Guda T, Wenke J C, Bible J, Holt G E and Guelcher S A 2014 Balancing the Rates of New Bone Formation and Polymer Degradation Enhances Healing of Weight-Bearing Allograft/Polyurethane Composites in Rabbit Femoral Defects *Tissue Eng Pt A* **20** 115-29

[44] Zhang S, Zhang X, Zhao C, Li J, Song Y, Xie C, Tao H, Zhang Y, He Y, Jiang Y and Bian Y 2010 Research on an Mg–Zn alloy as a degradable biomaterial *Acta Biomater* **6** 626-40

[45] Aghion E, Gueta Y, Moscovitch N and Bronfin B 2008 Effect of yttrium additions on the properties of grain-refined Mg-3%Nd alloy *J Mater Sci* **43** 4870-5

[46] Socjusz-Podosek M and Litynska L 2003 Effect of yttrium on structure and mechanical properties of Mg alloys *Mater Chem Phys* **80** 472-5

[47] Wu B L, Zhao Y H, Du X H, Zhang Y D, Wagner F and Esling C 2010 Ductility enhancement of extruded magnesium via yttrium addition *Mat Sci Eng a-Struct* **527** 4334-40

[48] Yao H B, Li Y and Wee A T S 2003 Passivity behavior of melt-spun Mg-Y alloys *Electrochimica Acta* **48** 4197-204

[49] Chen J, Li Q A, Li J H, Li X F, Li K J and Zhang X Y 2009 Microstructure and mechanical properties of Mg-6Al magnesium alloy with yttrium and neodymium elements *China Foundry* **6** 124-8

[50] Davenport A J, Padovani C, Connolly B J, Stevens N P C, Beale T A W, Groso A and Stampanoni M 2007 Synchrotron X-ray microtomography study of the role of Y in corrosion of magnesium alloy WE43 *Electrochem Solid St* **10** C5-C8

[51] Liu M, Schmutz P, Uggowitzer P J, Song G L and Atrens A 2010 The influence of yttrium (Y) on the corrosion of Mg-Y binary alloys *Corros Sci* **52** 3687-701

[52] Miller P L, Shaw B A, Wendt R G and Moshier W C 1995 Assessing the Corrosion-Resistance of Nonequilibrium Magnesium-Yttrium Alloys *Corrosion* **51** 922-31

[53] Johnson I, Perchy D and Liu H 2011 In vitro evaluation of the surface effects on magnesium-yttrium alloy degradation and mesenchymal stem cell adhesion *J Biomed Mater Res A*

[54] Uggowitzer P J, Hanzi A C, Gunde P and Schinhammer M 2009 On the biodegradation performance of an Mg-Y-RE alloy with various surface conditions in simulated body fluid *Acta Biomater* **5** 162-71

[55] Uggowitzer P J, Gunde P, Furrer A, Hanzi A C and Schmutz P 2010 The influence of heat treatment and plastic deformation on the bio-degradation of a Mg-Y-RE alloy *Journal of Biomedical Materials Research Part A* **92A** 409-18

[56] Zhang E L, He W W and Yang K 2010 Effect of Y on the bio-corrosion behavior of extruded Mg-Zn-Mn alloy in Hank's solution *Mat Sci Eng C-Mater* **30** 167-74

[57] Walter R, Kannan M B, He Y and Sandham A 2013 Effect of surface roughness on the in vitro degradation behaviour of a biodegradable magnesium-based alloy *Appl Surf Sci* **279** 343-8

[58] Walter R and Kannan M B 2011 Influence of surface roughness on the corrosion behaviour of magnesium alloy *Mater Design* **32** 2350-4

[59] Von Der Hoh N, Bormann D, Lucas A, Denkena B, Hackenbroich C and Meyer-Lindenberg A 2009 Influence of Different Surface Machining Treatments of Magnesium-based Resorbable Implants on the Degradation Behavior in Rabbits *Adv Eng Mater* **11** B47-B54

[60] Allen K W, Hatzinikolaou T and Armstrong K B 1984 A comparison of acrylic adhesives for bonding aluminum alloys after using various surface preparation methods *International Journal of Adhesion and Adhesives* **4** 133-6

[61] Molitor P, Barron V and Young T 2001 Surface treatment of titanium for adhesive bonding to polymer composites: a review *International Journal of Adhesion and Adhesives* **21** 129-36

[62] Suzuki K, Aoki K and Ohya K 1997 Effects of surface roughness of titanium implants on bone remodeling activity of femur in rabbits *Bone* **21** 507-14

[63] Abdal-hay A, Dewidar M and Lim J K 2012 Biocorrosion behavior and cell viability of adhesive polymer coated magnesium based alloys for medical implants *Appl Surf Sci* **261** 536-46

[64] Wong H M, Yeung K W K, Lam K O, Tam V, Chu P K, Luk K D K and Cheung K M C 2010 A biodegradable polymer-based coating to control the performance of magnesium alloy orthopaedic implants *Biomaterials* **31** 2084-96

[65] Lu P, Cao L, Liu Y, Xu X and Wu X 2011 Evaluation of magnesium ions release, biocorrosion, and hemocompatibility of MAO/PLLA-modified magnesium alloy WE42 *Journal of Biomedical Materials Research Part B: Applied Biomaterials* **96B** 101-9

[66] Jo J-H, Li Y, Kim S-M, Kim H-E and Koh Y-H 2012 Hydroxyapatite/poly (ε-caprolactone) double coating on magnesium for enhanced corrosion resistance and coating flexibility *J Biomater Appl* 0885328212468921

[67] Zhang S 2011 *Biological and Biomedical Coatings Handbook: Applications*: Taylor & Francis)

[68] LeGeros R Z 2002 Properties of Osteoconductive Biomaterials: Calcium Phosphates *Clin Orthop Relat R* **395** 81-98

[69] Geesink R G T 2002 Osteoconductive Coatings for Total Joint Arthroplasty *Clin Orthop Relat R* **395** 53-65

[70] Kuroda K and Okido M 2012 Hydroxyapatite coating of titanium implants using hydroprocessing and evaluation of their osteoconductivity *Bioinorganic chemistry and applications* **2012**

[71] Webster T J, Ergun C, Doremus R H, Siegel R W and Bizios R 2000 Enhanced functions of osteoblasts on nanophase ceramics *Biomaterials* **21** 1803-10

[72] Ergun C, Liu H N, Halloran J W and Webster T J 2007 Increased osteoblast adhesion on nanograined hydroxyapatite and tricalcium phosphate containing calcium titanate *J Biomed Mater Res A* **80A** 990-7

[73] Guan F, Ma S, Shi X, Ma X, Chi L, Liang S, Cui Y, Wang Z, Yao N, Guan S and Yang B 2014 Biocompatibility of nano-hydroxyapatite/Mg-Zn-Ca alloy composite scaffolds to human umbilical cord mesenchymal stem cells from Wharton's jelly in vitro *Sci China Life Sci* **57** 181-7

[74] Sonmez S, Aksakal B and Dikici B 2014 Influence of hydroxyapatite coating thickness and powder particle size on corrosion performance of MA8M magnesium alloy *J Alloy Compd* **596** 125-31

[75] Ye X Y, Cai S, Xu G H, Dou Y, Hu H T, Ye X J, Zhao H and Sun X H 2014 The Influence of Mesopores on the Corrosion Resistance of Hydroxyapatite Coated AZ31 Mg Alloy *J Electrochem Soc* **161** C145-C50

[76] Yang Y-C 2007 Influence of residual stress on bonding strength of the plasma-sprayed hydroxyapatite coating after the vacuum heat treatment *Surface and Coatings Technology* **201** 7187-93

[77] Duan Y H, Zhu S, Guo F, Zhu J Y, Li M, Ma J and Zhu Q S 2012 The effect of adhesive strength of hydroxyapatite coating on the stability of hydroxyapatite-coated prostheses in vivo at the early stage of implantation *Arch Med Sci* **8** 199-208

[78] Rojaee R, Fathi M and Raeissi K 2013 Controlling the degradation rate of AZ91 magnesium alloy via sol-gel derived nanostructured hydroxyapatite coating *Mat Sci Eng C-Mater* **33** 3817-25

[79] Yang J X, Cui F Z, Lee I S, Zhang Y, Yin Q S, Xia H and Yang S X 2012 In vivo biocompatibility and degradation behavior of Mg alloy coated by calcium phosphate in a rabbit model *J Biomater Appl* **27** 153-64

[80] Shadanbaz S, Walker J, Woodfield T B F, Staiger M P and Dias G J 2014 Monetite and brushite coated magnesium: in vivo and in vitro models for degradation analysis *J Mater Sci-Mater M* **25** 173-83

[81] Kim S M, Jo J H, Lee S M, Kang M H, Kim H E, Estrin Y, Lee J H, Lee J W and Koh Y H 2014 Hydroxyapatite-coated magnesium implants with improved in vitro and in vivo biocorrosion, biocompatibility, and bone response *J Biomed Mater Res A* **102** 429-41

[82] Ou C W, Lu W, Zhan Z L, Huang P, Yan P F, Yan B and Chen M S 2013 Effect of Ca and P Ion Concentrations on the Structural and Corrosion Properties of Biomimetic Ca-P Coatings on ZK60 Magnesium Alloy *Int J Electrochem Sc* **8** 9518-30

[83] Rojaee R, Fathi M and Raeissi K 2013 Electrophoretic deposition of nanostructured hydroxyapatite coating on AZ91 magnesium alloy implants with different surface treatments *Appl Surf Sci* **285, Part B** 664-73

[84] Qiu X, Wan P, Tan L L, Fan X M and Yang K 2014 Preliminary research on a novel bioactive silicon doped calcium phosphate coating on AZ31 magnesium alloy via electrodeposition *Mat Sci Eng C-Mater* **36** 65-76

[85] Wang B C, Chang E, Lee T M and Yang C Y 1995 Changes in Phases and Crystallinity of Plasma-Sprayed Hydroxyapatite Coatings under Heat-Treatment - a Quantitative Study *J Biomed Mater Res* **29** 1483-92

[86] Ostrowski N J, Lee B, Roy A, Ramanathan M and Kumta P N 2013 Biodegradable poly(lactide-co-glycolide) coatings on magnesium alloys for orthopedic applications *J Mater Sci-Mater M* **24** 85-96

[87] Li J N, Cao P, Zhang X N, Zhang S X and He Y H 2010 In vitro degradation and cell attachment of a PLGA coated biodegradable Mg-6Zn based alloy *J Mater Sci* **45** 6038-45

[88] Xu L and Yamamoto A 2012 In vitro degradation of biodegradable polymer-coated magnesium under cell culture condition *Appl Surf Sci* **258** 6353-8

[89] Xu L P and Yamamoto A 2012 Characteristics and cytocompatibility of biodegradable polymer film on magnesium by spin coating *Colloid Surface B* **93** 67-74

[90] Kannan M B and Liyanaarachchi S 2013 Hybrid coating on a magnesium alloy for minimizing the localized degradation for load-bearing biodegradable mini-implant applications *Mater Chem Phys*

[91] Abdal-hay A, Amna T and Lim J K 2013 Biocorrosion and osteoconductivity of PCL/nHAp composite porous film-based coating of magnesium alloy *Solid State Sci* **18** 131-40

[92] Wong K, Yeung K, Lam J, Chu P, Luk K and Cheung K 2009 Reduction of corrosion behavior of Magnesium alloy by PCL surface treatment p 22-5

[93] Woodruff M A and Hutmacher D W 2010 The return of a forgotten polymer—Polycaprolactone in the 21st century *Prog Polym Sci* **35** 1217-56

[94] Huang Y X, Ren J, Chen C, Ren T B and Zhou X Y 2008 Preparation and properties of poly(lactide-co-glycolide) (PLGA)/nano-hydroxyapatite (NHA) scaffolds by thermally induced phase separation and rabbit MSCs culture on scaffolds *J Biomater Appl* **22** 409-32

[95] Smith L J, Swaim J S, Yao C, Haberstroh K M, Nauman E A and Webster T J 2007 Increased osteoblast cell density on nanostructured PLGA-coated nanostructured titanium for orthopedic applications *Int J Nanomed* **2** 493-9

[96] You Y, Lee S W, Youk J H, Min B M, Lee S J and Park W H 2005 In vitro degradation behaviour of non-porous ultra-fine poly(glycolic acid)/poly(L-lactic acid) fibres and porous ultra-fine poly(glycolic acid) fibres *Polym Degrad Stabil* **90** 441-8

[97] Lu L, Peter S J, Lyman M D, Lai H L, Leite S M, Tamada J A, Uyama S, Vacanti J P, Langer R and Mikos A G 2000 In vitro and in vivo degradation of porous poly(DL-lactic-co-glycolic acid) foams *Biomaterials* **21** 1837-45

[98] Lee S J, Khang G, Lee Y M and Lee H B 2002 Interaction of human chondrocytes and NIH/3T3 fibroblasts on chloric acid-treated biodegradable polymer surfaces *J Biomater Sci Polym Ed* **13** 197-212

[99] Kanczler J M and Oreffo R O 2008 Osteogenesis and angiogenesis: the potential for engineering bone *Eur Cell Mater* **15** 100-14

[100] Bos R R, Rozema F R, Boering G, Nijenhuis A J, Pennings A J, Verwey A B, Nieuwenhuis P and Jansen H W 1991 Degradation of and tissue reaction to biodegradable poly(L-lactide) for use as internal fixation of fractures: a study in rats *Biomaterials* **12** 32-6

[101] Pihlajamaki H, Bostman O, Tynninen O and Laitinen O 2006 Long-term tissue response to bioabsorbable poly-L-lactide and metallic screws: an experimental study *Bone* **39** 932-7

[102] Walton M and Cotton N J 2007 Long-term in vivo degradation of poly-L-lactide (PLLA) in bone *J Biomater Appl* **21** 395-411

[103] Barber F A and Dockery W D 2006 Long-term absorption of poly-L-lactic acid interference screws *Arthroscopy-the Journal of Arthroscopic and Related Surgery* **22** 820-6

[104] Stahelin A C, Weiler A, Rufenacht H, Hoffmann R, Geissmann A and Feinstein R 1997 Clinical degradation and biocompatibility of different bioabsorbable interference screws: A report of six cases *Arthroscopy* **13** 238-44

[105] Liu H N and Webster T J 2010 Mechanical properties of dispersed ceramic nanoparticles in polymer composites for orthopedic applications *Int J Nanomed* **5** 299-313

[106] Liu H N and Webster T J 2011 Enhanced biological and mechanical properties of well-dispersed nanophase ceramics in polymer composites: From 2D to 3D printed structures *Mat Sci Eng C-Mater* **31** 77-89

[107] Wei G and Ma P X 2004 Structure and properties of nano-hydroxyapatite/polymer composite scaffolds for bone tissue engineering *Biomaterials* **25** 4749-57

[108] Ebrahimian-Hosseinabadi M, Ashrafizadeh F, Etemadifar M and Venkatraman S S 2011 Evaluating and Modeling the Mechanical Properties of the Prepared PLGA/nano-BCP Composite Scaffolds for Bone Tissue Engineering *J Mater Sci Technol* **27** 1105-12

[109] Lock J and Liu H N 2011 Nanomaterials enhance osteogenic differentiation of human mesenchymal stem cells similar to a short peptide of BMP-7 *Int J Nanomed* **6** 2769-77

[110] Lock J, Nguyen T Y and Liu H 2012 Nanophase hydroxyapatite and poly(lactide-co-glycolide) composites promote human mesenchymal stem cell adhesion and osteogenic differentiation in vitro *J Mater Sci Mater Med* **23** 2543-52

[111] Akagi H, Iwata M, Ichinohe T, Amimoto H, Hayashi Y, Kannno N, Ochi H, Fujita Y, Harada Y, Tagawa M and Hara Y 2013 Hydroxyapatite/poly-L-lactide acid screws have better biocompatibility and femoral burr hole closure than does poly-L-lactide acid alone *J Biomater Appl*

[112] Abdal-hay A, Barakat N A M and Lim J K 2013 Hydroxyapatite-doped poly(lactic acid) porous film coating for enhanced bioactivity and corrosion behavior of AZ31 Mg alloy for orthopedic applications *Ceram Int* **39** 183-95

[113] D'Anto V, Raucci M G, Guarino V, Martina S, Valletta R and Ambrosio L 2013 Behaviour of human mesenchymal stem cells on chemically synthesized HA-PCL scaffolds for hard tissue regeneration *J Tissue Eng Regen Med*

[114] Ngiam M, Liao S S, Patil A J, Cheng Z Y, Chan C K and Ramakrishna S 2009 The fabrication of nano-hydroxyapatite on PLGA and PLGA/collagen nanofibrous composite scaffolds and their effects in osteoblastic behavior for bone tissue engineering *Bone* **45** 4-16

[115] Hasegawa S, Ishii S, Tamura J, Furukawa T, Neo M, Matsusue Y, Shikinami Y, Okuno M and Nakamura T 2006 A 5-7 year in vivo study of high-strength hydroxyapatite/poly(L-lactide) composite rods for the internal fixation of bone fractures *Biomaterials* **27** 1327-32

[116] Shikinami Y, Matsusue Y and Nakamura T 2005 The complete process of bioresorption and bone replacement using devices made of forged composites of raw hydroxyapatite particles/poly L-lactide (F-u-HA/PLLA) *Biomaterials* **26** 5542-51

[117] Barber F A and Dockery W D 2008 Long-term absorption of beta-tricalcium phosphate poly-L-lactic acid interference screws *Arthroscopy-the Journal of Arthroscopic and Related Surgery* **24** 441-7

[118] Wei G B and Ma P X 2004 Structure and properties of nano-hydroxyapatite/polymer composite scaffolds for bone tissue engineering *Biomaterials* **25** 4749-57

[119] Liu H and Webster T J 2010 Ceramic/polymer nanocomposites with tunable drug delivery capability at specific disease sites *Journal of Biomedical Materials Research Part A* **93** 1180-92

[120] Kobayashi M, Rharbi Y, Brauge L, Cao L and Winnik M A 2002 Effect of silica as fillers on polymer interdiffusion in poly(butyl methacrylate) latex films *Macromolecules* **35** 7387-99

[121] Zhang Y J, Zhang G Z and Wei M 2009 Controlling the Biodegradation Rate of Magnesium Using Biomimetic Apatite Coating *J Biomed Mater Res B* **89B** 408-14

[122] Kokubo T and Takadama H 2006 How useful is SBF in predicting in vivo bone bioactivity? *Biomaterials* **27** 2907-15

[123] Guan R-G, Johnson I, Cui T, Zhao T, Zhao Z-Y, Li X and Liu H 2012 Electrodeposition of hydroxyapatite coating on Mg-4.0Zn-1.0Ca-0.6Zr alloy and in vitro evaluation of degradation, hemolysis, and cytotoxicity *Journal of Biomedical Materials Research Part A* **100A** 999-1015

[124] Bahrololoom M E, Javidi M, Javadpour S and Ma J 2009 Characterisation of natural hydroxyapatite extracted from bovine cortical bone ash *J Ceram Process Res* **10** 129-38

[125] Catledge S A, Fries M D, Vohra Y K, Lacefield W R, Lemons J E, Woodard S and Venugopalan R 2002 Nanostructured ceramics for biomedical implants *J Nanosci Nanotechnol* **2** 293-312

[126] Ergun C, Liu H, Webster T J, Olcay E, Yilmaz S and Sahin F C 2008 Increased osteoblast adhesion on nanoparticulate calcium phosphates with higher Ca/P ratios *J Biomed Mater Res A* **85** 236-41

[127] Liu H, Slamovich E B and Webster T J 2006 Increased osteoblast functions among nanophase titania/poly(lactide-co-glycolide) composites of the highest nanometer surface roughness *J Biomed Mater Res A* **78** 798-807

[128] Webster T J, Ergun C, Doremus R H and Bizios R 2002 Hydroxylapatite with substituted magnesium, zinc, cadmium, and yttrium. II. Mechanisms of osteoblast adhesion *J Biomed Mater Res* **59** 312-7

[129] Zhao S-f, Jiang Q-h, Peel S, Wang X-x and He F-m 2011 Effects of magnesium-substituted nanohydroxyapatite coating on implant osseointegration *Clinical Oral Implants Research* **22** 349-56

[130] Farahani T D, Entezami A A, Mobedi H and Abtahi M 2005 Degradation of poly(D,L-lactide-co-glycolide) 50 : 50 implant in aqueous medium *Iran Polym J* **14** 753-63

[131] Zhou W Y, Duan B, Wang M and Cheung W L 2009 Crystallization Kinetics of Poly(L-Lactide)/Carbonated Hydroxyapatite Nanocomposite Microspheres *J Appl Polym Sci* **113** 4100-15

[132] Mobedi H, Nekoomanesh M, Orafaei H and Mivehchi H 2006 Studying the degradation of poly (L-lactide) in presence of magnesium hydroxide *Iran Polym J* **15** 31

[133] Chen X, Yu J and Guo S 2006 Structure and properties of polypropylene composites filled with magnesium hydroxide *J Appl Polym Sci* **102** 4943-51

[134] Chen X, Yu J, Guo S, Luo Z and He M 2009 Effects of magnesium hydroxide and its surface modification on crystallization and rheological behaviors of polypropylene *Polym Composite* **30** 941-7

[135] Weir N A, Buchanan F J, Orr J F, Farrar D F and Boyd A 2004 Processing, annealing and sterilisation of poly-L-lactide *Biomaterials* **25** 3939-49

[136] Cifuentes S C, Benavente R and Gonzalez-Carrasco J L 2014 Does magnesium compromise the high temperature processability of novel biodegradable and bioresorbables PLLA/Mg composites? *Rev Metal Madrid* **50**

[137] Loo S C J, Ooi C P, Wee S H E and Boey Y C F 2005 Effect of isothermal annealing on the hydrolytic degradation rate of poly(lactide-co-glycolide) (PLGA) *Biomaterials* **26** 2827-33

[138] Tsuji H and Ikada Y 1995 Properties and Morphologies of Poly(L-Lactide) .1. Annealing Condition Effects on Properties and Morphologies of Poly(L-Lactide) *Polymer* **36** 2709-16

[139] Tabi T, Sajó I, Szabó F, Luyt A and Kovács J 2010 Crystalline structure of annealed polylactic acid and its relation to processing *Express Polym Lett* **4** 659-68

[140] Kim Y and Kim G 2013 Collagen/alginate scaffolds comprising core (PCL)-shell (collagen/alginate) struts for hard tissue regeneration: fabrication, characterisation, and cellular activities *J Mater Chem B* **1** 3185-94

[141] Sekosan G and Vasanthan N 2010 Morphological Changes of Annealed Poly-epsilon-caprolactone by Enzymatic Degradation with Lipase *J Polym Sci Pol Phys* **48** 202-11

[142] Jeong J C, Lee J and Cho K 2003 Effects of crystalline microstructure on drug release behavior of poly(epsilon-caprolactone) microspheres *J Control Release* **92** 249-58

[143] Cipriano A F, De Howitt N, Gott S C, Miller C, Rao M P and Liu H 2014 Bone marrow stromal cell adhesion and morphology on micro- and sub-micropatterned titanium *J Biomed Nanotechnol* **10** 660-8

[144] Aldana D S, Villa E D, Hernandez M D, Sanchez G G, Cruz Q R, Gallardo S F, Castillo H P and Casarrubias L B 2014 Barrier Properties of Polylactic Acid in Cellulose Based Packages Using Montmorillonite as Filler *Polymers-Basel* **6** 2386-403

[145] Park A and Cima L G 1996 In vitro cell response to differences in poly-L-lactide crystallinity *J Biomed Mater Res* **31** 17-30

[146] Groth T, Altankov G and Klosz K 1994 Adhesion of human peripheral blood lymphocytes is dependent on surface wettability and protein preadsorption *Biomaterials* **15** 423-8

[147] Wan Y, Yang J, Yang J, Bei J and Wang S 2003 Cell adhesion on gaseous plasma modified poly-(l-lactide) surface under shear stress field *Biomaterials* **24** 3757-64

[148] Johnson I, Akari K and Liu H N 2013 Nanostructured hydroxyapatite/poly(lactic-co-glycolic acid) composite coating for controlling magnesium degradation in simulated body fluid *Nanotechnology* **24**

[149] Lacombe R 2005 *Adhesion measurement methods: theory and practice*: CRC Press)

[150] 2015 PoLyInfo. Materials Information Station)

[151] Van Vooren C 2012 Water Permeability of PLGA and PHB Films Enriched with Additives. UGent)

[152] Le Duigou A, Davies P and Baley C 2009 Seawater ageing of flax/poly (lactic acid) biocomposites *Polym Degrad Stabil* **94** 1151-62

[153] Peng Y, Wu P and Yang Y 2003 Two-dimensional infrared correlation spectroscopy as a probe of sequential events in the diffusion process of water in poly(ε-caprolactone) *The Journal of Chemical Physics* **119** 8075-9

[154] Liu T-Y, Lin W-C, Yang M-C and Chen S-Y 2005 Miscibility, thermal characterization and crystallization of poly (l-lactide) and poly (tetramethylene adipate-co-terephthalate) blend membranes *Polymer* **46** 12586-94

[155] D'Souza S, Dorati R and DeLuca P P 2014 Effect of Hydration on Physicochemical Properties of End-Capped PLGA *Advances in Biomaterials* **2014**

[156] Ng C S, Teoh S H, Chung T S and Hutmacher D W 2000 Simultaneous biaxial drawing of poly (epsilon-caprolactone) films *Polymer* **41** 5855-64

[157] Auras R A, Lim L T, Selke S E M and Tsuji H 2011 *Poly(lactic acid): Synthesis, Structures, Properties, Processing, and Applications*: Wiley)

[158] Fraschini C, Plesu R, Sarasua J R and Prud'Homme R E 2005 Cracking in polylactide spherulites *J Polym Sci Pol Phys* **43** 3308-15

[159] Sorensen P A, Dam-Johansen K, Weinell C E and Kiil S 2010 Cathodic delamination of seawater-immersed anticorrosive coatings: Mapping of parameters affecting the rate *Prog Org Coat* **68** 283-92

[160] Okerberg B C, Berry B C, Garvey T R, Douglas J F, Karim A and Soles C L 2009 Competition between crystallization and dewetting fronts in thin polymer films *Soft Matter* **5** 562-7

[161] Xu D, Wang Z and Douglas J F 2007 Crystallization-induced fluid flow in polymer melts undergoing solidification *Macromolecules* **40** 1799-802

[162] Li P, Feng X L, Jia X L and Fan Y B 2010 Influences of tensile load on in vitro degradation of an electrospun poly(L-lactide-co-glycolide) scaffold *Acta Biomater* **6** 2991-6

[163] Piens M and De Deurwaerder H 2001 Effect of coating stress on adherence and on corrosion prevention *Prog Org Coat* **43** 18-24

[164] Croll S 1979 The origin of residual internal stress in solvent-cast thermoplastic coatings *J Appl Polym Sci* **23** 847-58

[165] Perera D Y and Nguyen T 1996 Hygroscopic stress and failure of coating/metal systems *Double Liaison* **43** 66-71

[166] Schneller T 2010 *Chemical solution deposition of functional oxide thin films* (Wien ; New York: Springer)

[167] Weldon D G 2009 *Failure analysis of paints and coatings* (Chichester, U.K.: Wiley)

[168] Hsu S T and Yao Y L 2014 Effect of Film Formation Method and Annealing on Morphology and Crystal Structure of Poly (L-Lactic Acid) Films *J Manuf Sci E-T Asme* **136**

[169] Hamley I W, Parras P, Castelletto V, Castillo R V, Muller A J, Pollet E, Dubois P and Martin C M 2006 Melt structure and its transformation by sequential crystallization of the two blocks within poly(L-lactide)-block-poly(epsilon-caprolactone) double crystalline diblock copolymers *Macromol Chem Physic* **207** 941-53

[170] Abdal-hay A, Barakat N A and Lim J K 2013 Influence of electrospinning and dip-coating techniques on the degradation and cytocompatibility of Mg-based alloy *Colloids and Surfaces A: Physicochemical and Engineering Aspects* **420** 37-45

[171] Hu R-G, Zhang S, Bu J-F, Lin C-J and Song G-L 2012 Recent progress in corrosion protection of magnesium alloys by organic coatings *Prog Org Coat* **73** 129-41

[172] Landi E, Logroscino G, Proietti L, Tampieri A, Sandri M and Sprio S 2008 Biomimetic Mg-substituted hydroxyapatite: from synthesis to in vivo behaviour *J Mater Sci-Mater M* **19** 239-47

[173] Zhao S F, Jiang Q H, Peel S, Wang X X and He F M 2013 Effects of magnesium-substituted nanohydroxyapatite coating on implant osseointegration *Clinical Oral Implants Research* **24** 34-41

[174] Leem Y H, Lee K S, Kim J H, Seok H K, Chang J S and Lee D H 2014 Magnesium ions facilitate integrin alpha 2- and alpha 3-mediated proliferation and enhance alkaline phosphatase expression and activity in hBMSCs *J Tissue Eng Regen Med*

[175] Cipriano A F, Sallee A, Guan R G, Zhao Z Y, Tayoba M, Sanchez J and Liu H 2015 Investigation of magnesium-zinc-calcium alloys and bone marrow derived mesenchymal stem cell response in direct culture *Acta Biomater* **12** 298-321